Strongly correlated superconductivity: A plaquette dynamical mean-field theory study

Kristjan Haule and Gabriel Kotliar

Department of Physics, Rutgers University, Piscataway, New Jersey 08854, USA

(Received 31 May 2007; published 13 September 2007)

We use cluster dynamical mean-field theory to study the simplest models of correlated electrons, the Hubbard model and the *t-J* model. We use a plaquette embedded in a medium as a reference frame to compute and interpret the physical properties of these models. We study various observables such as electronic lifetimes, one electron spectra, optical conductivities, superconducting stiffness, and the spin response in both the normal and the superconducting state in terms of correlation functions of the embedded cluster. We find that the shortest electron lifetime occurs near optimal doping where the superconducting critical temperature is maximal. A second critical doping connected to the change of topology of the Fermi surface is also identified. The mean-field theory provides a simple physical picture of three doping regimes, the underdoped, the overdoped, and the optimally doped regime, in terms of the physics of the quantum plaquette impurity model. We compare the plaquette dynamical mean-field theory results with earlier resonating valence bond mean-field theories, noting the improved description of the momentum space anisotropy of the normal state properties and the doping dependence of the coefficient of the linear temperature dependence of the superfluid density in the superconducting state.

PACS number(s): 71.27.+a, 71.30.+h

I. INTRODUCTION

The origin and the nature of superconductivity in strongly correlated materials is one of the greatest challenges in modern condensed matter theory. It received renewed attention with the discovery of the high temperature superconductivity in copper oxide based materials. While these materials have been studied intensively over the past decades, there is still no consensus as to what are the essential physical ingredients responsible for the high temperature superconductivity phenomena and how it should be modeled.[1–14]

Anderson proposed that the high temperature superconductivity phenomena was intimately connected with the proximity to a parent Mott-insulating state.[15,16] Developing precise connections between the proximity to a Mott insulator and high temperature superconductivity has proven to be a difficult problem. Suggestive conclusions have been reached using slave boson methods,[17,18] variational wave functions,[19,20] and gauge theory techniques.[2] However, lack of theoretical tools has made difficult to prove that simple models are sufficient to explain the phenomena surrounding cuprates. For example, it is still strongly debated whether the existence of superconductivity with a high critical temperature and a pseudogap is a genuine property of the models studied, or an artifact of the approximations employed to solve the model.

Over the past decade, significant progress in the field of correlated electrons has been achieved through the development of dynamical mean-field theory.[21,22] In its single site version, this method describes lattice models in terms of a single site impurity problem embedded in a medium. The method has been very successful in describing and even predicting numerous properties of a large number of materials.[23–31] Cluster extensions of this method, cluster dynamical mean-field theory (CDMFT) (for reviews, see Refs. 23 and 32), have been proposed and are currently a subject of intensive investigations.

In this paper, we apply the cluster dynamical mean-field approach to construct a mean-field theory of the simplest models of strongly correlated materials, the one band Hubbard and *t-J* models, using a 2×2 cluster, namely, the plaquette as the basic mean-field reference frame.

There are several motivations for constructing a mean-field theory based on a plaquette embedded in a dynamical bath of conduction electrons: (a) A plaquette embedded in a self-consistent medium can describe the physics of singlet formation, which is very important in the *t-J* and Hubbard models. There are two roads of singlet formation, the Kondo effect, in which a spin can form a singlet with a bath of conduction electrons, and the superexchange mechanism, which locks two spins on a bond in a singlet state. (b) A plaquette in a medium is a minimal unit to describe *d*-wave superconductivity and antiferromagnetism on the same footing, given that their order parameters (as well as that of other forms of order competing with superconductivity) naturally fit on a plaquette.

From a methodological perspective, mean-field theory allows one to study the physical properties of different phases as a function of control parameters, whether they are stable or metastable. For example, we will study the evolution of the superconducting state, together with the underlying normal state, which appears as a metastable phase below T_C. From a theoretical perspective, metastable states are only defined within a mean-field theory, but they are of clear physical relevance. Furthermore, comparison response or correlation functions in both the normal and the superconducting state give important clues as to the mechanism of superconductivity.

A clear understanding of the evolution of well defined mean-field phases of the simplified model is an important step toward constructing the phase diagram of realistic Hamiltonians. Even if a phase is not realized as the thermodynamically stable phase in a mean-field treatment of a simplified Hamiltonian, it could be stabilized by adding additional longer range terms in the Hamiltonian without sig-

nificantly altering the short distance properties described by the mean-field theory. Furthermore, a good understanding of the different mean-field states can be useful in elucidating the results of numerical studies in larger finite clusters, since complicated patterns in a finite size system may be a reflection of phase separation among different competing mean-field phases.

The study of minimal models such as the *t-J* model or the Hubbard model describing a system near a Mott transition is an important first step toward understanding real materials. From a study of minimal models, one can learn what aspects follow from just the proximity to a doping driven Mott transition. This is a necessary step before the importance of other physical effects, such as the disorder or the electron-phonon interactions certainly present in the real materials, can be ascertained. A basic question yet to be elucidated is to which extent a minimal model of the doping driven Mott transition, such as the *t-J* model, describes at the qualitative level the physical properties of the cuprates. If, indeed, the qualitatively low energy physics of the cuprates results from the proximity to a Mott-insulating state, as described by a minimal model of this phenomena, then the results can be refined by including more realistic band structure, for example, nearest- and next-nearest-neighbor hoppings, longer range interactions, disorder, and coupling to the lattice, as well as by incorporating a multiband situation which is needed to describe the physics in a wider energy range. It is possible to carry out these studies in the more realistic framework of the combination of electronic structure methods with dynamical mean-field theory (DMFT), a subject which is left for future studies. One should also ascertain the size of the corrections to the mean-field theory by either expanding around mean-field theory[33] or increasing the cluster size.[34]

Several studies have already shown that the Hubbard model treated within cluster DMFT on a 2×2 plaquette successfully describes many properties of the high temperature superconductors. For example, the competition of antiferromagnetism and superconductivity,[35–39] the existence of a pseudogap at low doping,[40–46] and the formation of Fermi arcs.[43,44,47,48]

These phenomena involve short-range nonlocal correlations. In CDMFT, the approach to the Mott insulator is characterized by the growth of the nonlocal components of the self-energy, which is responsible for the phenomena of momentum space differentiation and the formation of lines of zeros in the Green's function at zero temperature. Surprising manifestations of strong correlations include the transfer of optical spectral weight upon condensation,[49] the existence of an avoided quantum critical point[50] underlying the superconducting dome, and the presence of two distinct gaps[51,52] in the superconducting state of the underdoped cuprates. The approach describes well an anomalous incoherent normal state[45,49] which is lifted by the onset of superconductivity.[50,53]

Other studies of the Hubbard model using large clusters at values of $U \leq 8t$ have focused on the convergence of the critical temperature.[34] In a series of publications, it has been shown that the *d*-wave superconducting state is well described by spin fluctuation theory.[34,54,55] To which extent the physics of well defined quasiparticles interacting with spin fluctuations responsible for the pairing can be carried over to strong coupling regime is an important open problem, which can be only be addressed by gaining a better understanding of the large *U* limit of the Hubbard model, which is the focus of this paper.

Hence, we focus on understanding the physical content of the plaquette mean-field theory in the regime where the interaction strength is large enough to drive a Mott transition at half filling with a substantial Mott-Hubbard gap. We gain insights by comparing the superconducting state with the underlying normal state. For example, we study the evolution of the Fermi arcs with temperature and trace the mechanism of superconductivity to the optimization of the superexchange energy. We connect the maximum critical temperature with anomalies at optimal doping, resulting from a maximum in the inelastic scattering rate. The techniques introduced in this paper provide a simple interpretation of the cuprate phase diagram in terms of the occupations of a small number of cluster eigenstates or pseudoparticles which describe a mean-field coarse-grained version of the important excitations of the lattice system, and we use them to describe different experimental probes, tunneling optics, and neutron scattering, in both the normal and the *d*-wave superconducting phase. The superconducting state is characterized by two energy scales: one increases with decreasing doping, and one decreases with decreasing doping. The first can be identified with the photoemission gap in the antinodal region, while the second can be identified with the slope of the Dirac cone along the Fermi surface. We investigate the effect of the latter scale on the penetration depth.

The organization of the paper is the following: In Sec. II, we summarize the formalism and introduce the models, the cluster schemes, and the impurity solvers, i.e., the continuous time quantum Monte Carlo[56,57] (CTQMC) and a generalization of the non crossing approximation (NCA).[58–61] Section III describes the evolution of the cluster Green's functions and the self-energies as a function of doping. We identify the existence of an anomalous scattering rate describing the nodal region of the lattice model, which peaks at a characteristic doping δ_2^c in the normal phase. The scattering rate is drastically reduced in the superconducting state. We identify a second characteristic doping δ_1^c at which another self-energy diverges, and connect this phenomena to the formation of lines of zeros in the Green's function.

One can view CDMFT in the superconducting phase as a generalization of the Migdal-Eliashberg theory to strongly correlated electron systems, and we present the frequency dependence of the superconducting order parameter in Sec. IV. An advantage of the mean-field theory is that it allows us to study the "normal" state underlying the superconducting state and its evolution with temperature. This is done for the tunneling density of states in Sec. IV, for the optical conductivity in Sec. V, and for the magnetic properties in Sec. VI. This comparison between the mean-field normal state and the mean-field superconducting state establishes the superexchange as the main pairing mechanism, as surmised in the resonating valence bond (RVB) theory.

The pseudoparticles representing plaquette eigenstates are not only technical tools to set up strong coupling impurity solvers but provide a physical picture of the excitations of

the system, and we use them to interpret the CDMFT results in Sec. VII. We conclude with the connection between our method and an earlier simpler mean-field theory, approach based on the plaquette, the slave boson mean-field theory, and closely related methods. For related work advancing the RVB concepts using single site DMFT on multiorbital models, see Refs. 62 and 63.

II. FORMALISM

In this section, we summarize the methodology used for our investigation. Two minimal models of the proximity to a Mott transition were considered: the Hubbard model and the t-J model. There are several different versions of dynamical mean-field theory. For example, in addition to standard DMFT, an extended version of DMFT[23,59,60,64–68] (EDMFT) which replaces all the nonlocal terms in the interaction (namely, the kinetic energy and the superexchange) by a fermionic and a bosonic bath has been proposed. There are also numerous variants of cluster dynamical mean-field theory which differ by the dynamical medium surrounding the plaquette (hybridization function of the impurity model). Finally, the solution of the impurity model that results from the CDMFT mapping can be carried out with different impurity solvers. In this work, we use two complementary solvers, the NCA and the CTQMC method.

The goal of this paper, is to highlight physical properties which follow generally from the proximity to a Mott-insulating state, which are captured by a local approach, namely, cluster DMFT. For this reason, we have focused on physics which emerges from both Hubbard and t-J models, and which is captured by all the different cluster schemes (cellular DMFT,[69] dynamical cluster approximation,[70] and their extended versions). While we mention some quantitative differences between these schemes, the stress is on qualitative main conclusions that can be obtained with all quantum cluster schemes. In order to keep the presentation clear and the paper relatively concise, we provide only methodological details which are not available in the literature. To avoid unnecessary duplication, results for a given physical quantity are presented with only one cluster scheme and impurity solver, chosen to demonstrate more clearly a physical point.

A. Models

One of the more studied models in the field of strongly correlated electrons is the Hubbard model defined by the Hamiltonian

$$H = -\sum_{ij\sigma} t_{ij} c_{i\sigma}^{\dagger} c_{j\sigma} + \sum_i U n_{i\uparrow} n_{i\downarrow}. \quad (1)$$

It consists of a hopping term and an on-site repulsion. To be above the Mott-transition, we take an on-site repulsion $U = 12t$.

A second model of great interest is the t-J Hamiltonian,

$$H = -\sum_{ij\sigma} t_{ij} c_{i\sigma}^{\dagger} c_{j\sigma} + \frac{1}{2}\sum_{ij} J_{ij} \mathbf{S}_i \mathbf{S}_j. \quad (2)$$

It contains two terms: the first describes the kinetic energy which delocalizes the holes introduced by doping, and the second represents spin-spin interaction. In this work, we take $J/t = 0.3$.

In the t-J model, a constraint forbidding all double occupancy must be enforced, and will be treated exactly in this work. In the spirit of understanding general features of the proximity to the Mott state, we include only the nearest-neighbor hopping $t=1$ ($t'=0$).

B. Extended and standard dynamical mean-field theory

In DMFT, the nonlocal terms in the Hamiltonian coupling are replaced by a coupling to a bath of conduction electrons. In the Hubbard model, the only nonlocal term is the kinetic energy, and this leads to the standard DMFT mapping which is described in many reviews.[21] In the t-J model, also the superexchange interaction connects different sites, and applying the DMFT philosophy to that term also leads to the extended DMFT equations.

Here, we outline the derivation of the extended version of the cluster DMFT.[59,60,64,65] We first employ Hubbard-Stratonovich transformation to decouple the nonlocal interaction term of the t-J model, leading to the following action:

$$S = \int_0^{\beta} d\tau \left[\sum_{\mathbf{k}\sigma} c_{\mathbf{k}\sigma}^{\dagger}(\tau) \left(\frac{\partial}{\partial\tau} - \mu + \epsilon_{\mathbf{k}} \right) c_{\mathbf{k}\sigma}(\tau) + \sum_i U n_{i\uparrow}(\tau) n_{i\downarrow}(\tau) \right.$$
$$\left. + \sum_{\mathbf{q}} \left\{ \mathbf{\Phi}_{\mathbf{q}}^{\dagger}(\tau) \frac{2}{J_{\mathbf{q}}} \mathbf{\Phi}_{\mathbf{q}}(\tau) + i\mathbf{S}_{\mathbf{q}} [\mathbf{\Phi}_{\mathbf{q}}^{\dagger}(\tau) + \mathbf{\Phi}_{-\mathbf{q}}(\tau)] \right\} \right]. \quad (3)$$

Here, $\mathbf{\Phi}$ is the Hubbard-Stratonovich vector bosonic field which decouples the spin-spin interaction.

The many-body theory described by the action above can be summarized in a functional:

$$\Gamma[\mathcal{G},\mathcal{D}] = -\operatorname{Tr}\log(G_0^{-1} - \Sigma) - \operatorname{Tr}[\mathcal{G}\Sigma] + \frac{1}{2}\operatorname{Tr}\log(\mathcal{D}_0^{-1} - \Pi)$$
$$+ \frac{1}{2}\operatorname{Tr}[\mathcal{D}\Pi] + \Phi[\mathcal{G},\mathcal{D}]. \quad (4)$$

Here, functional Φ of the exact Baym-Kadanoff functional contains all two particle irreducible diagrams of an electron-boson system with propagators $\mathcal{G}$ and $\mathcal{D}$. Maximizing the functional Eq. (4) leads to the exact Dyson equations for this system. Cluster approximations are obtained by restricting the functional to a subset of trial Green's functions. In the cellular DMFT (C-DMFT),[23,69] the Φ functional is approximated as follows: The full lattice is covered by nonoverlapping clusters. The functional within each cluster is treated exactly, i.e., if two lattice points i and j are inside the same cluster, $\Phi^{C\text{-}DMFT}[\mathcal{G}_{ij},\mathcal{D}_{ij}] = \Phi^{exact}[\mathcal{G}_{ij},\mathcal{D}_{ij}]$. If, however, i and j are in different clusters, Φ functional is set to zero. In this way, short-range correlations within the cluster are treated exactly, while long-range correlations are ignored.

Cluster approximations are obtained by replacing the exact functional Φ in Eq. (4) by its cluster counterpart.

The saddle point equations then become $\Sigma_{cluster} = \delta\Phi(G_{cluster})/\delta G_{cluster}$ and $\Pi_{cluster} = -2\,\delta\Phi(D_{cluster})/\delta\Pi_{cluster}$.

The fluctuating bosons $\boldsymbol{\Phi}_\mathbf{q}$ in the extended DMFT formalism allow one to keep some out-of-cluster short-range correlations and describe better the spin fluctuations by allowing the cluster spin to relax more efficiently through its direct exchange interaction with the bath. We will see that this leads to higher superconducting critical temperatures. Apart from this quantitative difference, we did not find any qualitative difference between the extended version (which employs bosons to describe spin fluctuations between the clusters) and the results of the nonextended version of DMFT.

C. Cluster schemes and impurity models

There are several cluster schemes in use in the study of correlated electron materials. The dynamical cluster approximation[70] (DCA) can be thought of as a coarse graining in momentum space, obtained by relaxing the conservation of momentum. Rather than treating the infinite number of lattice $\mathbf{k}$ points and corresponding Green's functions $\mathcal{G}_\mathbf{k}$, the Φ functional is approximated to depend only on the Green's function of a few cluster momenta, which we will denote by $\mathbf{K}$ and $\mathbf{Q}$. The cluster Green's functions of the approximate functional $\Phi[\mathcal{G}_\mathbf{K}, \mathcal{D}_\mathbf{Q}]$ are obtained by course graining the exact Green's functions, i.e., $\mathcal{G}_\mathbf{k} \rightarrow \mathcal{G}_\mathbf{K} = \Sigma_{\mathbf{k} \in \mathbf{K}} \mathcal{G}_\mathbf{k}$ and $\mathcal{D}_\mathbf{q} \rightarrow \mathcal{D}_\mathbf{Q} = \Sigma_{\mathbf{q} \in \mathbf{Q}} \mathcal{D}_\mathbf{Q}$, where the sum $\Sigma_{\mathbf{k} \in \mathbf{K}}$ is over those $\mathbf{k}$ momenta in the Brillouin zone which correspond to certain cluster momenta $\mathbf{K}$ (see Refs. 32 and 70).

The results of this paper were obtained with both DCA and C-DMFT. Again, all the qualitative features to be discussed in the next sections can be seen with both methods. Since DCA is a cluster method with a simple interpretation in momentum space while C-DMFT has a simple interpretation in real space, the fact that the qualitative physics emerges from both approaches suggests that the physical properties that we discuss in this paper are genuine properties of cluster dynamical mean-field theory on a plaquette, irrespective of the specific cluster scheme used.

We summarize the abbreviations used in the remainder of the text:

(1) CDMFT: cluster DMFT,

(2) C-DMFT: cellular DMFT,[69]

(3) DCA: dynamical cluster approximation,[70]

(4) EC-DMFT: extended version of cellular DMFT,

(5) EDCA: extended version of dynamical cluster approximation.[70,71]

A great advantage of all cluster DMFT formulations is that the complicated functional Dyson equations for the self-energies and cluster response functions can be written in terms of an impurity model

$$Z = \int D[\psi^\dagger \psi] \exp\left[-S_{cluster}\right.$$

$$-\int_0^\beta d\tau \int_0^\beta d\tau' \sum_\mathbf{K} \underline{\psi}_\mathbf{K}^\dagger(\tau) \underline{\Delta}_\mathbf{K}(\tau,\tau') \underline{\psi}_\mathbf{K}(\tau')$$

$$\left.+\frac{1}{2}\int_0^\beta d\tau \int_0^\beta d\tau' \sum_\mathbf{Q} \mathbf{S}_\mathbf{Q}(\tau) \chi_{0\,\mathbf{Q}}^{-1}(\tau,\tau') \mathbf{S}_\mathbf{Q}(\tau')\right], \quad (5)$$

which is numerically tractable and where the effective Weiss fields $\boldsymbol{\Delta}$ and χ_0^{-1} have to obey the following self-consistency conditions:

$$\mathbf{G} = \sum_\mathbf{k} [i\omega - H_\mathbf{k} - \Sigma(i\omega)]^{-1} = [i\omega - E_{imp} - \Sigma(i\omega) - \boldsymbol{\Delta}(i\omega)]^{-1},$$

$$(6)$$

$$\chi = \sum_\mathbf{k} [\mathbf{M}(i\omega) + J_\mathbf{q}]^{-1} = [\mathbf{M}(i\omega) + \chi_0^{-1}(i\omega)]^{-1}, \quad (7)$$

which merely express the fact that the cluster quantities, computed from the impurity model $1/[i\omega - E_{imp} - \Sigma(i\omega) - \boldsymbol{\Delta}(i\omega)]$, have to coincide with the lattice local quantities when summing over the reduced Brillouin zone. Namely, in the C-DMFT, the lattice was divided into nonoverlapping clusters; hence, the summations over $\mathbf{k}$ run over the reduced Brillouin zone. Here, $\mathbf{M}$ plays the role of the spin self-energy which is computed from the local susceptibility and Weiss field by $\mathbf{M} = \chi^{-1} - \chi_0^{-1}$, as evident from Eq. (7).

A special feature of the 2×2 plaquette is worth stressing: the cluster momentum $\mathbf{K}$ is a good quantum number and therefore local quantities like Green's function $\mathbf{G}$ or hybridization $\boldsymbol{\Delta}$ take a diagonal form

$$\mathbf{G} = \begin{pmatrix} \underline{G}_{0,0} & 0 & 0 & 0 \\ 0 & \underline{G}_{\pi,0} & 0 & \\ 0 & 0 & \underline{G}_{0,\pi} & 0 \\ 0 & 0 & 0 & \underline{G}_{\pi,\pi} \end{pmatrix}. \quad (8)$$

For large clusters, cellular DMFT would lead to off-diagonal terms in the impurity action written on the basis of cluster momenta. The hybridization function in Eq. (5) would take the form $\underline{\psi}_\mathbf{K}^\dagger \underline{\Delta}_{\mathbf{KK'}} \underline{\psi}_{\mathbf{K'}}$. However, in the 2×2 case, both in C-DMFT and DCA, the hybridization function is diagonal in cluster momentum.

The DMFT mapping of the lattice model onto a plaquette in a medium allows us to make a connection between this problem and the multiorbital Hubbard models which have been studied in connection with the orbitally selective Mott transition.[72–74] This is defined by a set of bands, each one characterized by a local density of a states, labeled by its cluster wave vector. Notice, however, that the interaction among the orbitals, i.e., the Hubbard U term written in terms of $\underline{\psi}_\mathbf{K}^\dagger$ and $\underline{\psi}_\mathbf{K}$ is more complicated than what has been treated in the literature and deserves further investigations. The local density of states corresponding to the different bands can be obtained by setting $U=0$ and evaluating the noninteracting Green's function G_0 corresponding to each cluster wave vector. This is plotted in Fig. 1.

The formalism is easily extended to the superconducting state by introducing Nambu notation,

$$\underline{\psi}_\mathbf{K} = \begin{pmatrix} c_{\mathbf{K}\uparrow} \\ c_{-\mathbf{K}\downarrow}^\dagger \end{pmatrix}. \quad (9)$$

Assuming singlet pairing, all the previous discussion carries through, with the cluster Green's functions and hybridization functions taking the 2×2 matrix form:
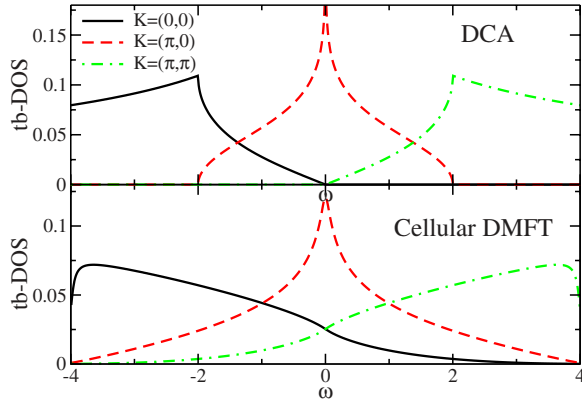
FIG. 1. (Color online) Tight-binding density of states (DOS) for the three orbitals within DCA and C-DMFT. Notice that the tight-binding Hamiltonian within C-DMFT Eq. (13) contains off-diagonal elements, therefore DOS does not contain full information about the noninteracting part of the Green's function G_0 ($G_0^{-1} = G^{-1} + \Sigma$).

$$G_{\underline{K}}(\tau) = -\langle T_\tau \underline{\psi}_K(\tau) \underline{\psi}_K^\dagger(0) \rangle = \begin{pmatrix} \mathcal{G}_{K\uparrow}(\tau) & \mathcal{F}_K(\tau) \\ \mathcal{F}_K^\dagger(\tau) & -\mathcal{G}_{-K\downarrow}(-\tau) \end{pmatrix}.$$
(10)

Here, $\mathcal{F}_K$ is the anomalous component of the Green's function. Hybridization $\underline{\Delta}_K$ becomes a matrix as well

$$\underline{\Delta}_K(i\omega) = \begin{pmatrix} \Delta_{K\uparrow}(i\omega) & \Delta_K^{an}(i\omega) \\ \Delta_K^{an\dagger}(i\omega) & -\Delta_{-K\downarrow}(-i\omega) \end{pmatrix}$$
(11)

and the impurity problem is off-diagonal in Nambu space.

In cluster momentum basis [see Eq. (8)], which we employed in this work on the 2×2 plaquette, DCA and C-DMFT share the same form of the impurity model; the only difference between the two schemes lies in the form of the self-consistency conditions. This is dictated by the form of the noninteracting part of the Hamiltonian H and the region of momentum summation. In the DCA scheme, the noninteracting Hamiltonian H_k is just the tight-binding energy $\epsilon_k = -2t(\cos k_x + \cos k_y) - 4t' \cos k_x \cos k_y$. In the self-consistency conditions Eqs. (6) and (7), the summation has to be performed only in the region of the patch corresponding to each cluster momentum K,[32] i.e.,

$$G_K = \sum_{k \in K} \left(\begin{pmatrix} i\omega + \mu - \epsilon_k & 0 \\ 0 & i\omega - \mu + \epsilon_k \end{pmatrix} - \underline{\Sigma}_K(i\omega) \right)^{-1}.$$
(12)

The patches which correspond to different cluster momentum K are, thus, completely decoupled in the self-consistency condition. Their coupling is only through the Coulomb interaction.

In the real space C-DMFT, we can still define "orbitals" which correspond to cluster momenta K [see the form of local quantities in Eq. (8)], however, these orbitals are coupled through both the Coulomb repulsion U and the noninteracting Hamiltonian, which takes the following form:

$$H_k = \begin{pmatrix} \epsilon_k^0 - \mu & 0 & iv_k^1 & 0 & iv_k^2 & 0 & v_k^0 & 0 \\ 0 & -\epsilon_k^0 + \mu & 0 & iv_k^1 & 0 & iv_k^2 & 0 & -v_k^0 \\ -iv_k^1 & 0 & \epsilon_k^1 - \mu & 0 & -v_k^0 & 0 & iv_k^4 & 0 \\ 0 & -iv_k^1 & 0 & -\epsilon_k^1 + \mu & 0 & v_k^0 & 0 & iv_k^4 \\ -iv_k^2 & 0 & -v_k^0 & 0 & \epsilon_k^2 - \mu & 0 & iv_k^3 & 0 \\ 0 & -iv_k^2 & 0 & v_k^0 & 0 & -\epsilon_k^2 + \mu & 0 & iv_k^3 \\ v_k^0 & 0 & -iv_k^4 & 0 & -iv_k^3 & 0 & \epsilon_k^3 - \mu & 0 \\ 0 & -v_k^0 & 0 & -iv_k^4 & 0 & -iv_k^3 & 0 & -\epsilon_k^3 + \mu \end{pmatrix},$$
(13)

where we defined

$$\epsilon_k^0 = -t(2 + \cos k_x + \cos k_y) - t'(1 + \cos k_x \cos k_y),$$

$$\epsilon_k^1 = t(\cos k_x - \cos k_y) + t'(1 + \cos k_x \cos k_y),$$

$$\epsilon_k^2 = -t(\cos k_x - \cos k_y) + t'(1 + \cos k_x \cos k_y),$$

$$\epsilon_k^3 = t(2 + \cos k_x + \cos k_y) - t'(1 + \cos k_x \cos k_y),$$

$$v_k^0 = t' \sin k_x \sin k_y,$$

$$v_k^1 = \sin k_x(t + t' \cos k_y),$$

$$v_k^2 = \sin k_y(t + t' \cos k_x),$$

$$v_k^3 = \sin k_x(t - t' \cos k_y),$$

$$v_k^4 = \sin k_y(t - t' \cos k_x).$$
(14)

The unit of distance chosen here is $a = 1/2$ such that the summation over the reduced Brillouin zone in Eqs. (6) and (7) simply runs over $k_x \in [-\pi, \pi]$ and $k_y \in [-\pi, \pi]$. One can
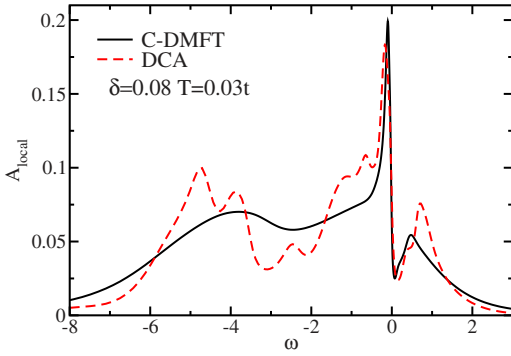
FIG. 2. (Color online) Comparison between the local spectral function computed in C-DMFT and in DCA with NCA used as impurity solver.

readily show that this summation leads to a diagonal form of local quantities.

In Fig. 2, we compare the local spectral function of the t-J model in the two cluster schemes. Notice the similarities of the results, in particular, at low energies. The spectral functions in both methods have a very similar pseudogap. Hence, in spite of quantitative differences, which will not be investigated systematically in this paper, the qualitative physics, which is the main focus of this paper, is present in both cluster methods. Note, however, that decoupling of orbitals in DCA method leads to splitting of the Hubbard band into peaks which correspond to excitations of the 2×2 cluster. These finite size effects are strongly reduced in C-DMFT method.

Here, we comment on some quantitative differences between the methods. The superconducting critical temperature is highest in EDCA method and reaches the value $\sim 0.036t$, while it drops to $\sim 0.026t$ in EC-DMFT. When the bosonic bath is switched off, the real space C-DMFT maximum critical temperature in both the t-J model at $J=0.3$ and the Hubbard model at $U=12t$ is around $\sim 0.01t$. Notice that this value is close to the estimations in Ref. 34 for the critical temperature of the Hubbard model in the thermodynamical limit for $U=4t$. Namely, the Hubbard model at $U=4t$ within large cluster DCA has $T_C \sim 0.023t$.[34] If we extrapolate this value to large $U=12t$ treating $T_C \propto J$,[75] T_C would drop to $\sim 0.008t$, which is close to the C-DMFT result.

The existence of a finite transition temperature and the trends of the superconducting transition temperature with doping and with the strength of the superexchange interaction are robust properties of plaquette DMFT and are common to all cluster schemes. It would be interesting to understand the convergence properties with cluster size within the different cluster schemes for the t-J model, as was done for the Hubbard model at intermediate U in Ref. 34 and in the classical limit in Ref. 76.

D. Impurity solvers

At the heart of the cluster DMFT is the solution of the impurity problem Eq. (5). In this work, we used two different impurity solvers, both based on the expansion of the impurity action with respect to hybridization strength. The first is the NCA, which sums up all diagrams with no crossing and is conveniently formulated in slave particle approach.[61] The second is the recently implemented CTQMC method,[56,57] which numerically samples the same type of diagrams but sums up all diagrams using Monte Carlo importance sampling. Here, we assume that the weights, which correspond to a set of all diagrams of definite perturbation order k, to be positive.

The two impurity solvers are in good agreement with each other on the imaginary axis, but the first method allows us to obtain real frequency correlation functions which are unavailable in the quantum Monte Carlo (QMC) approach. Both approaches are well suited to study the regime of intermediate temperatures and dopings, close to the tip of the superconducting dome, separating overdoped and underdoped regions, which is not easily accessible with other techniques.

Both impurity solvers used here require the introduction of the cluster eigenstates obtained by the exact diagonalization of the cluster, i.e., $H_{cluster}|m\rangle = E_m^{cluster}|m\rangle$. To each cluster eigenstate, a pseudoparticle a_m can be assigned, i.e.,

$$|m\rangle \equiv a_m^\dagger |0\rangle,$$ (15)

to recast the cluster part of the action to a quadratic form. The constraint

$$Q \equiv \sum_m a_m^\dagger a_m = \sum |m\rangle\langle m| = 1,$$ (16)

which expresses the completeness of the atomic eigenbase, has to be imposed.

The original problem can be exactly expressed in terms of pseudoparticles a_m, with the only nonquadratic term of the converted action being the hybridization between the and the medium,

$$S_{eff} = \int_0^\beta \sum_m a_m^\dagger(\tau)\left(\frac{\partial}{\partial \tau} + E_m^{cluster} - \lambda\right)a_m(\tau)$$

$$+ \int_0^\beta d\tau \int_0^\beta d\tau' \sum_{mnm'n'} a_m^\dagger(\tau)a_n(\tau)$$

$$\times D_{mnn'm'}(\tau - \tau')a_{n'}^\dagger(\tau')a_{m'}(\tau')$$ (17)

denoted here by

$$D_{m_1 m_2 m_3 m_4}(i\omega) = \sum_{\mathbf{K}} (\mathbf{F}^{\mathbf{K}\dagger})_{m_1 m_2} \Delta_{\mathbf{K}}(i\omega)(\mathbf{F}^{\mathbf{K}})_{m_3 m_4}$$

$$- \frac{1}{2}(\mathbf{S}_{\mathbf{K}})_{m_1 m_2} \chi_0^{-1}{}_{\mathbf{K}}(i\omega)(\mathbf{S}_{\mathbf{K}})_{m_3 m_4}, \quad (18)$$

where

$$(\mathbf{F}^{\mathbf{K}})_{mn} = \langle m|\underline{\psi}_{\mathbf{K}}|n\rangle = \begin{pmatrix} \langle m|c_{\mathbf{K}\uparrow}|n\rangle \\ \langle m|c_{-\mathbf{K}\downarrow}^\dagger|n\rangle \end{pmatrix}, \quad (19)$$

$$(\mathbf{S}_{\mathbf{Q}})_{mn} = \langle m|\mathbf{S}_{\mathbf{Q}}|n\rangle. \quad (20)$$

Note that the effective hybridization D combines both the fermionic ($\Delta_{\mathbf{K}}$) and bosonic baths ($\chi_0^{-1}{}_{\mathbf{K}}$) into the total effec-

tive Weiss field felt by the cluster eigenstates (pseudoparticles). We used Lagrange multiplier λ to enforce the constraint (16).

The continuous time quantum Monte Carlo method samples over the diagrams generated by expanding the action $\int D[a^\dagger a]\exp(-S_{cluster}-\Delta S)$ with respect to effective hybridization ΔS. Here, ΔS stands for the second term in Eq. (17). The probability to visit each diagram is proportional to its contribution to the partition function, which is computed by explicit evaluation of the cluster trace $\int D[a^\dagger a]e^{-S_{cluster}}(-\Delta S)^k/k!$, keeping only a single pseudoparticle in the system at each moment in imaginary time. In this way, the constraint $Q=1$ is explicitly taken into account. For more details, see Ref. 57.

In the diagrammatic method, the constraint $Q=1$ is imposed by letting the Lagrange multiplier λ approach infinity. The physical observable can then be computed using Abrikosov's trick[77] $\langle A \rangle_{Q=1} = \lim_{\lambda \to \infty} \frac{\langle QA \rangle}{\langle Q \rangle}$.

The coupling of the cluster to the medium, which simulates the rest of the lattice, causes the cluster eigenstates to decay in time. Therefore, their spectral functions carry nontrivial frequency dependence and important information about various physical processes such as the Ruderman-Kittel-Kasuya-Yosida (RKKY) interactions, the Kondo effect, and d-wave superconductivity. The corresponding pseudoparticle Green's function can be written in the form

$$\bar{G}_{mn}(\omega) = (\omega + \lambda - E_{cluster} - \bar{\Sigma})^{-1}_{mn}, \qquad (21)$$

where $(E_{cluster})_{mn} = (E_{cluster})_m \delta_{nm}$ is the energy of the cluster eigenstate and λ is the Lagrange multiplier which will be set to infinity at the end of the calculation.

Although hybridization is a small quantity compared to other scales in the problem, the perturbation is singular in the sense that at zero temperature an infinite number of diagrams substantially contribute to the solution of the problem. In Ref. 57 we showed a histogram (a distribution of the perturbation order) which is peaked around $\langle E_{kin} \rangle/T$, where E_{kin} is the average kinetic energy and T is the temperature. An infinite resummation of diagrams is, thus, necessary, and the noncrossing diagrams are simplest to compute.

Just like in the single site Anderson and Kondo impurity problem,[58,60] the noncrossing approximation works well down to some breakdown temperature, which is slightly below the superconducting transition temperature. Although NCA is not exact, this approximation has the virtue of directly yielding real frequency information. In Fig. 3, we present a typical comparison of the two impurity solvers on the imaginary axis for the cluster Green's functions of the t-J model in the normal state close to T_C. This comparison illustrates the degree of agreement within the two solvers on the imaginary axis. Notice that all the qualitative features of the evolution of the Green's functions with doping are seen in both methods. Therefore, we will use in this work the strategy of combining information from different solvers in order to draw conclusions as to the physical picture contained in the solution of the cluster DMFT equations of the t-J and Hubbard models, thus, avoiding the difficult problem of analytic continuation of imaginary time QMC data.
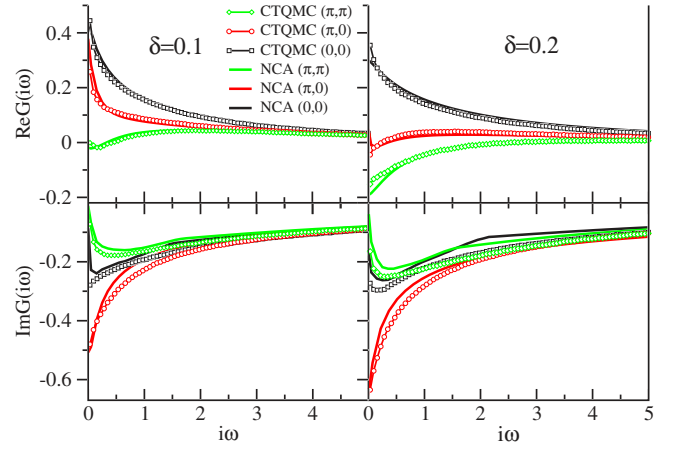

FIG. 3. (Color online) Comparison of NCA and CTQMC Green's functions on the imaginary axis for several doping levels. We used real space C-DMFT.

In the noncrossing approximation, the pseudoparticle self-energies are computed from

$$\bar{\Sigma}_{m'm}(i\omega) = T \sum_{i\epsilon,nn'} \bar{G}_{n'n}(i\epsilon)\{D_{nmm'n'}(i\epsilon - i\omega)$$
$$- D_{m'n'nm}(i\omega - i\epsilon)\}, \qquad (22)$$

while the physical quantities such as Green's function and susceptibility are obtained by the functional derivative of the NCA Luttinger functional with respect to the hybridization term and are given by

$$\mathcal{G}_\mathbf{K}(i\omega) = -T \sum_{i\epsilon,mnm'n'} (\mathbf{F}^\mathbf{K})_{m'n'}\bar{G}_{n'n}(i\epsilon)\bar{G}_{mm'}(i\epsilon - i\omega)(\mathbf{F}^{\mathbf{K}\dagger})_{nm},$$
$$\qquad (23)$$

$$\chi_\mathbf{Q}^{\alpha\beta}(i\omega) = T \sum_{i\epsilon,mnm'n'} (\mathbf{S}_\mathbf{Q}^\alpha)_{m'n'}\bar{G}_{n'n}(i\epsilon)\bar{G}_{mm'}(i\epsilon - i\omega)(\mathbf{S}_{-\mathbf{Q}}^\beta)_{nm}.$$
$$\qquad (24)$$

The above equations can be projected to the physical subspace $Q=1$ only on the real axis. In the limit $\lambda \to \infty$, they take the form

$$\bar{\Sigma}_{m'm}(\omega) = \sum_{\mathbf{K},nn'} \int d\xi f(\xi)\bar{G}_{n'n}(\xi + \omega)\{\hat{D}_{nmm'n'}(\xi)$$
$$+ \hat{D}_{m'n'nm}(-\xi)\}, \qquad (25)$$

$$\mathcal{G}_\mathbf{K}(\omega) = \sum_{mnm'n'} (\mathbf{F}^\mathbf{K})_{m'n'}(\mathbf{F}^{\mathbf{K}\dagger})_{nm}$$
$$\times \int d\xi e^{-\beta\xi}[\bar{G}_{n'n}(\xi + \omega)\hat{G}_{mm'}(\xi)$$
$$- \hat{G}_{n'n}(\xi)\bar{G}_{mm'}^*(\xi - \omega)], \qquad (26)$$

$$\chi_{\mathbf{Q}}^{\alpha\beta}(\omega) = \sum_{mnm'n'} (\mathbf{S}_{\mathbf{Q}}^{\alpha})_{m'n'}(\mathbf{S}_{\mathbf{Q}}^{\beta})_{nm}$$

$$\times \int d\xi e^{-\beta\xi}[\bar{G}_{n'n}(\xi+\omega)\hat{G}_{mm'}(\xi)$$

$$+ \hat{G}_{n'n}(\xi)\bar{G}_{mm'}^{*}(\xi-\omega)]. \tag{27}$$

Here, we used the following notation:

$$\hat{D}(\omega) = -\frac{1}{2\pi i}[D(\omega+i\delta) - D(\omega-i\delta)], \tag{28}$$

$$\hat{G} = -\frac{1}{2\pi i}[\bar{G}(\omega+i\delta) - \bar{G}(\omega-i\delta)]. \tag{29}$$

The pseudoparticle quantities (Green's functions $\hat{G}$ and self-energies $\hat{\Sigma}$) exponentially vanish below a certain threshold energy (they have x-ray singularity), which can be interpreted as the effective energy of the many-body state associated with the pseudoparticle. These thresholds can be removed by defining new quantities without threshold,[78] i.e.,

$$\tilde{G}(\epsilon) = \hat{G}(\epsilon)/f(-\epsilon), \tag{30}$$

$$\tilde{\Sigma}(\epsilon) = \hat{\Sigma}(\epsilon)/f(-\epsilon). \tag{31}$$

Using these quantities, we can rewrite the NCA equations as

$$\tilde{\Sigma}_{m'm}(\omega) = \sum_{\mathbf{K},nn'} \int d\xi \frac{f(\xi-\omega)f(-\xi)}{f(-\omega)} \tilde{G}_{n'n}(\xi)\{\hat{D}_{nmm'n'}(\xi-\omega)$$

$$+ \hat{D}_{m'n'nm}(\omega-\xi)\}, \tag{32}$$

$$\mathrm{Im}\, G_{\mathbf{K}}(\omega) = -\pi \sum_{mnm'n'} (\mathbf{F}^{\mathbf{K}})_{m'n'}(\mathbf{F}^{\mathbf{K}\dagger})_{nm} \int d\xi \frac{f(\xi-\omega)f(-\xi)}{f(-\omega)}$$

$$\times \tilde{G}_{n'n}(\xi)\tilde{G}_{mm'}(\xi-\omega), \tag{33}$$

$$\mathrm{Im}\,\chi_{\mathbf{Q}}^{\alpha\beta}(\omega) = -\pi \sum_{mnm'n'} (\mathbf{S}_{\mathbf{Q}}^{\alpha})_{m'n'}(\mathbf{S}_{\mathbf{Q}}^{\beta})_{nm} \int d\xi \frac{f(\xi-\omega)f(-\xi)}{b(-\omega)}$$

$$\times \tilde{G}_{n'n}(\xi)\tilde{G}_{mm'}(\xi-\omega). \tag{34}$$

At zero temperature, the combination of the Fermi functions $\frac{f(-\xi)f(\xi-\omega)}{f(-\omega)} = \frac{f(\xi)f(\omega-\xi)}{f(\omega)}$ is equal to unity in the interval $[\min(0,\omega), \max(0,\omega)]$ and zero outside.

These equations relate physical observables, such as $G_{\mathbf{K}}$ and $\chi_{\mathbf{Q}}$, to the pseudoparticle spectral functions. The latter represent coarse-grained versions of the important many-body excitations of the system including fermionic quasiparticles and bosonic collective modes. They have quantum numbers describing their spin, number of particles (which when divided by the cluster size gives the density), and coarse-grained momentum.

Relating several experimental observables such as photoemission spectra, tunneling spectra, and optical spectra to the same set of pseudoparticle spectral functions gives additional insights into the important excitations of the system.

III. CLUSTER ONE-PARTICLE GREEN'S FUNCTION, CLUSTER SELF-ENERGY, AND SCATTERING RATE

In this section, we discuss cluster quantities. As discussed in Sec. II, in both C-DMFT and DCA formalism, local quantities, such as cluster self-energies and cluster Green's function, are diagonal in the cluster momentum basis. Consequently, the physical behavior of the system within the cluster DMFT approach on a plaquette can be summarized in the four cluster quantities Σ_{00}, $\Sigma_{\pi 0}$, $\Sigma_{0\pi}$, and $\Sigma_{\pi\pi}$, corresponding to the eigenvalues of the matrix containing on-site, nearest-neighbor, and next-nearest-neighbor cluster self-energy introduced in Ref. 48. These cluster self-energies in the cluster momentum basis should not be interpreted as the lattice self-energies evaluated at four momentum points.

In the next few figures, we present low temperature self-energies for the *t*-*J* model on the imaginary axis obtained using the CTQMC impurity solver. Figure 4 contains the data in the normal state, and Fig. 5 the same quantities deep in the superconducting state.

Starting from the low temperature $T=0.01t$ normal state solution shown in Fig. 4, one notices large momentum differentiation at small doping. The three orbitals evolve very differently with changes in doping and temperature, as we will show in the following. The (0, 0) component has Fermi-liquid frequency dependence with relatively small scattering rate at zero frequency and small monotonic decrease of the real part of the self-energy with increasing doping. The two degenerate orbitals $(0, \pi)$ and $(\pi, 0)$ are distinctly different from the (0, 0) orbital. The scattering rate around optimal doping $0.12 \lesssim \delta \lesssim 0.22$ remains large (of order unity) even below the transition to superconducting state $T \sim 0.01t$. We notice in passing that it becomes increasingly difficult to converge the C-DMFT equations in the metastable normal state around optimal doping. Critical slowing down is observed, which might be a signature of local (cluster) instability, which might occur at zero temperature and might even preclude the continuation of a translationally invariant normal state solution down to zero temperature.

The $(\pi\pi)$ self-energy in Fig. 4 is by far the largest among all four and, except at very small and very large doping, it does not show any signature of coherence. At $\delta \sim 0.1$, it has a clear pole at zero frequency. From the above plot, we can see that a pole is on the real axis, and it is located above the Fermi level at small doping, crosses the Fermi level around $\delta \sim 0.1$, and finally, becomes negative in the optimal and overdoped regimes. A very sharp pole on the real axis described above is, indeed, confirmed by the NCA calculation. The consequence of the pole in self-energy is the appearance of zeros of the Green's function as discussed in Ref. 43. Physically, it means that some states in momentum space are damped and gapped even at very low temperature. Figure 5 at lower temperatures shows that this behavior persist to temperatures much lower than T_C. Hence, even in superconducting state, the large Luttinger Fermi surface is not recovered. The antinodal fermions are strongly damped and gapped even in the superconducting state. This is related to the occurrence of Fermi arcs and lines of zeros of the Green's function[79] as noticed in Refs. 43, 44, and 80. This phenomenon was first noticed in microscopic studies of coupled
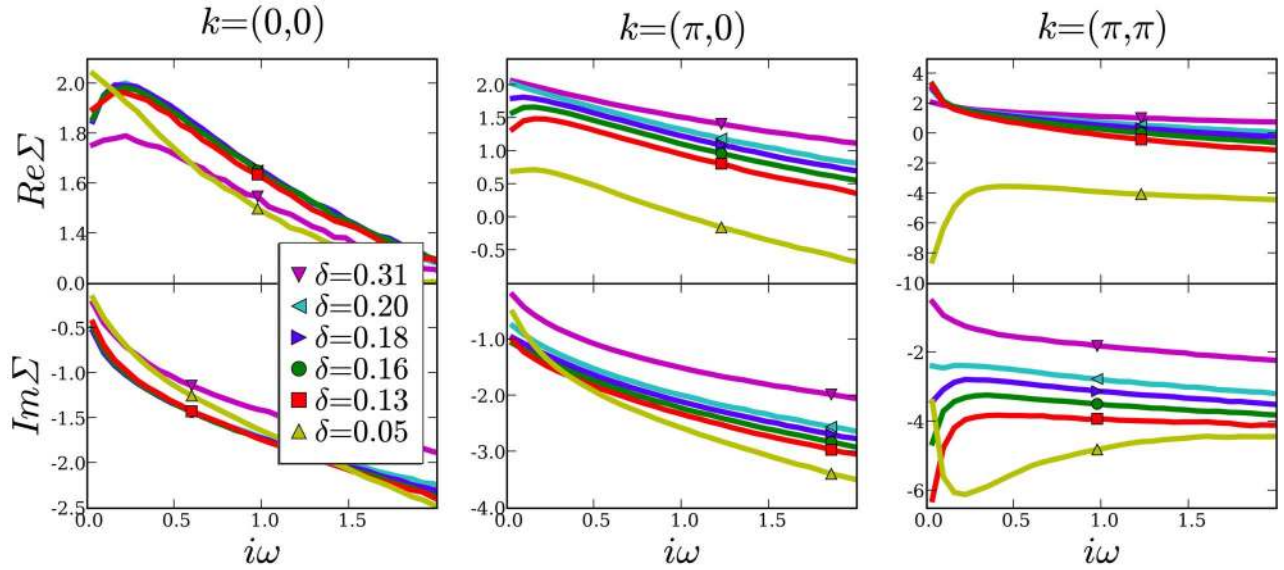
FIG. 4. (Color online) C-DMFT cluster self-energies of the t-J model using CTQMC as the impurity solver. Temperature $T=0.01t$ and system is in the normal state. Notice that Σ_{00} is Fermi-liquid-like (imaginary part vanishes at zero Matsubara frequency below the coherence temperature) in the whole range of doping, $\Sigma_{\pi 0}$ is Fermi liquid in the overdoped and underdoped regimes, while the scattering rate remains of the order of unity in the optimally doped regime. Finally, $\Sigma_{\pi\pi}$ is by far the largest self-energy. Its real part is so large that the orbital is gapped in all doping ranges considered. The scattering rate is enormous and a pole appears on the real axis around $\delta=0.1$. The pole is above E_F at very small doping, crosses E_F at $\delta=0.1$, and goes below E_F for optimally doped and overdoped regimes. This causes a sign change of the real part of $\Sigma_{\pi\pi}$. The $(\pi\pi)$ orbital is, thus, in the Mott-insulating state in most of the doping ranges considered.

ladders,[81,82] and related proposals also appeared in recent phenomenological models of high T_C's.[83–85] However, in these studies, the location of the lines of zeros is tied to the umklapp surface, while in the cluster DMFT, the lines of zeros is a dynamical object which evolves in a highly non-trivial way with doping.

The pole in $(\pi\pi)$ self-energy crosses the Fermi level at a critical doping (or at least becomes very large at low energies) that we denote by δ_1^c. The existence of a pole in the self-energy appears also in the Hubbard model with an important difference. In the Hubbard model, the pole is always below E_F and, therefore, this "critical" doping δ_1^c is zero. We also want to mention that at small $U=6$ (below the Mott transition of the undoped system) in the Hubbard model, the above mentioned pole seems to be absent or at least substantially reduced. This substantiates the idea that the lines of zeros in the Green function appear only above a critical coupling.

Figure 5 shows cluster self-energies at a lower temperature, i.e., $T=0.005t$ in the superconducting state. The $(0, 0)$ orbital does not change very dramatically except that it becomes more coherent. On the other hand, the $(\pi,0)$ orbital does show a dramatic effect. The huge scattering rate is now replaced by the large anomalous component of the self-energy, while the scattering rate is severely reduced. The peak in anomalous self-energy seems to track T_C and coincides with the point of maximal scattering rate in the normal state. We will call this doping δ_2^c since it corresponds to the avoided critical point identified in Ref. 50. Finally, the (π,π) component of the self-energy sharpens with reducing temperature, and the pole at $\delta_1^c \sim 0.1$ is even more apparent. This result is quite surprising because the superconducting state is

expected to be more coherent. As we show above, coherence is only restored in three of the four orbitals, while the $(\pi\pi)$ orbital remains gapped. Hence, the Fermi surface underlying the normal state does not contain the Luttinger volume at small doping.

In Figs. 6 and 7, we show the cluster Green's functions of the t-J model in the normal state and the superconducting state at lower temperatures. The cluster Green's functions describe a coarse-grained average of the lattice Green's function over some parts of the Brillouin zone. It is evident from Fig. 6 that the $(\pi,0)$ orbital contains most of the spectral weight (largest imaginary part of $G_{\pi 0}$) over the whole doping regime considered here. The (π, π) orbital is clearly gapped since the real part of the self-energy is too big to pick up any states inside the band as was previously observed in the extended DMFT study of the same model.[59,60] The important message is contained in the real part of $(\pi,0)$ cluster Green's function. The real part measures the particle-hole asymmetry of the orbital. It would vanish if the orbital is perfectly particle-hole symmetric. As one can see in Figs. 6 and 7, the $(\pi,0)$ orbital has "more weight" below E_F in the underdoped regime and more weight above E_F in the overdoped regime. Remarkably, it becomes almost particle-hole symmetric in the region of optimal doping. The exact point of particle-hole symmetry is close to ~ 0.18, which is just slightly above the point of maximal T_C and maximal anomalous self-energy. Figure 7 demonstrates that this remarkable symmetry persists even in the superconducting state, where the gap appears in all the orbitals.

We now compare the previous findings with the corresponding quantities in the Hubbard model displayed in Figs. 8, 9, 11, and 12. The Hubbard model at $U=12t$ has roughly
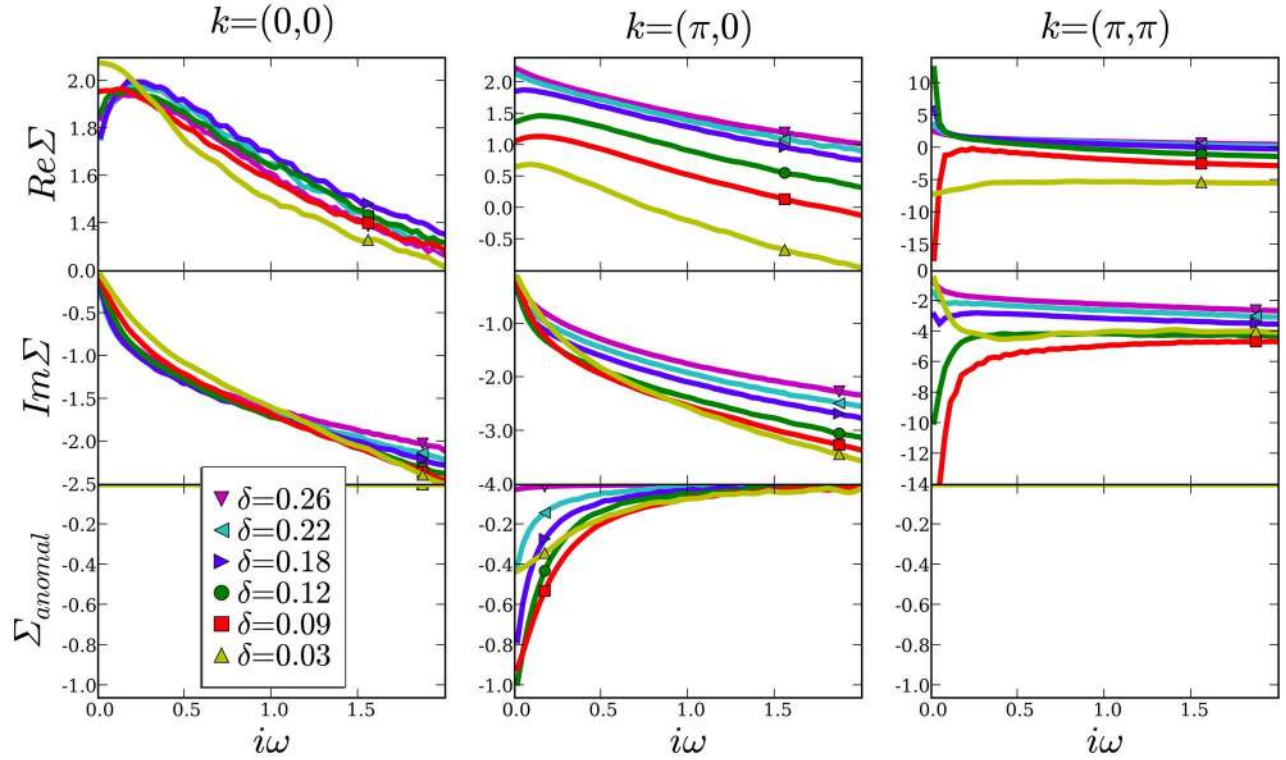
FIG. 5. (Color online) Same as in Fig. 4 but at lower temperature $T=0.005t$ in the superconducting state. The bottom row shows the anomalous self-energy. The (0,0) orbital barely changes in the superconducting state. On the other hand, the large scattering rate in $(\pi,0)$ orbital is severely reduced in the superconducting state and the orbital becomes Fermi-liquid-like. The large scattering rate in the normal state is now replaced by a large anomalous component of self-energy (peaked around $\delta \sim 0.15$, see Fig. 18). Finally, the pole in (π,π) self-energy sharpens and the orbital remains Mott-insulating in most of the doping ranges considered. A pole of the cluster self-energy is accompanied by a line of zeros of the Green's functions in certain parts of the momentum space (Refs. 43 and 44) and persists in the superconducting state.
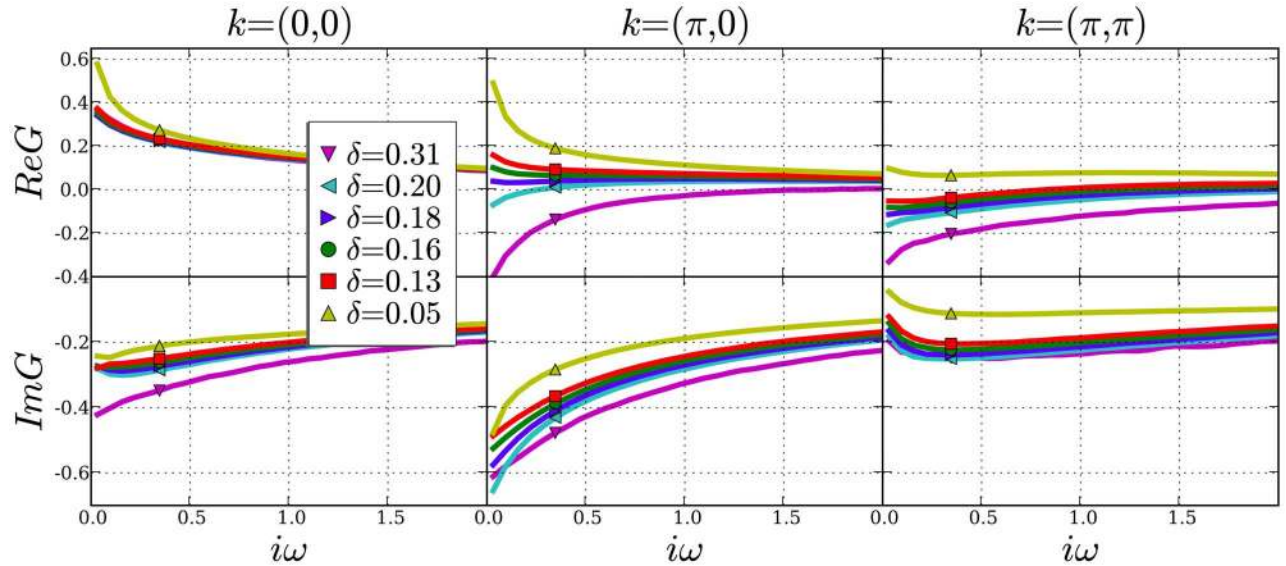
FIG. 6. (Color online) C-DMFT cluster Green's functions at $T=0.01t$ in the normal state of the t-J model obtained by CTQMC. The real part of the Green's function vanishes for particle-hole symmetric situation, while it is positive when the spectral weight below E_F has the "largest weight" and vice versa. The (0,0) orbital does not change much with doping and remains close to half-filling. The $(\pi,0)$ orbital gives most of the weight at the Fermi level (has largest imaginary part at zero frequency) and remarkably becomes particle-hole symmetric at the doping level slightly larger than the optimally doped level ($\delta=0.18$). The (π,π) orbital is gapped for all doping levels.
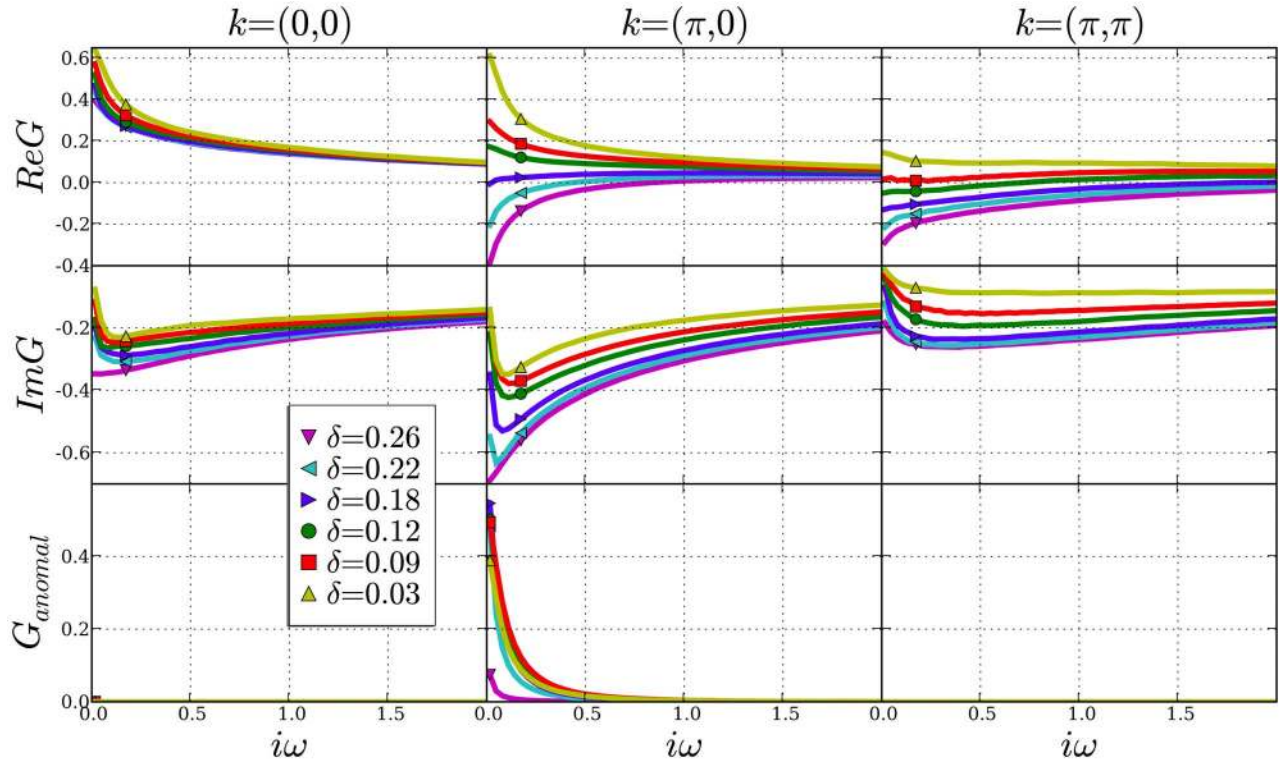
FIG. 7. (Color online) C-DMFT cluster Green's functions of the t-J model at $T=0.005t$ in the superconducting state obtained by CTQMC. Superconducting gap opens, in particular, in the $(\pi,0)$ orbital. Particle-hole symmetry of this orbital is again evident from the real part of the Green's function being close to zero around optimal doping (blue curve with triangles pointing right).

the same superexchange as the one used in the previous study of the t-J model, $J \sim 0.3t$, and therefore, we expect a similar physical behavior. We will demonstrate below that, indeed, this is the case, and we will highlight some quantitative differences between the two models, such as the numerical values of the critical dopings for cluster quantities δ_1^c and δ_2^c.

Figure 8 shows the four cluster Green's functions at $T=0.01t$ in the normal state. When the off-diagonal long-range order is allowed, the system starts to develop anomalous components in the optimally doped regime at this temperature, just like in the t-J model at the same temperature. In the metastable normal state, the $(0, 0)$ orbital is again the most coherent orbital and is not very sensitive to doping. On the other hand, the $(\pi,0)$ orbital is clearly coherent for small and large doping and the scattering rate around $\delta \sim 0.1$ is of the order unity. The point of maximum scattering rate and maximum anomalous self-energy in the Hubbard model is, however, slightly shifted toward lower doping (relative to the t-J model), i.e., $\delta_2^c \sim 0.1$.

The (π,π) orbital is again the one with the largest self-energy and scattering rate. In the Hubbard model, the pole on the real axis crosses zero exactly at zero doping; hence, $\delta_1^c=0$. However, even at optimal doping ~ 0.1, the real part of the self-energy is so large that the orbital is almost completely gapped.

Figure 9 demonstrates that the pole in $\Sigma_{\pi\pi}$ does not disappear in the superconducting state. This was also the case in the t-J model, and it is, therefore, a robust feature of the

approach to the Mott insulator within CDMFT. The physical interpretation is that part of the underlying Fermi surface remains gapped even in the superconducting state. The $(\pi,0)$ orbital becomes coherent when entering the superconducting state. Its imaginary part, at low frequencies, is maximal around δ_2^c.

The cluster self-energies in the cluster site representation contain useful information about the range. For example, it has been argued that near the Mott insulator, they become long ranged, while the cluster cumulant remains short ranged.[43,44] In Fig. 10, we show the on-site, nearest-neighbor, and next-nearest-neighbor self-energy, the actual output of the C-DMFT scheme. These are related to the eigenvalues shown above through the following linear relations:

$$\Sigma_{R=(0,0)} = \frac{1}{4}(\Sigma_{00} + \Sigma_{\pi 0} + \Sigma_{0\pi} + \Sigma_{\pi\pi}), \qquad (35)$$

$$\Sigma_{R=(1,0)} = \frac{1}{4}(\Sigma_{00} - \Sigma_{\pi 0} + \Sigma_{0\pi} - \Sigma_{\pi\pi}), \qquad (36)$$

$$\Sigma_{R=(0,1)} = \frac{1}{4}(\Sigma_{00} + \Sigma_{\pi 0} - \Sigma_{0\pi} - \Sigma_{\pi\pi}), \qquad (37)$$

$$\Sigma_{R=(1,1)} = \frac{1}{4}(\Sigma_{00} - \Sigma_{\pi 0} - \Sigma_{0\pi} + \Sigma_{\pi\pi}). \qquad (38)$$
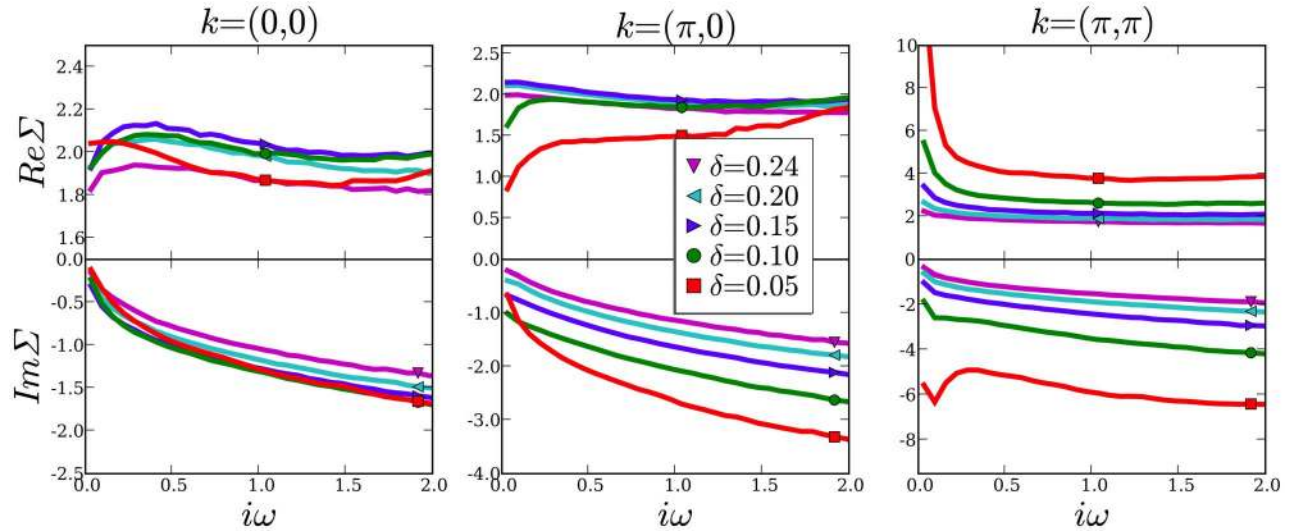
FIG. 8. (Color online) Hubbard model cluster self-energies in C-DMFT obtained by CTQMC at $T=0.01t$ and $U=12t$ in the normal state. Just like in the t-J model, the $(0,0)$ orbital is Fermi-liquid-like in the whole doping regime, while the $(\pi,0)$ orbital is coherent only in the underdoped and overdoped regimes. At optimal doping (in the Hubbard model, optimal doping is around $\delta \sim 0.1$), the scattering rate is largest. The important difference appears in the (π,π) orbital. The (π,π) self-energy is the largest self-energy of the system just like in the t-J model. Contrary to the t-J model, the pole in the (π,π) self-energy on the real axis, which appears in the t-J model around $\delta=0.1$, is now at zero doping. The self-energy of the (π,π) orbital, thus, monotonically grows when approaching the Mott insulator.

On the heavily overdoped side of the Hubbard model, $\delta > 0.16$, presented in Fig. 10, it is clear that the only relevant quantity is the on-site self-energy, which justifies the use of the single site DMFT in the overdoped site of the system. In the underdoped regime, however, the nearest-neighbor and next-nearest neighbor self-energies are large and give rise to
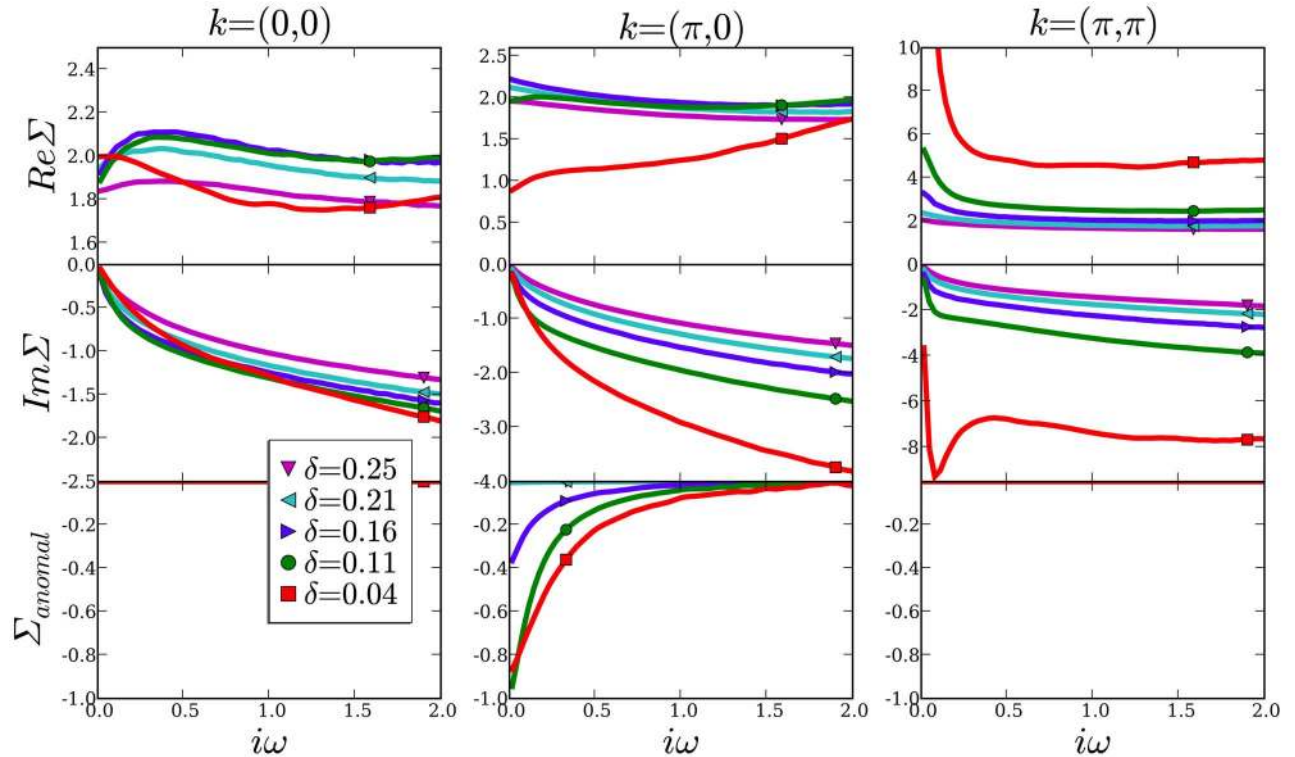

FIG. 9. (Color online) Similar to Fig. 8 but at lower temperature $T=0.005t$ in the superconducting state. Just like in the t-J model, the $(\pi,0)$ orbital, which is representative of the nodal part of the self-energy, becomes coherent in the superconducting state and the anomalous self-energy is largest around $\delta \sim 0.1$, where the scattering rate is largest in the normal state. The (π,π) self-energy sharpens with decreasing temperature just like in the Hubbard model, showing that this orbital is in the Mott-insulating state in the underdoped and optimally doped regimes.
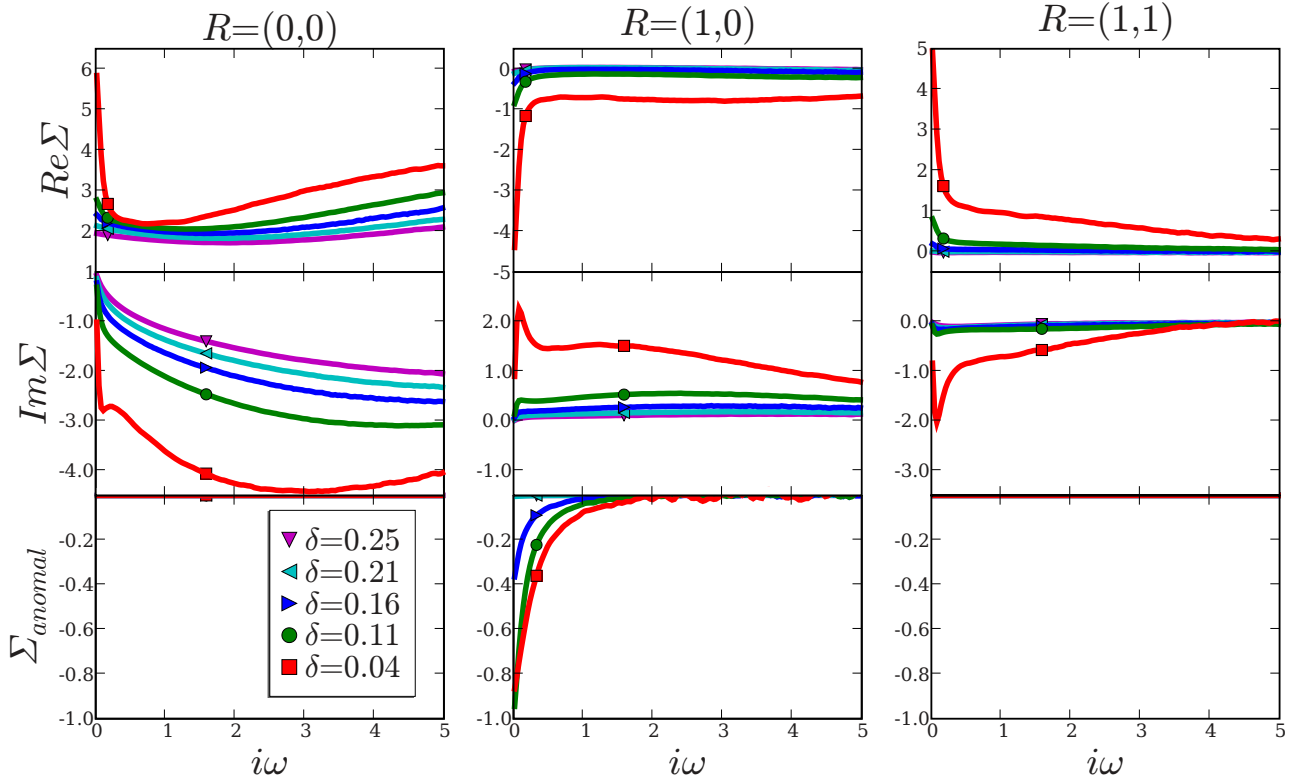
FIG. 10. (Color online) The on-site and short-range self-energies of the Hubbard model in the superconducting state at $T=0.005t$. The on-site self-energy is the largest, and its imaginary part vanishes for all finite dopings. The reason is that the pole in the (π,π) self-energy is now at zero doping. The nonlocal components of the self-energy vanish rather rapidly with doping.

qualitatively different results than those of a single site DMFT. They renormalize the nearest-neighbor and next-nearest-neighbor hoppings and induce a substantial next-nearest-neighbor hopping even for the model with vanishing bare t'. Furthermore, they distort the Fermi surface and cause variation of coherence across the Fermi surface as we will show below.

Finally, the cluster Green's functions for the Hubbard model are shown for two temperatures $T=0.01$ and $T=0.005$ in Figs. 11 and 12 at $U=12t$. Again, we notice qualitatively similar behavior than those found in the t-J model. The (π,π) orbital is gapped in both normal and superconducting states. The $(\pi,0)$ orbital contains most of the spec-
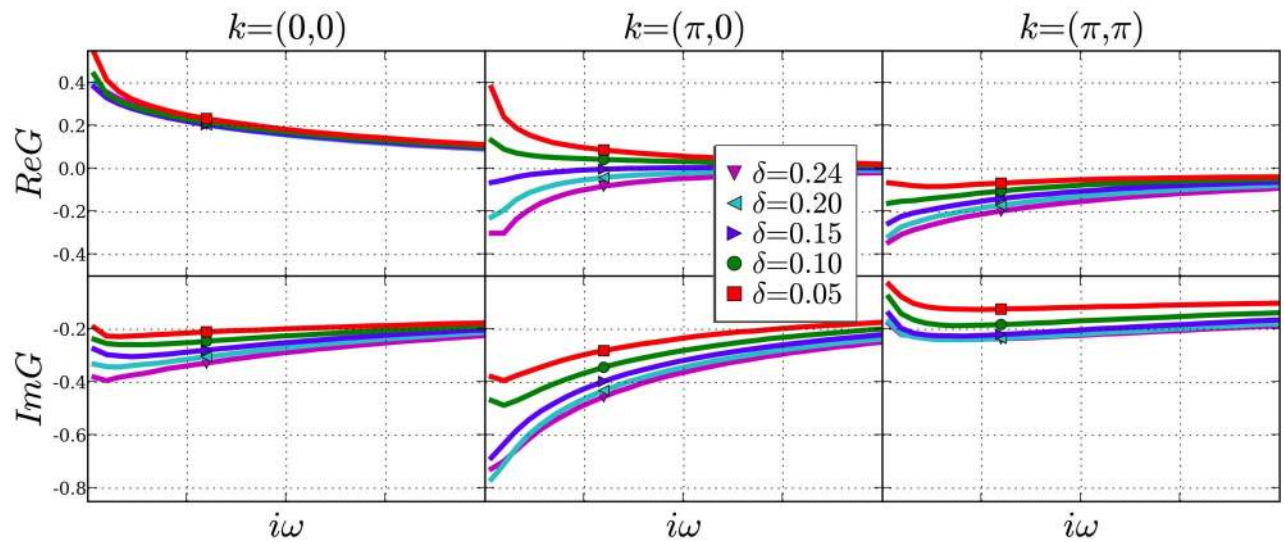

FIG. 11. (Color online) Hubbard model Green's function in the normal state at $T=0.01t$. The physics is the same as in Fig. 6 for the t-J model. The only difference is that the particle-hole symmetric point of the $(\pi,0)$ orbital appears around $\delta \sim 0.12$, which is again slightly above the optimally doped level.
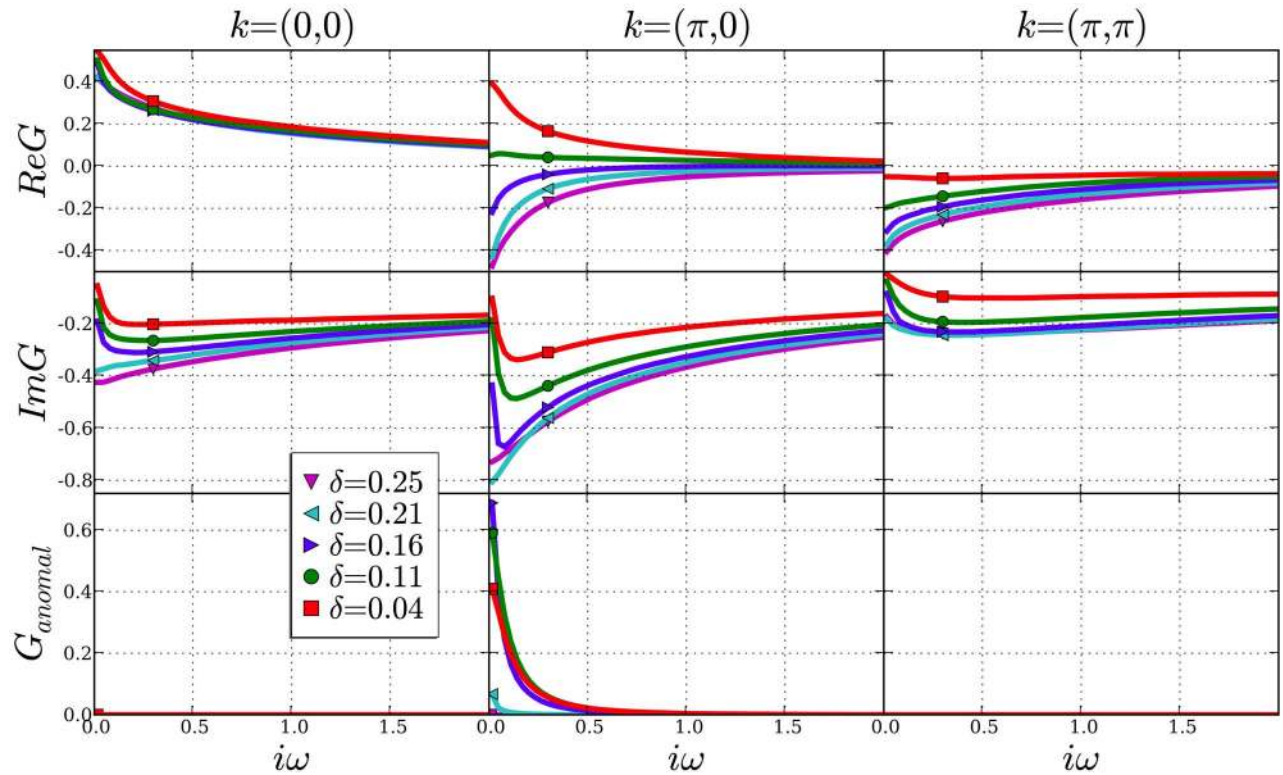
FIG. 12. (Color online) Similar to Fig. 11 but for lower temperature $T=0.005t$ in the superconducting state.

tral weight and becomes particle-hole symmetric slightly above optimal doping around, i.e., $\delta \approx 0.12$. This particle-hole symmetry persists in the superconducting state.

We now turn to the real frequency information. In most of what follows, we show results for the *t-J* model, except when explicitly stated otherwise.

Figure 13 shows the evolution of the CDMFT cluster spectral functions as a function of frequency for a few doping levels. Notice that due to symmetry, $(\pi,0)$ and $(0,\pi)$ spectral functions coincide. At zero doping (not shown), all four orbitals are half filled and the system is in Mott-insulating state.

Upon doping the system, the (π,π) orbital is emptied first, but in a very unusual way. Although its occupancy becomes much smaller than unity and, therefore, one would naively expect a large number of hole carriers in this band, it remains basically gapped for arbitrary doping as we have established above on the basis of the CTQMC results. This is very unusual since one naively expects the orbital to be gapped only at an integer filling. Only at very large doping, $\delta > 0.3$, the self-energy of this orbital approaches the other three self-energies so that the self-energy becomes momentum independent and, therefore, local. At this large doping, the (π,π) orbital is essentially empty and we can think of this orbital as an Anderson impurity model in the empty orbital regime.

The (0, 0) orbital is also very inert in the whole doping range. Its density of states at the Fermi level is small, while its occupancy only slightly decreases with increasing doping. The orbital remains close to half-filling with very small number of charge carriers induced in this band.

Finally, the $(0,\pi)$ [and $(\pi,0)$] components have sharp spectral features with very strong doping dependence. In going from $\delta=0.3$ to $\delta=0.1$, we observe the narrowing of the quasiparticle width reminiscent of the single site DMFT; however, a qualitative feature of CDMFT is that at smaller dopings this narrowing of the width is arrested, as a result of the presence of exchange effects as seen in slave boson studies[86] and in the large N limit of the *t-J* model.[87]

At low doping, the spectral function develops a pseudogap on the scale of *J*, with most of the coherent spectral weight below the Fermi level and a small fraction of it above the Fermi level. This is a general feature of the approach to the Mott transition in cluster DMFT, and has been seen in earlier studies.[41,42,45,59,60]

The important message contained in Fig. 13 is that the momentum differentiation at small doping is very large. The (π,π) orbital remains gapped at all dopings. It is in the Mott-insulating state at low doping and becomes empty in the overdoped regime; hence, it undergoes a band insulator to Mott insulator transition with decreasing doping. Most of the dynamical information of the active degrees of freedom representing the electrons close to the Fermi surface of the lattice model is, however, contained in the $(0,\pi)$ and $(\pi,0)$ components.

The frequency dependence of the cluster $(\pi,0)$ self-energy and its evolution with doping on the real axis is shown in Fig. 14. At small doping, the holelike scattering rate $(\omega<0)$ is large, while the electronlike rate $(\omega>0)$ is small. Around optimal doping, the self-energy is roughly linear in frequency, however, with large zero-frequency value. In this regime, there is still a large particle-hole asymmetry
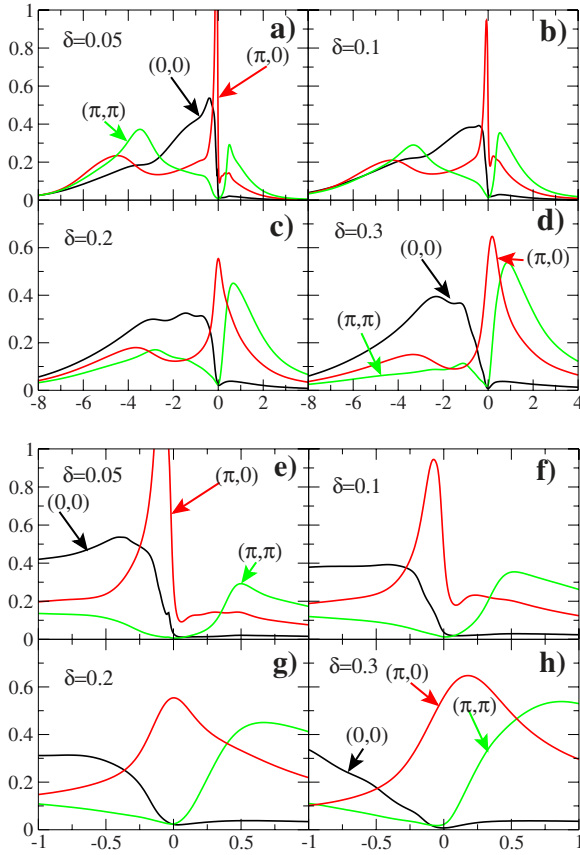
FIG. 13. (Color online) Evolution of the EC-DMFT cluster spectral functions of the *t*-*J* model with doping in the normal state at $T=0.025t \sim T_C$, using NCA as an impurity solver. The upper panel shows the spectra in the interval between $[-8t, 4t]$, where the Hubbard band is clearly observed. The lower panel shows the region near the Fermi level.

in the scattering rate. While the holelike part is linear with a relatively small slope down to $\omega=-0.5t$, the electron part is increasing only in the small region up to $\omega=0.15t$ with larger slope. Only in the strongly overdoped system does the self-energy become roughly particle-hole symmetric at low frequency. This particle-hole asymmetry in scattering rate can be contrasted with the approximate particle-hole symmetry

in the one-particle Green's function at optimal doping. The combination of the real part of the self-energy and the band structure leads to approximate recovery of this symmetry in the local one-particle spectra at optimal doping although it is absent in the scattering rate.

Zero-frequency quantities

Further insight into the nature of the CDMFT solution can be obtained by examining the cluster self-energies at zero frequency. In Fig. 15, we display the CTQMC self-energy for the *t*-*J* model at the lowest Matsubara frequency as a function of doping. In the overdoped side, the real parts of all four self-energies merge; therefore, the self-energy becomes local. The single site DMFT is adequate. The coherent quasiparticle peak at the Fermi level is formed and arises mainly from the $(\pi, 0)$ orbital. The reason is that the noninteracting density of states for $(0, 0)$, (π, π), and $(0, \pi)$ orbital extends roughly between $[-4t, 0]$, $[0, 4t]$, and $[-2t, 2t]$, respectively (see Fig. 1). For the momentum independent self-energy, the Friedel sum rule dictates that the effective chemical potential $\mu - \Sigma(0)$ is at the corresponding noninteracting chemical potential μ_0, which is slightly below zero frequency. The (π, π) orbital is, therefore, empty, being band insulator like. At smaller doping, this orbital acquires an enormous real part of $\Sigma'(0)$, which pushes the effective chemical potential $\mu - \Sigma'(0)$ far below the band edge of the tight-binding Hamiltonian. This orbital is, therefore, in the Mott-insulating state for smaller dopings. The insulating state in this orbital does change the nature from bandlike to Mott-like insulator.

For the $(0, 0)$ orbital, the effective chemical potential is close to its upper band edge. The noninteracting density of states at the band edge for this orbital is small (see Fig. 1), and only a very small number of charge carriers are doped into the orbital. Therefore, it remains close to a Mott-insulating state with small scattering rate at the Fermi level.

The $(\pi, 0)$ orbital is slightly less than half filled in the doping range considered here, and the real part of the self-energy smoothly increases with doping (see Fig. 15) such that the effective chemical potential $\mu - \Sigma'(0)$ is positive in the underdoped side (carriers are holelike) and negative in the overdoped side (carriers are electronlike). Close to optimal doping, effective chemical potential is close to zero,
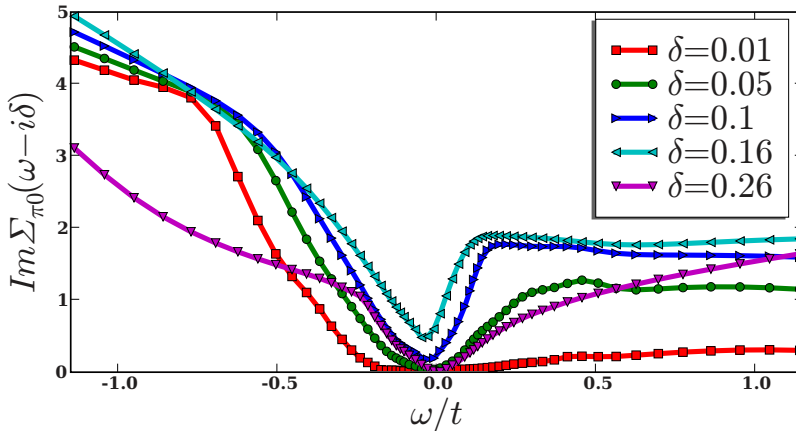

FIG. 14. (Color online) EC-DMFT cluster self-energies on the real axis in the normal state of the *t*-*J* model computed by NCA at $T=0.025t \sim T_C$.
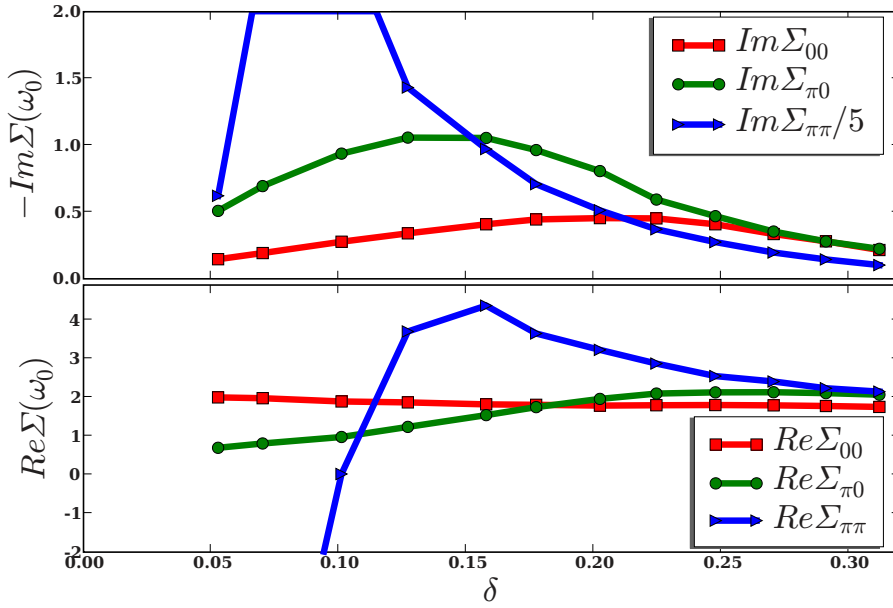
FIG. 15. (Color online) C-DMFT cluster self-energies at the lowest Matsubara point $\Sigma(i\omega_0) \sim \Sigma(\omega=0)$ versus doping in CTQMC at $T=0.01t$ in the normal state of the t-J model.

which makes the orbital approximately particle-hole symmetric at low frequency (see Fig. 13).

The (π,π) self-energy acquires a pole on the real axis around $\delta_1^c \sim 10\%$ doping, which can be identified in Fig. 15 as a divergent point of $\Sigma''_{\pi\pi}(0)$ and zero of $\Sigma'_{\pi\pi}(0)$.

Figure 16 describes the low energy phase shift in each orbital. It is defined by $\delta_K = \arg(G_K(i0+))$. Phase shifts are defined mod π. Notice two important features: at very small doping, the phase shifts in all channels are close to zero. They confirm the picture suggested in Ref. 50, in which the cluster degrees of freedom are weakly affected by the surroundings. It is reminiscent of the RKKY phase of the two impurity Kondo model. The system reaches the unitarity limit, as the phase shift crosses $\pi/2$ in the $(0,\pi)$ channel near $\delta=0.18$. This is because the real part of the cluster Green's function at zero frequency vanishes around optimal doping as shown in Figs. 6 and 7.

The indication for the existence of an anomaly around δ_2^c is seen most clearly in the imaginary part of the real frequency electron self-energy at $(0,\pi)$, evaluated at zero frequency. We display EDCA-NCA calculations of it in the upper panel of Fig. 17. At large and small doping, the scattering rate is small as expected for a Fermi liquid. Remarkably, it
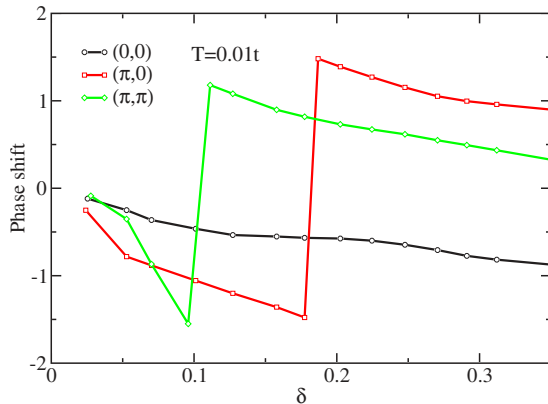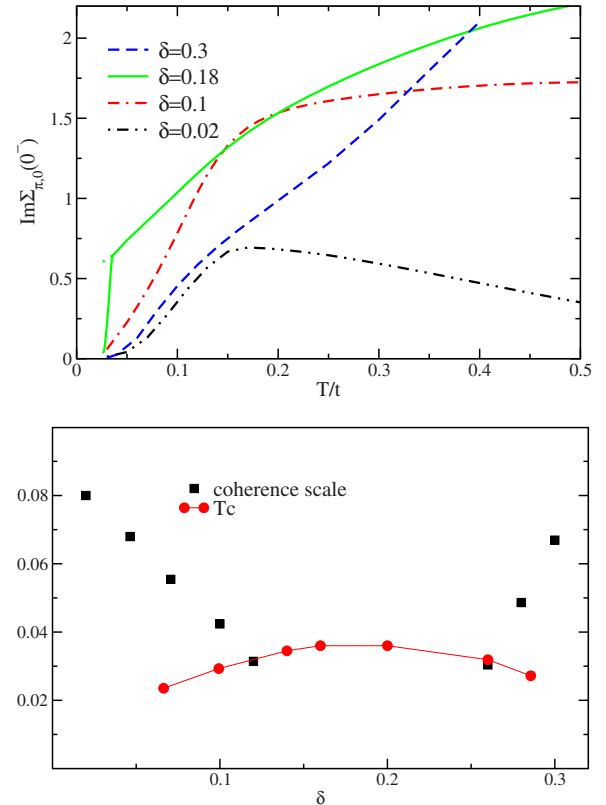

FIG. 16. (Color online) Phase shift (see definition in the text) versus doping for the four orbitals of the cluster obtained by CTQMC within C-DMFT method in the t-J model.

FIG. 17. (Color online) Upper panel: The imaginary part of the cluster $(\pi,0)$ self-energy at zero frequency as a function of temperature for a few doping levels, computed with EDCA using NCA as the impurity solver. Lower panel: An estimation of the coherent scale in the normal state of the t-J model (black dots) and transition temperature to superconducting state (red dots) within EDCA using NCA as the impurity solver.
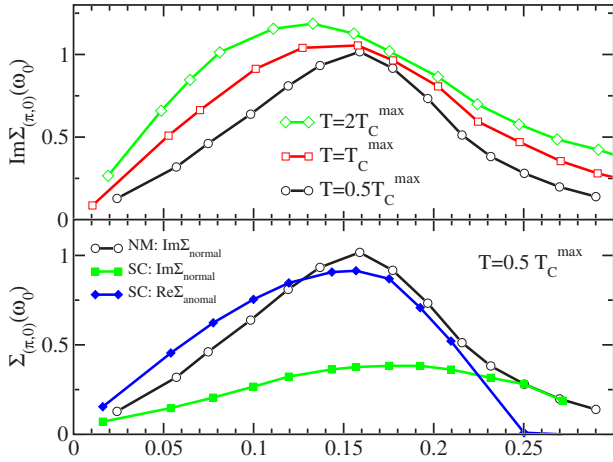
FIG. 18. (Color online) Upper panel: Imaginary part of $(\pi,0)$ cluster self-energy at the lowest Matsubara frequency $i\pi T$ versus doping for three different temperatures obtained by CTQMC for the t-J model. The scattering rate is peaked at optimal doping. Lower panel: The large imaginary part of self-energy of the normal state (black curve with circles) is severely reduced in the superconducting state (green curve with squares). The scattering rate is peaked at the point of maximal anomalous self-energy (blue curve with diamonds), tracking the point of the highest T_C.

becomes very large in the region near optimal doping when the critical temperature is maximal. This doping point corresponds to the above defined critical doping δ_2^c, which is in NCA around 0.18. The transition to the superconducting state, severely reduces the scattering rate, eliminating the

traces of the underlying critical behavior. A coherence scale, estimated from the scattering rate, is plotted in the bottom panel of Fig. 17 and is shown to have a tendency to vanish close to the point of maximal superconducting transition temperature.

Figure 18 shows the CTQMC results for the scattering rate within CDMFT and confirms the incoherence of the optimally doped system. The imaginary part of the self-energy at the first Matsubara point is small for both the underdoped and overdoped systems, while it is peaked at optimal doping. The peak is slightly shifted with temperature and, if the normal state is continued below the superconducting transition temperature, the peak of scattering rate coincides with the maximum of the anomalous self-energy, which traces the maximum of the transition temperature (see Fig. 19). The scattering rate is severely reduced in the superconducting state when off-diagonal long-range order is allowed in the calculation.

IV. SUPERCONDUCTIVITY, TUNNELING DENSITY OF STATES, FERMI ARCS, AND NODAL QUASIPARTICLES

The superconducting state is characterized by an order parameter $\langle c_{\mathbf{k}\uparrow} c_{-\mathbf{k}\downarrow} \rangle = \mathcal{F}_{\mathbf{k}}(\tau=0)$ and by the presence of a frequency dependent anomalous component to the self-energy. In Nambu notation, the self-energy in $(\pi,0)$ and $(0,\pi)$ orbitals takes the following form:
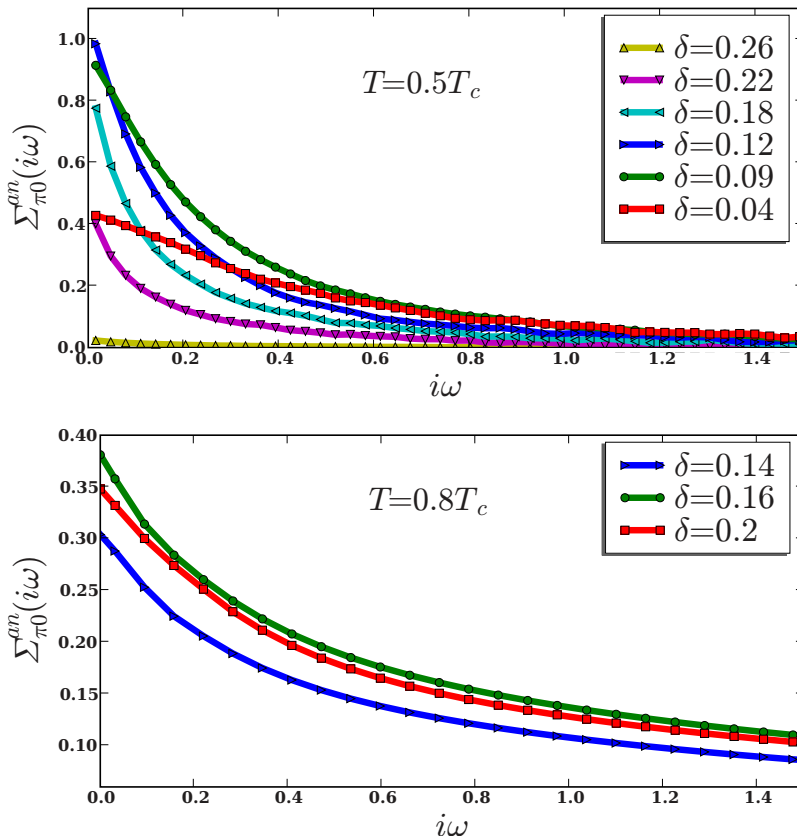

FIG. 19. (Color online) Upper panel: C-DMFT t-J model anomalous self-energy computed by CTQMC at $T=0.005t \sim 0.5 T_c^{max}$. Lower panel: t-J model anomalous self-energy within EDCA computed by NCA at $T=0.033t \sim 0.9 T_c^{max}$.
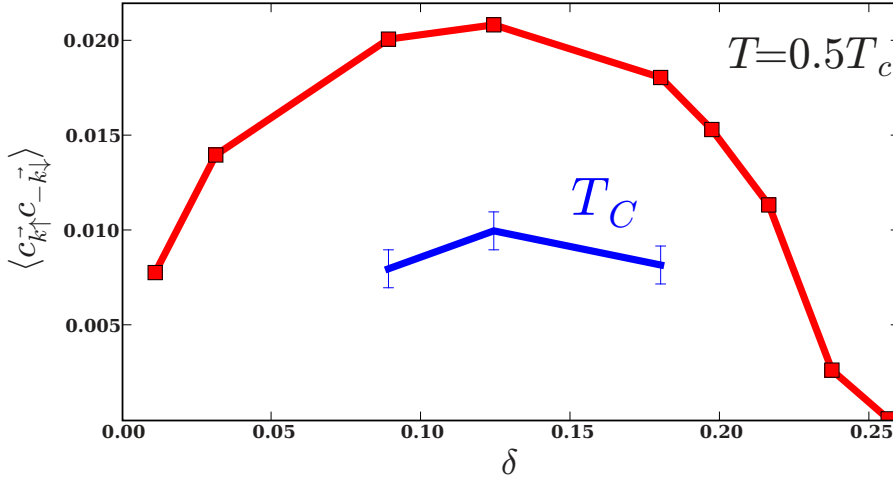
FIG. 20. (Color online) Order parameter in C-DMFT computed with CTQMC at $T=0.5T_{cmax}$. The critical temperature (in units of t) for a few doping values is also displayed.

$$\underline{\Sigma}_{\mathbf{K}}(i\omega) = \begin{pmatrix} \Sigma_{\mathbf{K}\uparrow}(i\omega) & \Sigma_{\mathbf{K}}^{an}(i\omega) \\ \Sigma_{\mathbf{K}}^{an}(i\omega) & -\Sigma_{-\mathbf{K}\downarrow}(-i\omega) \end{pmatrix} \quad (39)$$

and the corresponding Green's function is

$$\underline{G}_{\mathbf{K}}(i\omega) = \begin{pmatrix} \mathcal{G}_{\mathbf{K}\uparrow}(i\omega) & \mathcal{F}_{\mathbf{K}}(i\omega) \\ \mathcal{F}_{\mathbf{K}}^{\dagger}(i\omega) & -\mathcal{G}_{-\mathbf{K}\downarrow}(-i\omega) \end{pmatrix}. \quad (40)$$

The sign of the anomalous components chosen by the system is $\Sigma_{\pi 0}^{an}=-\Sigma_{0\pi}^{an}$. Within C-DMFT, this is precisely the nearest-neighbor self-energy and its lattice analog (using the original C-DMFT periodization[69]) takes the form $\Sigma_{\mathbf{k}}=\frac{1}{2}(\cos k_x -\cos k_y)\Sigma_{0\pi}^{an}$.

The anomalous self-energy $\Sigma_{\pi 0}^{an}$ is plotted in Fig. 19. The upper part of the figure shows the CTQMC results within C-DMFT, while the lower part shows the NCA results within EDCA. In both cases, the function is monotonically decreasing with imaginary frequency and is largest at optimal doping. Furthermore, at the low values of the Matsubara frequency, the anomalous self-energy exhibits a fast upturn and sublinear frequency behavior that becomes less pronounced as the doping is reduced. This trend is likely due to the reduction of density of states in the pseudogap region.

The anomalous self-energy obeys a spectral representation

$$\Sigma_{\mathbf{k}}^{an}(i\omega_n) = \Sigma_{\mathbf{k}}^{an}(\infty) - \int \frac{d\omega}{\pi} \frac{\text{Im} \Sigma_{\mathbf{k}}^{an}(\omega)}{i\omega_n - \omega}.$$

The infinite frequency value of the self-energy vanishes in the Hubbard model but is nonzero in the t-J model, and is related to the order parameter of the system $\mathcal{F}_{\mathbf{q}}(\tau=0)$ through the following exact relation:

$$\Sigma_{\mathbf{k}}^{an}(\infty) = -\frac{3}{(1+\delta)^2} \sum_{\mathbf{q}} J_{\mathbf{k}-\mathbf{q}} \mathcal{F}_{\mathbf{q}}(\tau=0), \quad (41)$$

where $\mathcal{F}_{\mathbf{q}}(\tau=0) = \langle c_{\mathbf{q}\uparrow} c_{-\mathbf{q}\downarrow} \rangle$.

Notice that simpler mean-field theories of the t-J model such as the slave boson mean-field theory[88] assume only the static, frequency independent anomalous self-energy. Other approaches based on the equation of motion for the Hubbard

operators[89] capture a frequency dependent order parameter but neglect the static infinite frequency component. A similar analysis of the pairing interaction has recently been carried out for the ladders in Ref. 90.

The existence of a finite value of the anomalous self-energy of the t-J model at infinite frequency should be interpreted as the existence of a nonzero value for anomalous self-energy in the Hubbard model at a scale of the order U.

The value of the anomalous self-energy at zero frequency and low temperature, and the gap (defined as the distance between the positive and negative energy peaks in the tunneling density of states divided by 2) are similar in all versions of the cluster DMFT. For the parameters used in our study ($J/t=0.3$, near optimal doping), the anomalous self-energy is of the order of unity at low temperature (see the upper panel of Fig. 19).

On the other hand, T_C, the superconducting order parameter, and the value of anomalous $\Sigma^{an}(\infty)$ are more sensitive quantities and differ between the various cluster schemes. The schemes with higher T_C (extended versions of CDMFT) show slower decrease of the anomalous self-energy, larger infinite frequency component of the anomalous self-energy, and larger value of the superconducting order parameter. In C-DMFT, the maximum value of the order parameter is around 0.02 (see Fig. 20), which is approximately eight times smaller than the maximum achieved in EDCA. Consequently, the static pairing in C-DMFT is very small, while it reaches almost $1/3$ in extended versions of the cluster DMFT (both in EDCA and in EC-DMFT), i.e., the magnitude of the anomalous self-energy at infinity as compared to the value at zero shown in Fig. 19.

From the anomalous Green's function, we can extract the order parameter, i.e., the anomalous Green's function at equal time $\mathcal{F}_{\pi 0}(\tau=0)$. The order parameter versus doping as obtained by the CTQMC and C-DMFT is shown in Fig. 20. It has a domelike shape and tracks the value of the critical temperature, just like in BCS theory. In the same figure, we also display critical temperature T_C at optimal doping. Due to a critical slowing down in the region of transition, many DMFT iterations are needed to determine the critical temperature.

The temperature dependence of the related quantity, the anomalous self-energy at infinity, computed with NCA is
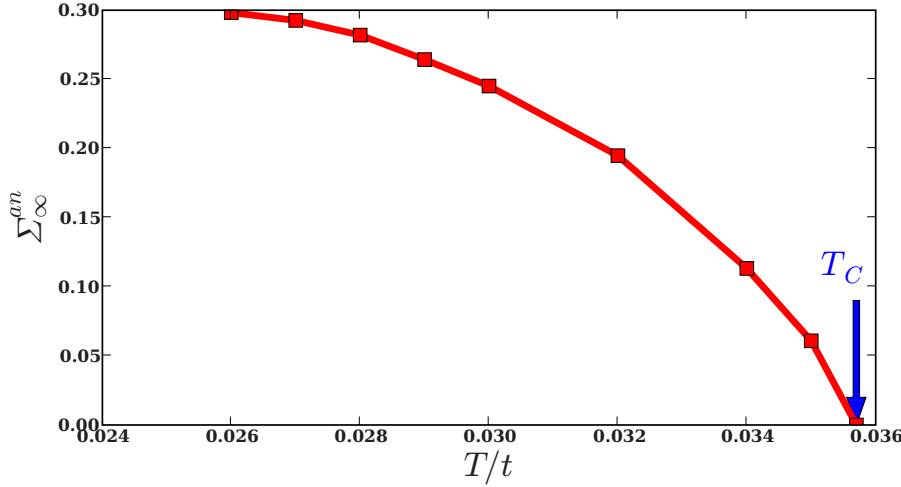
FIG. 21. (Color online) Anomalous self-energy $\Sigma^{an}(\omega=\infty)$ as a function of temperature within EDCA using NCA as the impurity solver at optimal doping $\delta=0.18$.

shown in Fig. 21. It has a clear BCS-like temperature dependence, saturating to a value of the order of ~ 0.3, which is around $1/3$ of the zero-frequency value.

Using NCA, we can examine directly $\Sigma''(\omega)$ and $\Sigma'(\omega)$ on the real axis. There are several features in the frequency dependence of the anomalous self-energies depicted in Fig. 22 which exhibit noticeable departures from the standard Migdal-Eliashberg theory of superconductivity. First, the real
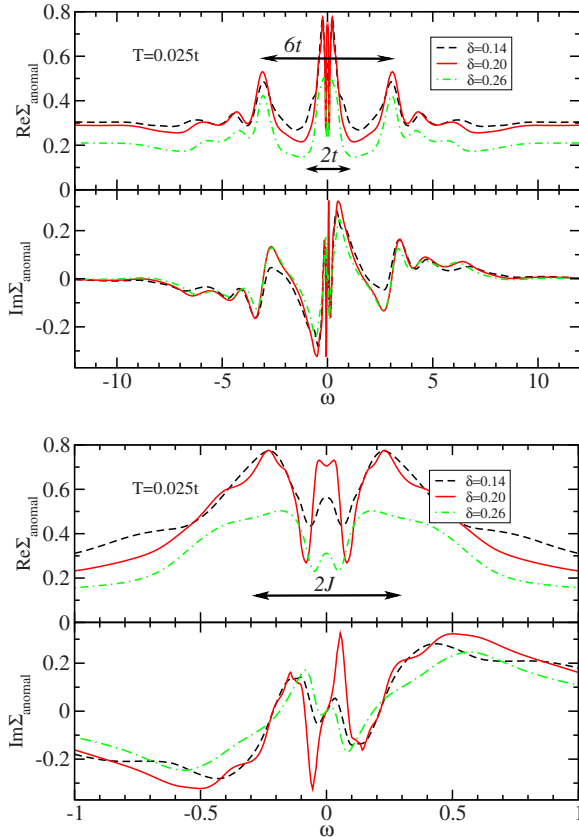

FIG. 22. (Color online) Anomalous self-energy on the real axis within EDCA using NCA as the impurity solver. The top panel shows the extended region in frequency space, while the lowest panel zooms in the low frequency part.

part of the self-energy does not change sign. This indicates that the interaction is attractive over the whole frequency range. There is no characteristic energy corresponding to ω_{Debye}, where the interaction turns from attractive to repulsive. Furthermore, the spectral function displays significant spectral weight not only at a scale of order J but also at the scale of order t, extending all the way to very high frequencies. Several scales can be clearly identified in the anomalous self-energy: the size of the superconducting (SC) gap in one-particle spectra $\sim 0.1t$ (see Fig. 25 and the discussion of the figure later in this section), the spin exchange J, the hopping t, and a scale of the order of half the bandwidth $\sim 3t$.

It is useful to momentum resolve the one-particle spectra at low energies to understand the origin of the low energy quasiparticle excitations in the system. This requires the choice of a periodization scheme. For simplicity, we use the cumulant periodization scheme introduced in Refs. 23, 43, and 44. A more detailed discussion of the periodization problem will be given elsewhere.[91] Here, we focus on the temperature dependence, which requires the finite temperature techniques described in this paper.

The results are shown in Fig. 23. As shown in earlier works,[47,48] C-DMFT is able to produce Fermi arcs in the nodal region. The advantage of the CTQMC technique relative to other solvers is that it allows one to investigate, within CDMFT, the temperature dependence of the arcs. As shown in Fig. 23, the Fermi arcs shrink with decreasing temperature, reminiscent of recent experiments[92] on cuprates. The physical mechanism for the formation of the arcs, and their shrinking with decreasing temperature, is the shift in the real part of the momentum dependent self-energy, which is enhanced in the cumulant periodization. While the validity of this periodization down to zero temperature, with the consequent formation of lines of zeros and Fermi pockets, is at this point a conjecture that deserves further study, there is no question that the formation of the arc and their temperature dependence, at finite temperatures, are robust properties of the cellular DMFT treatment and are visible in other periodizations. Therefore, the results of this paper together with the earlier zero temperature results of Ref. 43 are consistent, at the qualitative level, with both the recent De Haas–Van Alven measurements[93] and photoemission measurements.[92]
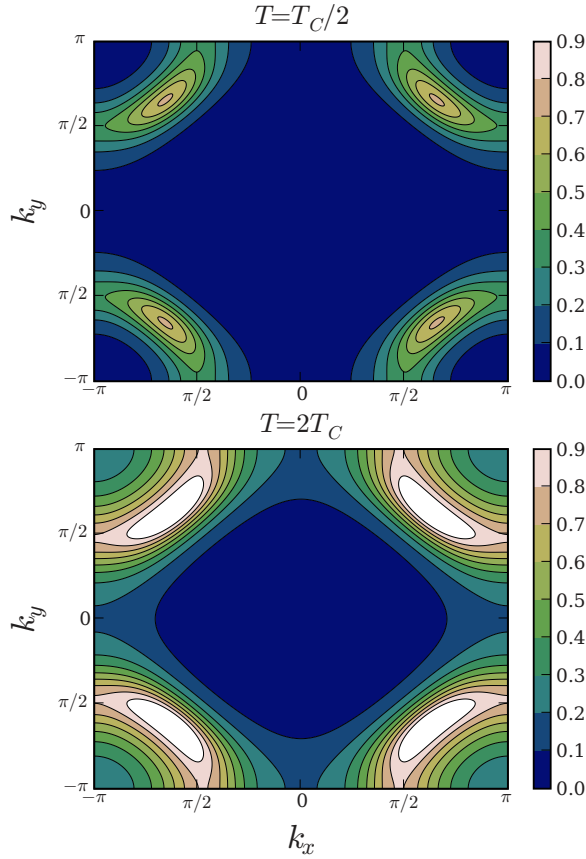
FIG. 23. (Color online) Momentum resolved spectral function in underdoped regime ($\delta = 0.09$) at zero frequency above and below T_C in the (metastable) normal state. We used CTQMC and C-DMFT.

FIG. 24. (Color online) Momentum resolved spectral function in optimally doped regime in superconducting state ($T = T_C/2$) at zero frequency. We used CTQMC and C-DMFT.

With decreasing temperature, the Fermi arcs evolve into a small pocket at a finite distance from a line of zeros, which darkens one side

The arcs are increased with doping and they develop into a banana shape structure. The Fermi surface at optimal doping in the superconducting state is displayed in Fig. 24. Notice the sharp quasiparticles in the nodal region and a gap in the antinodal region.

We now turn to another observable, the superconducting tunneling density of states and its doping dependence displayed in Fig. 25. This quantity has been extensively investigated experimentally.[4] On a broad energy scale, there is considerable particle-hole asymmetry in those curves, and the positive frequency part decreases as we underdope. This is expected on very general grounds for a doped Mott insulator.[94–98]

Remarkably, around optimal doping, $\delta \sim 0.18$, the curves are more particle-hole symmetric at low frequencies. The asymmetry in the superconducting state evolves from the asymmetry of the underlying normal state. To confirm this, we plot the density of states of the underlying normal state with dashed lines in the lower panel of Fig. 25. It is clear from Fig. 25 that the same magnitude of the asymmetry in the superconducting tunneling density of states is present in the normal state local density of states.

The low energy slope of the tunneling density of states is only weakly doping dependent, as was shown in the CDMFT
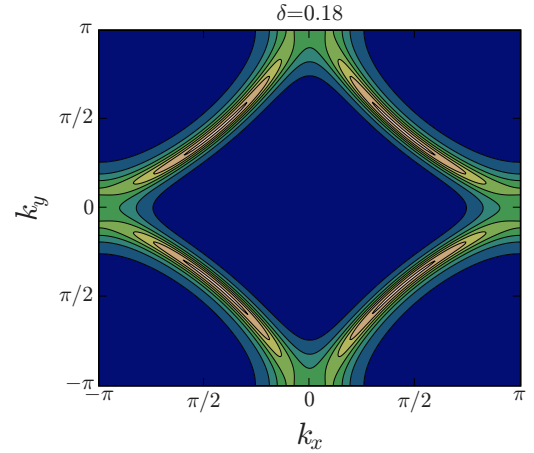
exact diagonalization study of the Hubbard model.[51]

Besides the considerable particle-hole asymmetry at low doping, there are several features in Fig. 25 which are in qualitative agreement with experiments,[9] for example, the dip-hump feature in the tunneling density of states in the unoccupied part of the spectra.

Another surprising aspect of the tunneling is that the increase in the gap with decreasing doping is correlated with a *decrease* in the intensity of the coherence peaks. This is the opposite of what is expected for a BCS superconductor, where the growth in coherence peaks correlates with an increase in the superconducting gap. This observation can also be understood in terms of the two gap picture. The gap in the tunneling density of states (maximum between the coherence peaks) is controlled by the gap originating from the normal component of the self-energy. This gap increases with decreasing doping. On the other hand, the degree of coherence is controlled by the anomalous self-energy, which decreases with decreasing doping as shown in Fig. 25.

The two gap picture of the cuprates has recently emerged from the analysis of numerous experiments.[99–101] It is also part of various phenomenological pictures of cuprate superconductors.[81,82,102] This picture has been recently placed on a microscopic basis by variational cluster approach studies[52] and C-DMFT studies of the Hubbard model.[51]

In the optimally doped regime, the gap value is of the order of $\Delta \sim 0.09t$. This value was obtained from Fig. 25, but similar values result from analytic continuation of CTQMC data to real axis. As discussed above, the critical temperature T_C strongly depends on the cluster scheme employed. Using the maximum T_C of each scheme, we can determine the ratio $2\Delta/T_C$ at optimal doping. In EDCA, $T_C^{EDCA} \sim 0.036t$ and $2\Delta/T_C \sim 5$; in EC-DMFT, $T_C^{EC-DMFT} \sim 0.026t$ and $2\Delta/T_C \sim 7$, and $T_C^{C-DMFT} \sim 0.01t$, therefore $2\Delta/T_C \sim 18$. In conventional superconductors described by BCS theory, this ratio is universally equal to $2\Delta/T_C = 3.5$, but increases in the strong coupling Eliashberg theory. The cluster DMFT superconductivity is, thus in the very strong coupling limit when compared to conventional superconductors. Recent experiments on
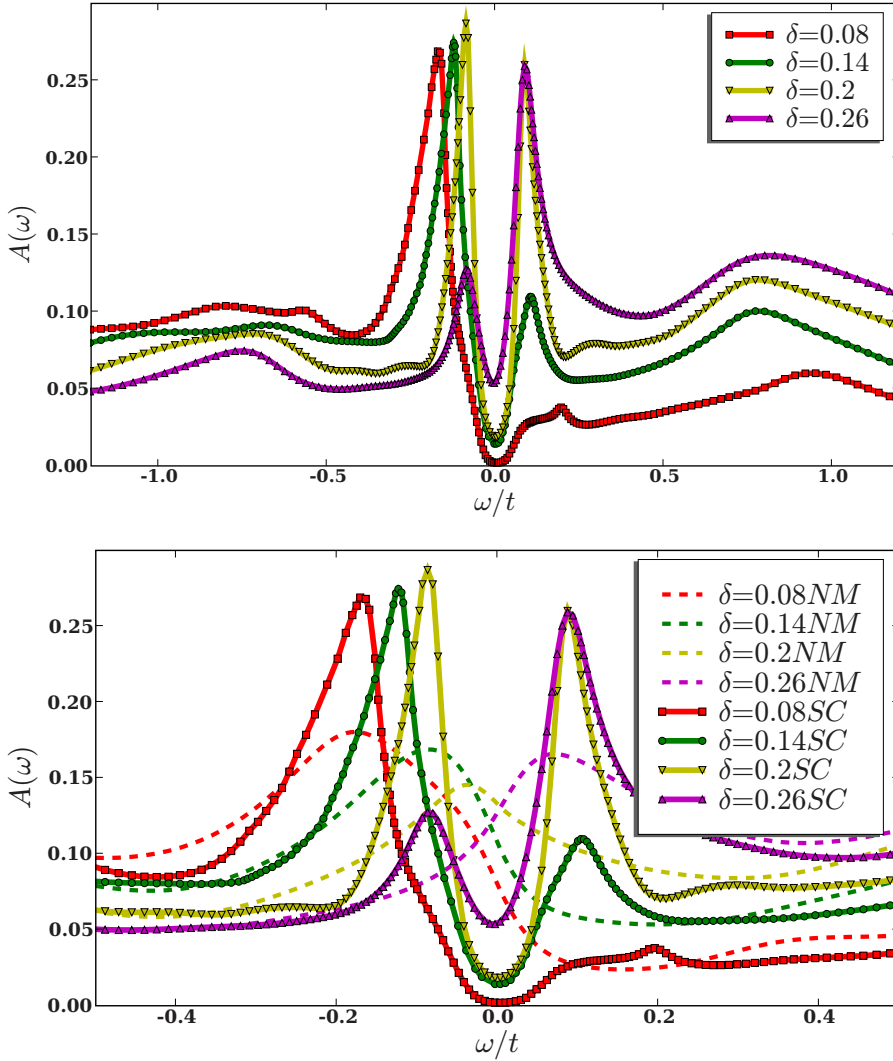
FIG. 25. (Color online) Tunneling density of states (local spectral function) in EDCA obtained with NCA at constant $T = 0.025t$. The lower panel is a blowup of the low energy regions. The dotted lines show the normal state spectral function for the same doping and temperature.

Bi2212 (Ref. 103) seem to suggest that the ratio $2\Delta/T_C$ is close to 8.0, being somewhere between the two limits of extended and nonextended versions of the CDMFT schemes.

In Figs. 27 and 26, we present some insights into the nodal quasiparticles of the Hubbard model as obtained from the CTQMC results shown in Figs. 9 and 12. The self-energy in the nodal region is obtained from the self-energy periodization,[69] i.e.,

$$\Sigma(\mathbf{k}) = \frac{1}{4}[\Sigma_{R=(0,0)} + \Sigma_{R=(1,0)}\cos k_x + \Sigma_{R=(0,1)}\cos k_y$$
$$+ \cos(kx)\cos(ky)\Sigma_{R=(1,1)}]. \tag{42}$$

This allows us to determine the position of the Fermi momentum $\mu - \epsilon_{\mathbf{k}_F} - \Sigma_{\mathbf{k}_F}(\omega=0)=0$ and quasiparticle renormalization amplitude $Z=1/[1-d\Sigma(\mathbf{k}_F)/d\omega]$. In Fig. 26, we plot Z_{nodal} and $\mathbf{k}_F$ along the nodal direction in the superconducting state, where the coherence is established and quasiparticles are well formed. Fermi surface is close to $(\pi/2, \pi/2)$. The renormalization amplitude Z is very slowly increasing with doping in the underdoped and optimally doped regimes,

but has a fast upturn once the normal state becomes more Fermi-liquid-like.

The evolution of the nodal velocities at very low temperatures and its consequences for the superconducting gap in the nodal and antinodal regions were recently studied in Ref. 51 using exact diagonalization as the impurity solver. Here, we confirm all the qualitative trends in the doping dependence of these quantities using the CTQMC solver.

In Fig. 27, we plot the quasiparticle Fermi velocity perpendicular to the Fermi surface and the anomalous velocity parallel to the Fermi surface in the nodal region. The velocities are defined by

$$v_{nodal} = Z_{nodal}\left(\frac{d\epsilon_{\mathbf{k}}}{dk_\perp} + \frac{d\Sigma_{\mathbf{k}}}{dk_\perp}\right), \tag{43}$$

$$v_\Delta = Z_{nodal}\frac{\Sigma_{\mathbf{k}}^{anomal}}{dk_\parallel}. \tag{44}$$

It is clear from Fig. 27 that the nodal velocity is almost constant in the underdoped, optimally doped, and lightly overdoped regimes, compatible with the observation in Ref. 104. The anomalous velocity, however, is domelike shaped
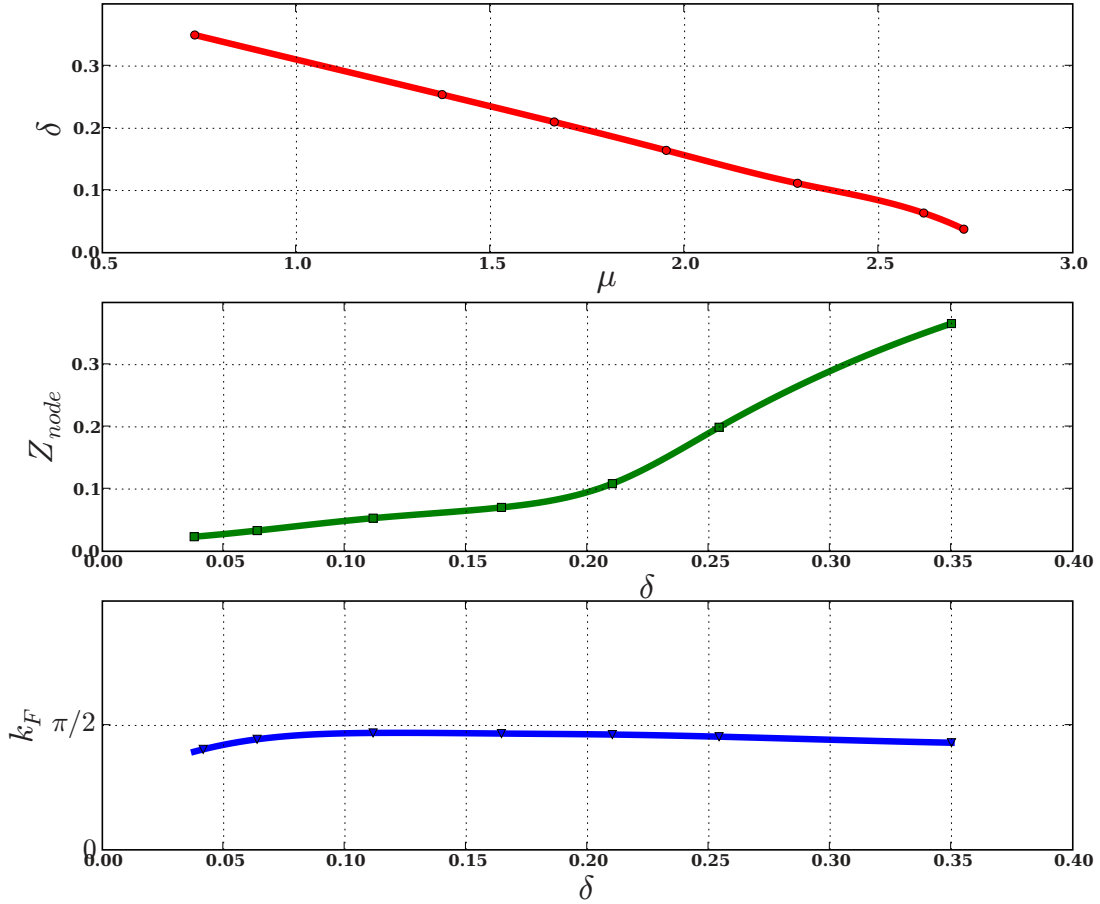
FIG. 26. (Color online) Upper panel: doping versus the chemical potential for the Hubbard model at $T=0.005t$. It shows linear dependence and downturn at small doping. This could point to a divergence of the compressibility zero doping. Middle panel: The nodal quasiparticle residue Z versus doping. It is slowly increasing in the underdoped and optimally doped systems and increases rather rapidly in the overdoped system. Lower panel: Fermi momentum along the nodal direction versus doping.

and tracks the critical temperature. The anomalous velocity measures the slope of the superconducting gap at the node, and its downturn in the underdoped regime suggests that the superconducting gap at the node decreases with decreasing doping. This surprising result is in accordance with recent Raman experiments[100] and angle-resolved photoemission measurements,[101] showing that the superconducting gap at the node in the deeply underdoped regime indeed decreases.

V. OPTICAL CONDUCTIVITY

We now turn to the optical conductivity, which we display in Fig. 28 for the *t-J* model. This quantity has been investigated both theoretically and experimentally over the past 20 years. For reviews, see Refs. 3, 8, and 10. The integrated spectral weight is a measure of the number of carriers, and its evolution with doping has attracted considerable attention.[49,105–112]

The starting point of a theory of the optical conductivity is the Kubo formula,

$$
\sigma(i\omega_n) = \frac{1}{\omega_n}\left[\omega_p^2 \delta_{\alpha\beta} - e^2 \sum_{\mathbf{k}\sigma\mathbf{k}'\sigma'} v_{\mathbf{k}}^\alpha v_{\mathbf{k}'}^\beta \right. \\
\left. \times \int_0^\beta e^{i\omega_n \tau}\langle T_\tau c_{\mathbf{k},\sigma}^\dagger(\tau) c_{\mathbf{k},\sigma}(\tau) c_{\mathbf{k}',\sigma'}^\dagger c_{\mathbf{k}',\sigma'}\rangle \right],
$$

(45)

where the plasma frequency is evaluated from the expectation value of the projected kinetic energy, and the operators c and $c^\dagger$ are projected fermions of the *t-J* model.

In principle, the evaluation of the optical conductivity within CDMFT requires the evaluation of the vertex function, since current vertex corrections are nonvanishing in plaquette C-DMFT. However, for DCA in a plaquette, we have shown that these corrections vanish.[49] This suggests that as a first step in investigating optical conductivity, we can neglect current vertex corrections and evaluate the conductivity from a convolution of the Green's functions,
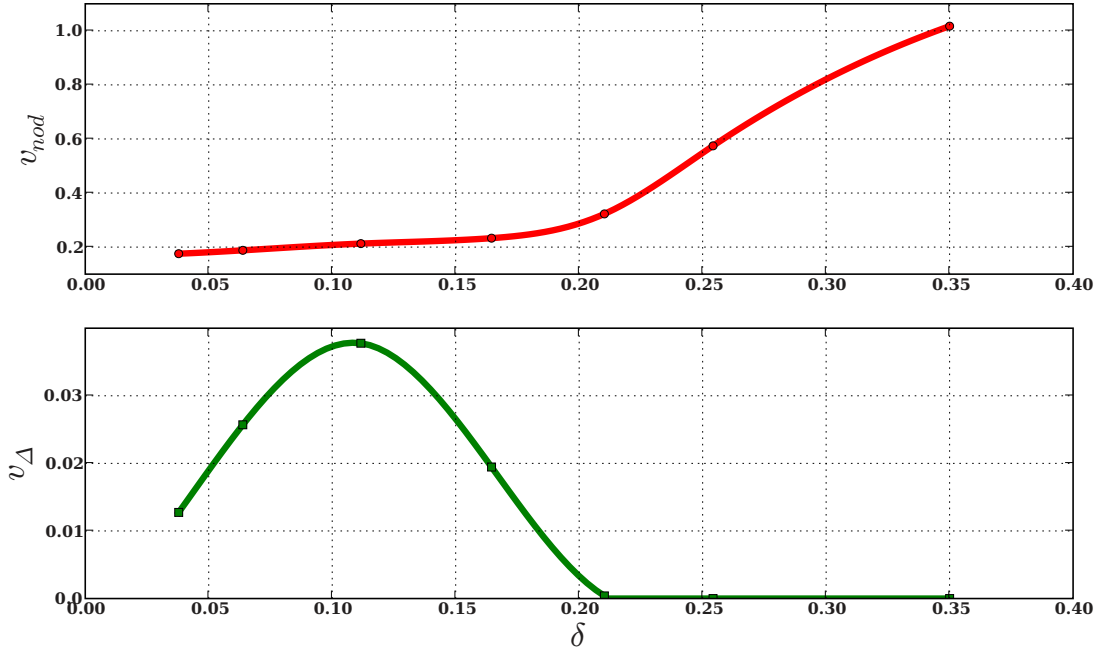
FIG. 27. (Color online) Upper panel: the nodal velocity perpendicular to the Fermi surface versus doping. It is almost flat in the underdoped and optimally doped systems and increases rapidly in the overdoped system. Lower panel: The nodal anomalous velocity parallel to the Fermi surface versus doping has a domelike shape with the peak around optimal doping.

$$\sigma(\omega) = \frac{i\omega_p^2}{\omega} - \frac{ie^2}{\omega}\sum_{\mathbf{k}\sigma} v_{\mathbf{k}}^2 \int \frac{dx}{\pi} f(x)[\mathcal{G}_{\mathbf{k}}(x + \omega + i\delta)\mathcal{G}_{\mathbf{k}}''(x)$$

$$+ \mathcal{G}_{\mathbf{k}}''(x)\mathcal{G}_{\mathbf{k}}(x - \omega - i\delta) + \mathcal{F}_{\mathbf{k}}^\dagger(x + \omega + i\delta)\mathcal{F}_{\mathbf{k}}'(x)$$

$$+ \mathcal{F}_{\mathbf{k}}^{\dagger''}(x)\mathcal{F}_{\mathbf{k}}(x - \omega - i\delta)]. \tag{46}$$

Within C-DMFT, in the regime where the NCA solvers can be used, the f-sum rule

$$\int_0^\infty \sigma'(x)dx = \frac{\pi e^2}{4} \sum_{\mathbf{k},\sigma,\alpha=(x,y)} \left[\frac{d^2\varepsilon_{\mathbf{k}}}{dk_\alpha^2}\right] n_{\mathbf{k}\sigma} \tag{47}$$

is obeyed within a few percent, suggesting that even for C-DMFT, where the vertex corrections are nonvanishing, the
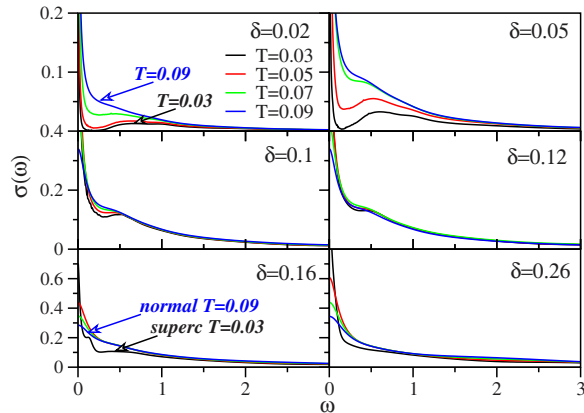

FIG. 28. (Color online) Optical conductivity at different dopings and temperatures within EDCA using NCA for the t-J model. The optical conductivity evolves from a sum of two distinct features at low dopings to a broad Drude feature at high dopings.

corrections introduced by this effect are small. Notice that the right-hand side of Eq. (47) is proportional to the kinetic energy of the low energy model if this model contains nearest-neighbor hopping only.

Formula (46) depends on the momentum dependent Green's function and, therefore, on the periodization scheme used and the cluster method employed. The qualitative features discussed in this paper and the behavior of the integrated quantities are common to all methods.

The optical conductivity has been modeled as either a one component or a two component system via an extended Drude analysis.[113,114] The two component parametrization consists of a Drude peak and a midinfrared feature.

The cluster DMFT results for the optical conductivity of the t-J model are shown in Fig. 28. We show the evolution of the optical conductivity with doping at various temperatures. In the very underdoped regime, there are clearly two components to the optical conductivity with an optical pseudogap, opening as a function of temperature. On the other hand, beyond $\delta=0.1$, one can describe the optics in terms of one broad feature which narrows as the temperature is reduced.

It is customary to parametrize the optical conductivity in terms of a generalized Drude model

$$\sigma(\omega) = \frac{\omega_p^2}{4\pi} \frac{1}{\dfrac{1}{\tau(\omega)} + i\omega\dfrac{m^*(\omega)}{m}}. \tag{48}$$

This parametrization relates the real and imaginary parts of the optical conductivity *in a given energy range* to two functions $\frac{1}{\tau(\omega)\omega_p^2}$ and $\frac{m^*(\omega)}{m\omega_p^2}$ via

$$\frac{1}{\tau(\omega)\omega_p^2} = \frac{1}{4\pi}\frac{\sigma'}{\sigma'^2 + \sigma''^2}, \tag{49}$$

$$\frac{m^*(\omega)}{m\omega_p^2} = \frac{1}{4\pi}\frac{1}{\omega}\frac{\sigma''}{\sigma'^2 + \sigma''^2}. \tag{50}$$

The quantity ω_p^2 is determined from a requirement involving the energy range in which the parametrization is used, namely,

$$\frac{\omega_p^2}{8} = \int_0^\Lambda \sigma'(\omega)d\omega, \tag{51}$$

where Λ is the high energy cutoff.

Figure 29 describes the evolution of the plasma frequency and effective mass versus doping in the *t-J* model. The plasma frequency vanishes at half-filling and linearly increases at low doping. The optical mass is weakly doping dependent and changes from approximately 3 in the overdoped regime to 5 in the underdoped regime, with the largest slope at optimal doping. Weak doping dependence of the effective mass of the same magnitude was pointed out in Ref. 114.

Given a parametrization of the optical conductivity as a sum of a few poles, the optical mass measures the ratio of the total spectral weight compared to the weight in the zero energy pole, representing the Drude peak. If the transitions between the upper and lower Hubbard bands of the Hubbard model are included in ω_p, i.e., $\Lambda > U$, then ω_p is finite on approaching the Mott transition and, consequently, the optical mass diverges. On the other hand, excluding transitions between the Hubbard bands results in ω_p vanishing as the
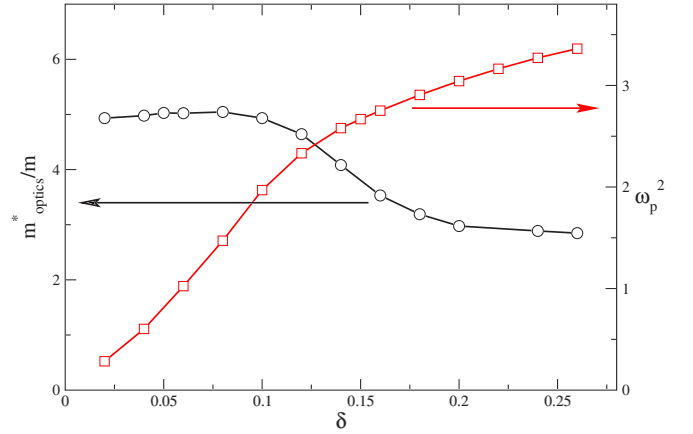

FIG. 29. (Color online) Effective mass and plasma frequency as a function of doping. Obtained from optical conductivity of Fig. 28.

Mott transition is approached. In the *t-J* model, the upper Hubbard band is projected out, therefore the optical mass is always finite. As long as the transitions into the upper Hubbard band are excluded, the plasma frequencies ω_p of cluster DMFT and single site DMFT are not too different. Notice, however, that m^*/m is enhanced in cluster DMFT relative to single site DMFT (not shown) because superexchange transfers optical weight from the low energy to the intermediate energy range $\sim J$.

The optical spectral weight ω_p^2 is, in general, a function of temperature and cutoff Λ, i.e.,

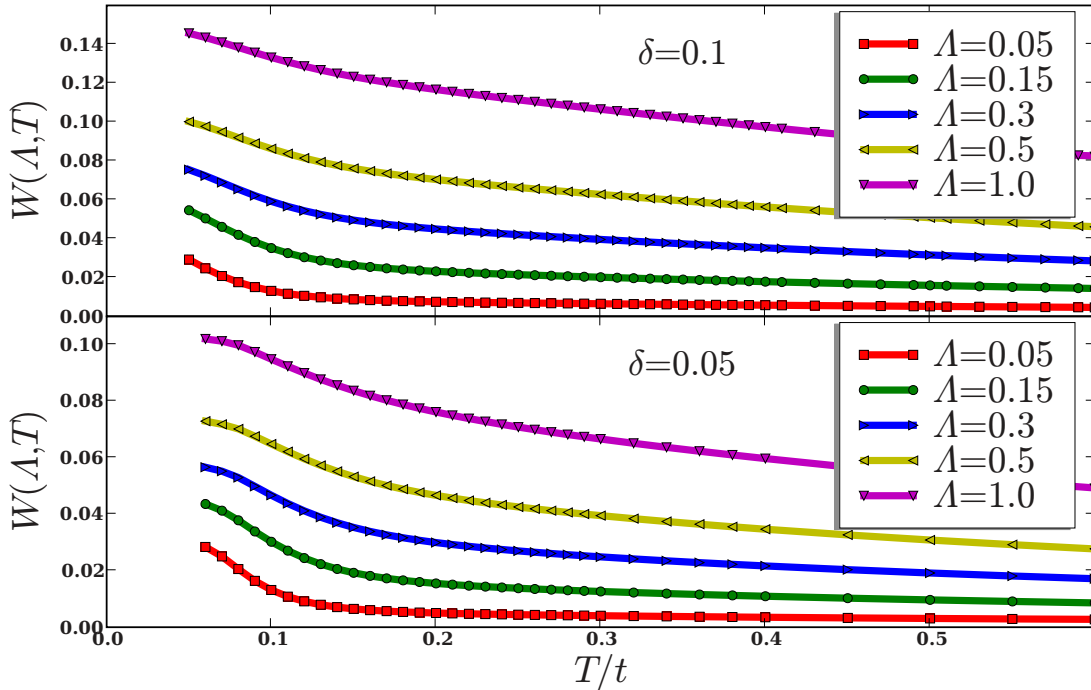$$\frac{\omega_p^2}{8} = W(\Lambda, T). \tag{52}$$

FIG. 30. (Color online) Integrated spectral weight in the normal state as a function of temperature in the underdoped regime for a few different cutoff frequencies. EDCA and NCA were used.
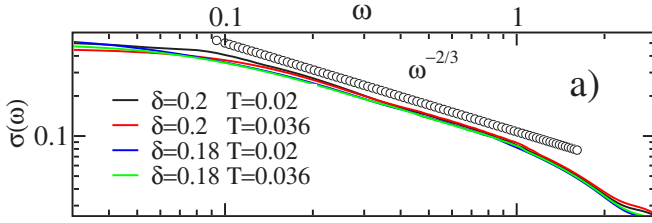
FIG. 31. (Color online) The optical conductivity $\sigma(\omega)$ of the t-J model is proportional to $\omega^{-2/3}$ in the intermediate frequency region for the optimally doped system.

In experiment, the cutoff is usually chosen such that the interband transitions are absent ($\Lambda \sim 1$ eV). The interband transitions or transitions into the upper Hubbard band are absent in the t-J model, therefore this requirement is taken into account automatically.

The optical pseudogap which separates the two components of spectra and is seen as a dip at the scale of J in Fig. 28 is quite large in the underdoped system, $\delta \sim 0.05$. One could expect that the integral spectral weight $W(\Lambda)$ for small enough $\Lambda \sim J$ might start to decrease below a certain characteristic temperature of a pseudogap. However, as shown in Fig. 30 there is no sign of such a decrease for any cutoff frequency Λ or any temperature. Although the pseudogap gap clearly increases with temperature, the Drude peak more than compensates for this spectral weight loss and W increases as T decreases.

Near optimal doping, the optical conductivity displays remarkable power laws in an intermediate asymptotic regime. These power laws were first pointed out by El Azrak *et al.* in Ref. 115. The power laws, and the possibility of a connection with an underlying quantum criticality, have been a subject of several recent experimental papers.[116] CDMFT provides a natural explanation for these anomalies.[49] These power laws were seen in exact diagonalization of much larger systems,[117] indicating again the power of the cluster DMFT when it can be compared with available exact results. The power of the optical conductivity is very close to 2/3 as seen in Fig. 31, but an analytic derivation of this result is not available.

A surprising aspect of the physics of strongly correlated materials is that low energy phenomena affect the spectra of the material over a very large energy scale. This general phenomenon is illustrated in Fig. 32, which shows the integral of optical spectral weight $W(\Lambda)$ in the normal and the superconducting state. Low energy phenomena, like the onset of superconductivity which involves a scale of a fraction of J, involves redistribution of optical weight of the order of $4t \approx 1$ eV, which is 40 times more than the gap value. A theoretical insight from our calculation is that the high frequency redistribution of weight comes from the anomalous Green's function $\mathcal{F}*\mathcal{F}$ in Eq. (46) and, hence, cannot be observed in the density of states or angle-resolved photoelectron spectroscopy measurements. The large range of redistribution of spectral weight has also been measured on cuprates and pointed out in Refs. 105 and 108.

It is useful to compare the results for the temperature dependence of the integrated spectral weight of cluster DMFT with those of single site DMFT as reported by Toschi *et al.*[118] These are displayed in Fig. 33. There are two important observations: first, the sign and the order of magnitude of the effect are similar in single site and in cluster DMFT. This indicates that local quantities can be reliably computed in this framework and do not change dramatically as the sizes of the cluster is increased. Second, the doping dependence of this low energy kinetic energy difference $W(0) - W(300 \text{ K})$ has a slope in cluster DMFT opposite to that in single site DMFT. An interesting question is whether the existing experimental data agree better with the single site or cluster DMFT. It seems that the results in Refs. 119–121 are in better agreement with the plaquette DMFT, but a more detailed comparison between theory and experiment is left for future studies using the more realistic band structure of each compound and a more precise periodization scheme.

We can also compute the temperature dependent resistivity using EDCA, in which the vertex correction vanish,

$$\frac{1}{\rho(T)} = e^2 \sum_{\mathbf{k}\sigma} v_{\mathbf{k}}^2 \int \frac{dx}{\pi} \left[-\frac{df(x)}{dx} \right] [\mathcal{G}_{\mathbf{k}\sigma}''(x)^2 + \mathcal{F}_{\mathbf{k}\sigma}''(x)^2].$$

(53)

Notice that while the scattering rates at zero frequency tend to saturate at high temperature (see Fig. 17), the resistivities do not, as seen in Fig. 34.
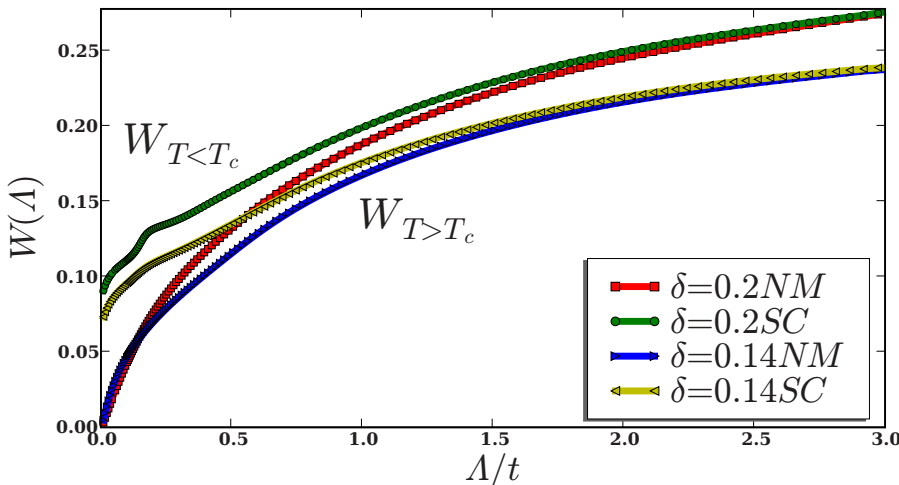

FIG. 32. (Color online) Superconducting and normal integrated spectral weights (N_{eff}) as a function of cutoff frequency. Optical spectral weight which collapses to delta function in the superconducting state comes from a very extended energy interval ($\sim 3t$). We employed EDCA and NCA.
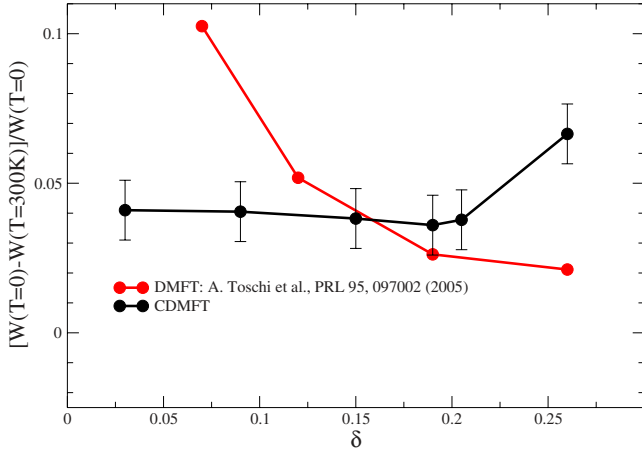
FIG. 33. (Color online) Difference between the low temperature and 300 K optical spectral weights integrated up to $\Lambda = 6t$. The cluster data are computed within EDCA, and the single site DMFT results are reproduced from Ref. 123. The error bars are due to the extrapolation of spectral weight to zero temperature from finite temperature results ($T_{min} \sim 0.5 T_C$).

Notice that the scaling of the resistivity with the number of holes is approximately obeyed, and that the maximum amount of linearity is obtained near optimal doping. More detailed comparison with experiments will require a more realistic modeling of the band structure and a detailed investigation of the dependence of this quantity on the periodization scheme used.

Finally, since we have access to both the real and imaginary parts of the optical conductivity, we can compute the superconducting stiffness, defined as the strength of the delta function peak in the superconducting state. Its temperature and doping dependence close to T_C is displayed in Fig. 35. In
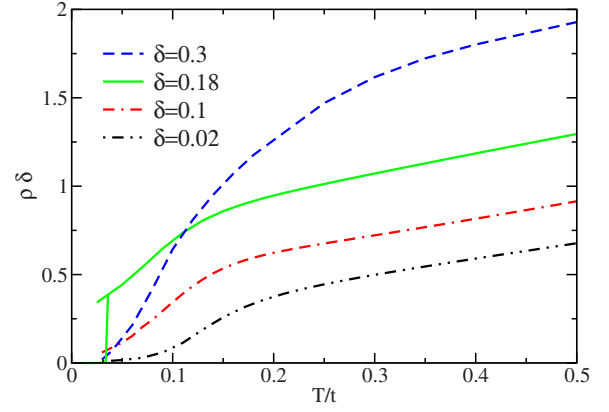

FIG. 34. (Color online) Resistivity versus temperature in EDCA using NCA as the impurity solver.

optimally doped and overdoped regimes, stiffness is a linear function of temperature close to the transition, while it is substantially reduced in the underdoped regime due to the opening of the pseudogap. A similar trend was found in cuprates as pointed out in Ref. 122.

With NCA, we are not able to reach sufficiently low temperatures to address the crucial issue of the doping dependence of the linear term of the superfluid stiffness. Instead, we use the techniques in Sec. IV to evaluate the low temperature behavior of this quantity,

$$\rho_s(0) - \rho_s(T) = \frac{b}{\pi} T = e^2 \frac{2 \log 2}{\pi^2} k_B T \frac{Z_n^2 v_0^2}{v_F v_\Delta}, \qquad (54)$$

where Z_n, v_Δ, and v_F were evaluated in Sec. IV, and v_0 is the band Fermi velocity. The coefficient b can be evaluated di-
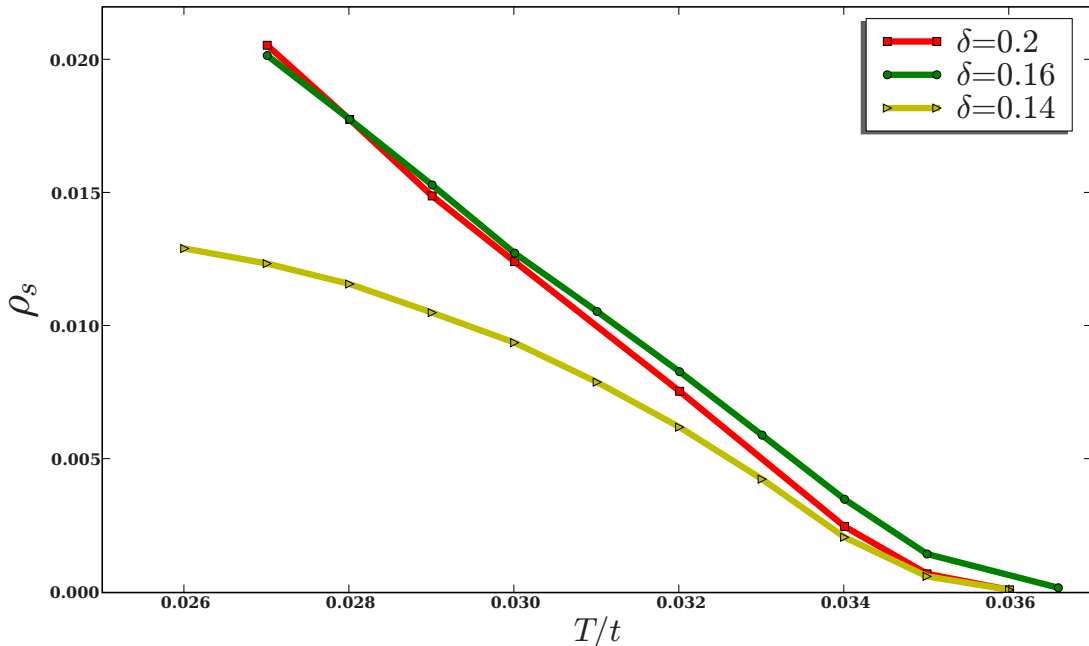

FIG. 35. (Color online) Superconducting stiffness versus temperature as obtained from optical conductivity using NCA and EDCA.
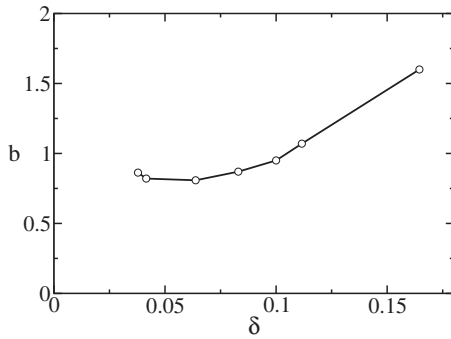
FIG. 36. Coefficient of the linear term of the superconducting stiffness $\pi[\rho_s(0)-\rho_s(T)]/T$ versus doping for the Hubbard model using CTMQC.

FIG. 37. (Color online) The cluster spin susceptibilities of the t-J model versus temperature at two different dopings obtained by EDCA and NCA.

rectly from the imaginary axis data of CTQMC and is plotted in Fig. 36.

CDMF captures the weak dependence of b on doping, which was a subject of intensive experimental investigations.[123,124] More detailed studies of this quantity in C-DMFT, including vertex corrections, and more detailed investigations of the periodization dependence of this quantity, as well as the related $B1g$ slope of the Raman scattering,[104] are certainly warranted.

VI. MAGNETISM SUPERCONDUCTIVITY AND SPIN RESONANCE

In this section, we turn to the magnetic properties, starting from the cluster magnetic quantities.[8,125,126] As in the rest of the paper, we confine ourselves to the study of minimal models; in this section, the t-J model with $t'=0$. Notice, however, that it is known from numerous studies that the presence of a next-nearest-neighbor hopping t' affects significantly the region of stability of the magnetism and can suppress it altogether.[48]

The static cluster susceptibilities are displayed in Fig. 37. These are coarse-grained versions of the momentum dependent magnetic susceptibility, over the different regions of the Brillouin zone of the size of one-quarter of the first Brillouin zone. While the cluster susceptibilities are relatively smooth functions of doping, they clearly demonstrate that the spin fluctuations in different regions of the Brillouin zone have
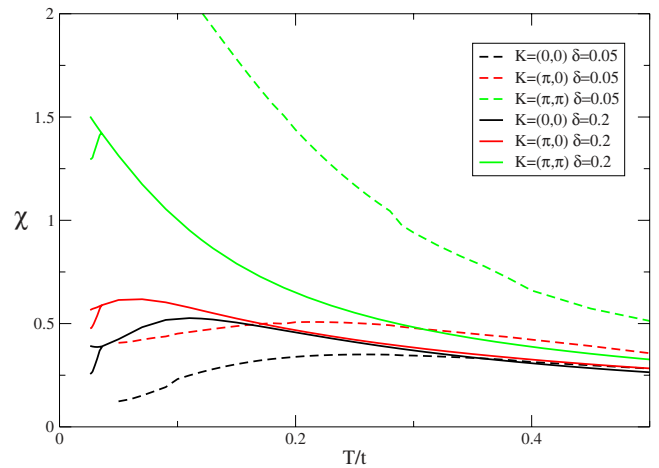
dramatically different behaviors with doping and temperature. The (π,π) component, dominated by the $\chi_{\pi\pi}$ susceptibility, strongly increases as we approach half-filling. In contrast, the uniform component χ_{00} decreases as doping is reduced, a signal of the opening of the pseudogap. The same is true of $\chi_{\pi0}$. Hence, an interesting property of the pseudogap state is the increase of staggered magnetic fluctuations with the opening of the pseudogap. A similar contrast between the staggered and uniform responses is seen in their temperature dependence. We see that while the uniform response decreases with temperature in the underdoped regime, the staggered response increases.

We now proceed to uniform spin susceptibility shown in Fig. 38. The $\mathbf{q}=0$ susceptibility at zero doping displays the characteristic behavior of the Heisenberg model, with a Curie-like behavior at high temperatures and a broad maximum at a scale of the order of J as the spins begin to form singlets. The main effect of doping is to reduce the effective exchange. Experimentally, the shift of the minima in the susceptibility is seen,[127,128] but it occurs faster than in Fig. 38. The effective spin exchange will be reduced by the addition of a negative next-nearest-neighbor hopping t' to the model.

We now turn to the frequency dependence of the imaginary part of the (π,π) susceptibility probed in neutron scat-
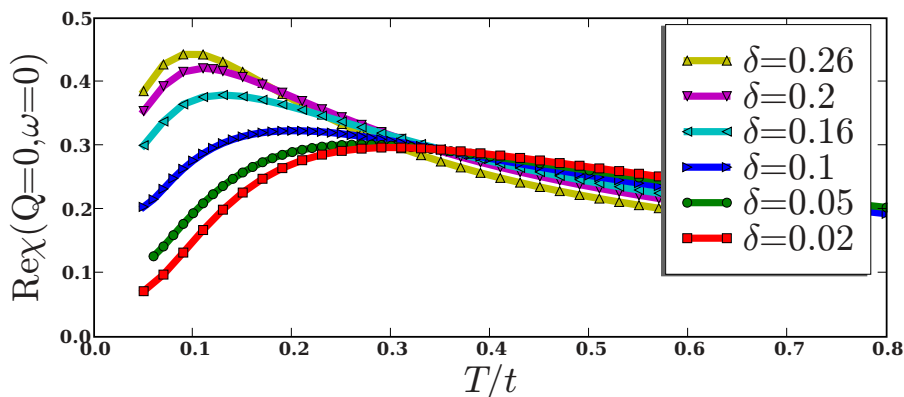

FIG. 38. (Color online) The $\mathbf{Q}=0$ cluster spin susceptibility versus temperature at different dopings for the t-J model within EDCA.
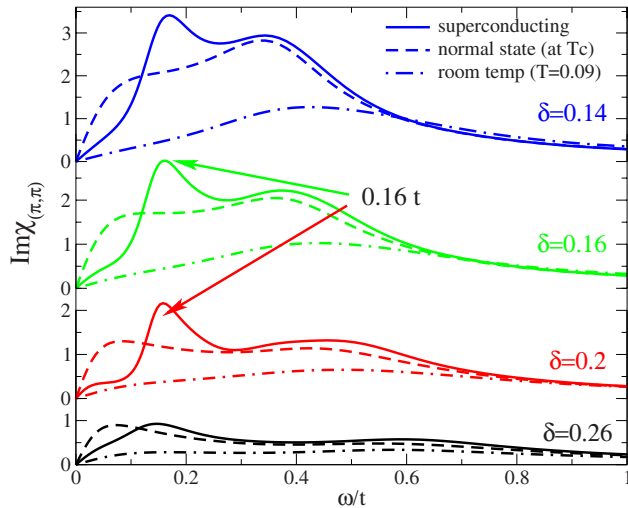
FIG. 39. (Color online) The dynamical spin susceptibility at **q** $=(\pi,\pi)$ for a few different doping levels and three different temperatures: superconducting state and normal state at the transition temperature and at room temperature. The pronounced peak is formed in the SC state at $0.16t \approx 48$ meV, and a broad peak in the normal state is around $100-140$ meV. Susceptibility at normal temperature is much smaller, and the peak moves to higher frequencies. The resonance is strongest at the optimally doped system. It disappears quickly in the overdoped side and somewhat more slowly in the underdoped side. Results are obtained with EDCA and NCA.

tering experiments. As shown in Fig. 39, a pronounced peak in the (π,π) spin response at frequency $0.16t$ in the optimally doped regime can be observed when entering the superconducting state. The position of the peak is temperature independent, but depends weakly on doping, tracking the critical temperature. Our results are in qualitative agreement with experiment; for example, the resonance energy scales with doping like $5T_C$ and its position does not depend on temperature.[125] In addition, we see a broader peak around $(0.35-0.45)t$ extending to very high frequencies of order of $t \approx 300$ meV, which also gains some weight when entering the superconducting state.

Cluster methods coarse grain the momentum dependence. In the plaquette case, the coarse graining is done over $1/4$ of the Brillouin zone, centered at (π,π); therefore, it is reasonable to compare our results with the **q** integrated susceptibility from Ref. 129, where the two features, present in the mean-field theory, 35 meV resonant peak as well as broader peak around 75 meV extending up to 220 meV, were observed.

The exchange energy of the t-J model can be expressed as an integral of the spin susceptibility,[130]

$$E_{xc} = \frac{3J}{\pi} \int d^2\mathbf{q}\, d\omega\, b(\omega) \mathrm{Im}[\chi(\mathbf{q},\omega)](\cos q_x + \cos q_y).$$

(55)

Using this equation, one can elucidate the origin of the superconducting condensation energy and the relative contribution of the different features of the spectral function.

Clearly, an important contribution to superconducting condensation energy arises from the incoherent features of the spin spectral function [around the frequency $(0.4-0.5)t$] rather than from the spin resonance.

The exchange energy as a function of temperature is shown in Fig. 40. At high temperature, spins are disordered and the exchange energy is negligible. At temperature below J, the singlets are formed and the exchange energy noticeably decreases, especially in the underdoped regime. At T_C, the exchange energy decreases further and gives, by far, the largest contribution to the condensation energy of the t-J model, as shown in Ref. 49. The exchange energy mechanism, observed in cluster DMFT study, is thus in agreement with the strong coupling magnetic mechanism for the superconductivity.

The spin resonance has been viewed from two different perspectives (see Ref. 125 and references therein): (i) starting from electronic quasiparticles and their residual interactions in a d-wave superconductor, residual interactions form a particle-hole bound state with spin 1, which is identified as the spin resonance. (ii) Alternatively, starting from a disordered quantum spin system, one can identify the spin resonance as a massive spin 1 excitation, which becomes massless as one approaches the magnetically ordered phase.

The cluster EDMFT Eq. (7) reconciles both points of view in a unified approach, since the equations for the spin susceptibility contain both the exchange interaction characteristic of the insulator $J(q)$ and the quasiparticle contribution described by the spin cumulant M [Eq. (7)].

The appearance of the spin resonance requires the dramatic decrease of the anomalously large scattering rate in the normal state, which is strongly reduced when the electrons condense to form d-wave pairs, avoiding criticality at low temperatures. The resonance, however, appears only in the superconducting state and is not present in the normal state.

VII. PSEUDOPARTICLE INTERPRETATION: CONNECTION WITH OTHER MEAN-FIELD THEORIES

In this section, we give an interpretation of physical observables in terms of pseudoparticle (eigenstates of the cluster) spectral functions. This is an alternative insight into a rich physics contained in the solution of cluster DMFT equations on a plaquette.

Pseudoparticle creation and annihilation operators were introduced as mathematical entities representing the atomic eigenstates of the plaquette immersed in the cluster DMFT medium. We have found that out of the large number (3^4) of pseudoparticles that we introduced, very few of them are important for reproducing the low energy part of physical observables. For example, more than 95% of the one-particle spectral function at the Fermi level comes from a few convolutions of pseudoparticles in Eq. (33), within NCA approach. This constraint is, however, not present for the high energy part of the spectra such as Hubbard bands, where the contribution of most of the pseudoparticles can be identified. The ground state and the low lying excitations are much more restricted and are a superposition of only a few atomic states. In the plaquette, these important states are
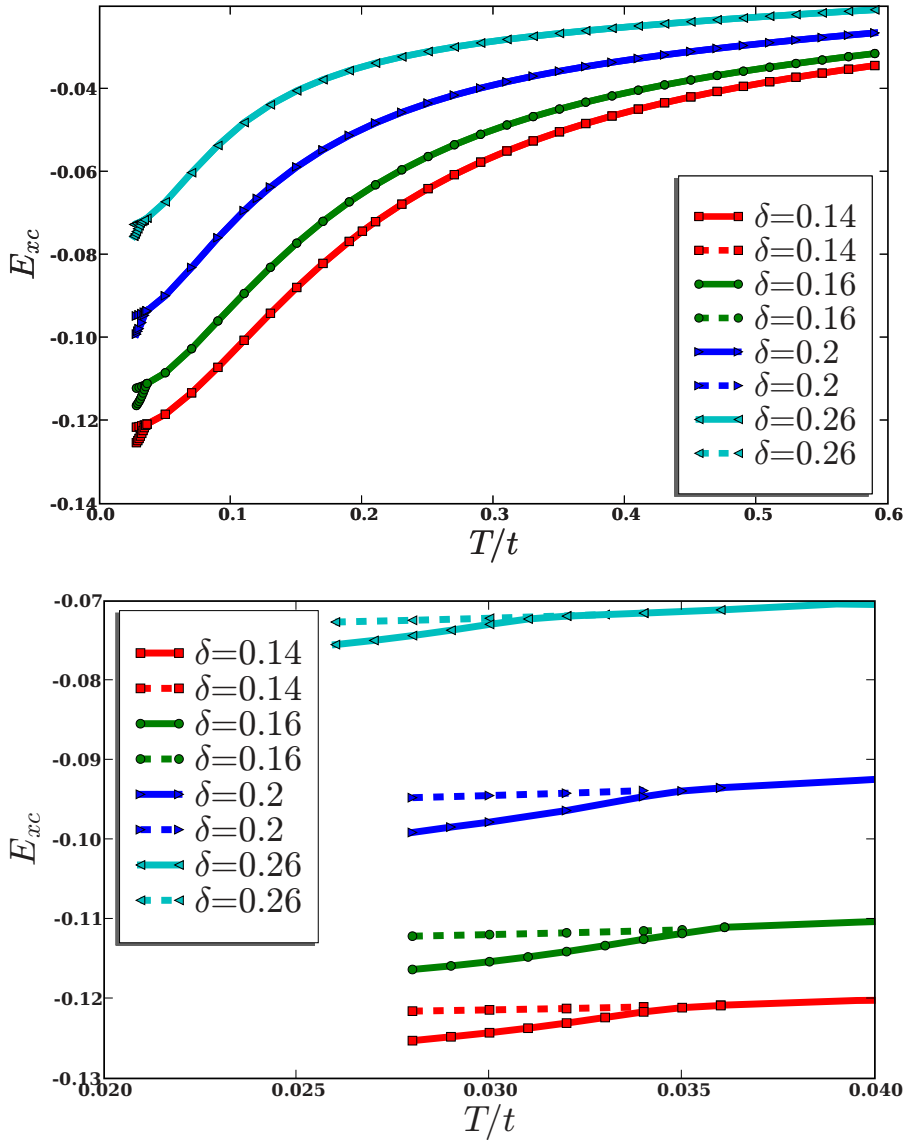
FIG. 40. (Color online) The exchange energy versus temperature for a few doping levels obtained by the NCA in EDCA. The lower panel is a blowup of the low temperature regime. The dotted lines correspond to the metastable normal state below T_C, while the full lines continue into the superconducting state.

$$\Gamma_4 = |N=4, S=0, K=0\rangle, \tag{56}$$

$$\Gamma_{4'} = |N=4, S=1, K=(\pi\pi)\rangle, \tag{57}$$

$$\Gamma_{3\sigma(\pi 0)} = |N=3, S=1/2, S_z=\sigma, K=(\pi,0)\rangle, \tag{58}$$

$$\Gamma_{3\sigma(0\pi)} = |N=3, S=1/2, S_z=\sigma', K=(0\pi)\rangle, \tag{59}$$

$$\Gamma_2 = |N=2, S=0, K=0\rangle, \tag{60}$$

where N is the number of electrons in the cluster eigenstate, S and S_z are the total spin and its z component of the cluster eigenstate, and K is the momentum of the cluster eigenstate.

Notice that although only a few cluster eigenstates contribute to the ground state, the wave function is still highly nontrivial since it is a product state of an infinite number of states in the bath and the few atomic eigenstates of the impurity. This surprising result of restriction to a few cluster eigenstates could be beneficial to devise useful approximations while extending C-DMFT to larger clusters in the fu-

ture. In this paper, we exploit this fact to give a simple interpretation of the different doping regimes of the *t-J* model.

Figure 41 (left) shows the evolution of the three most important pseudoparticle spectral functions from the underdoped to the overdoped regime.

At small doping, the cluster is mostly occupied by the singlet state with one particle per site and zero momentum $\Gamma_4 = |N=4, S=0, K=0\rangle$ (half-filled singlet). This pseudoparticle has the largest occupancy as shown in Fig. 41. It describes a system locked in a short-range singlet state as a consequence of the strong superexchange interaction.

The cluster electron spectral function describes the process of addition and removal of an electron from the cluster at frequency ω. Within NCA, it is constructed from the convolution of two pseudoparticles with different cluster occupations N and $N+1$, or $N-1$, with the frequency restricted between zero and ω as described by Eq. (33). The necessary condition for a peak of the one-particle spectral function at the Fermi level is that at least two pseudoparticle spectral functions share a common threshold and are strongly peaked at the same threshold.
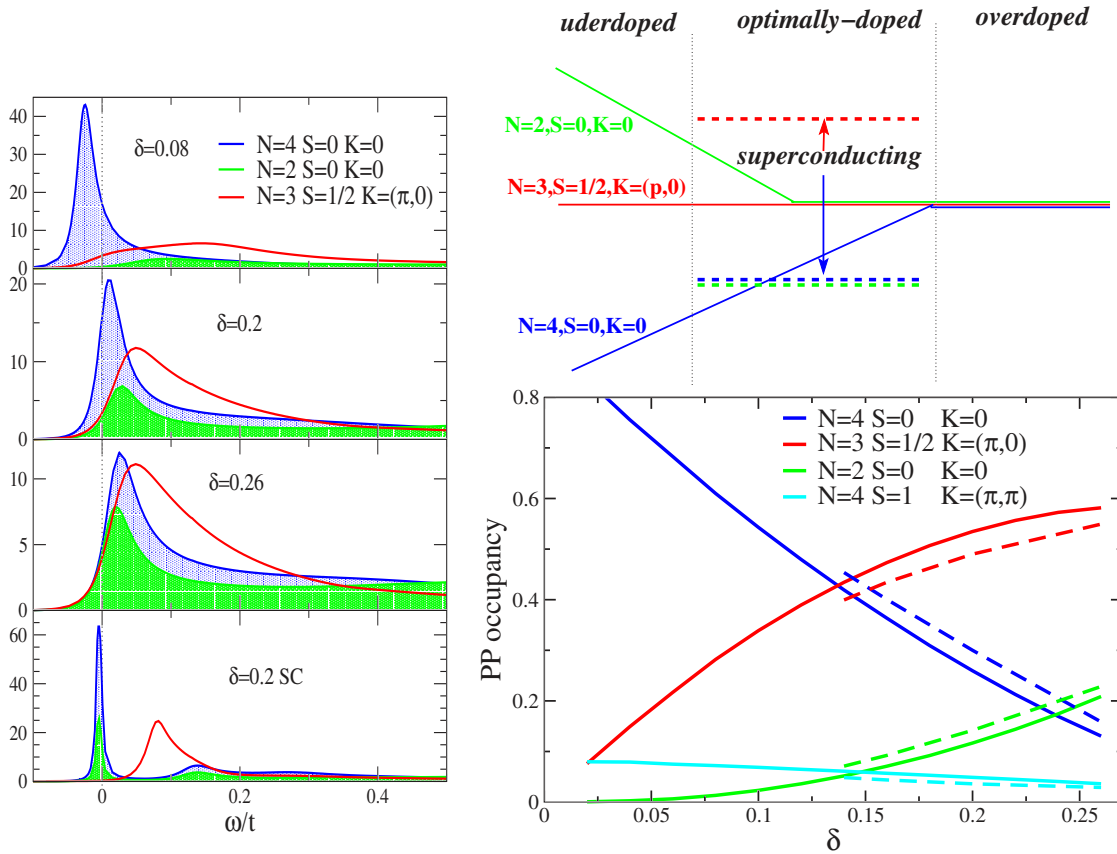
FIG. 41. (Color online) Left: Pseudoparticle spectral functions for the three most important pseudoparticles: ground states for $N=4$, $N=3$, and $N=2$ sectors. Right, top: Sketch of pseudoparticle threshold energies which can be interpreted as the effective many-body levels in the normal and superconducting states. Right, bottom: Pseudoparticle occupancies versus doping for the most important pseudoparticles. The full lines correspond to the normal state, while the dashed lines correspond to the superconducting state.

In the *underdoped regime*, the thresholds of all other pseudoparticles except Γ_4 are significantly shifted with reference to the half-filled singlet; a pseudogap results in the one-particle spectra in the underdoped regime. This gap in threshold energies severely limits the possible decay processes of the electron, resulting in a low electronic scattering rate. This is the plaquette-impurity model of a few holes propagating in a sea of singlets.

At large doping, i.e., in the *overdoped regime*, where the Kondo scale is dominant, we obtain the standard DMFT description of a strongly correlated Fermi liquid. As is well known from the study of the Fermi-liquid regime of the single impurity Anderson model, all pseudoparticles develop thresholds (x-ray singularity) at the same frequency which is related to the Kondo temperature of the problem. In our plaquette DMFT, all three important pseudoparticles (half-filled singlet, doublet with one hole per plaquette $\Gamma_{3\sigma K}$, and singlet with two holes per plaquette Γ_2) have a power law divergence at the same threshold frequency at zero temperature (Fig. 41), which is a standard signature of the Kondo effect. Hence, the one-particle spectral function begins to develop the Kondo-Suhl resonance at the Fermi level since the convolution between the doublet $\Gamma_{3\sigma K}$ and half-filled singlet Γ_4 (or Γ_2 singlet) states is large at low frequency. The one-particle spectral function is peaked slightly above the Fermi level. Notice that while we cannot follow the forma-

tion of the Kondo resonance to very low temperatures due to the well known NCA pathologies, we can clearly see the onset of the Fermi-liquid behavior in Fig. 13. The overdoped regime characterized by the common threshold of pseudoparticles is distinctively different from the underdoped regime, where the only important states are the half-filled singlet Γ_4 and the $\Gamma_{3\sigma K}$ doublet. The latter has a very little spectral weight in the region of the singlet peak.

Transition region: Normal state. In the optimally doped regime, the Kondo scale and the superexchange compete, giving rise to a regime with very large scattering rate and, consequently, a small coherence scale.

Surprisingly, the evolution of the spectral function with doping is such that the optimally doped regime is approximately particle-hole symmetric. As shown in Fig. 41 (right, top), the thresholds of the $N=2$ cluster ground state and $N=3$ cluster ground state (doublet) merge first, resulting in a Kondo-like contribution to the electron spectral function. This contribution is peaked above the Fermi level in a one band model below half-filling in a Fermi-liquid regime. The half-filled singlet, however, remains the lowest state in energy and still gives a significant contribution to the electron spectral function. The latter contribution is peaked below the Fermi level and keeps a pseudo-gap-like shape. Adding the two contributions to the electron spectral function restores the particle-hole symmetry in the density of states both in

normal and superconducting states at optimal doping [see Figs. 13(g) and 25]. The approximate restoration is important, because it is known that clusters of impurities such as the two impurity Kondo model[131] have a critical point only in the particle-hole symmetric case.[132]

Notice that the point of maximum scattering rate in Fig. 17 coincides with the merging of the thresholds of the pseudoparticles (see Fig. 41). Around the same doping level, an approximate particle-hole symmetry is restored in one-particle Green's function (see Figs. 6 and 13). Hence, the term avoided cluster quantum multicriticality describes better the phenomena observed in this study since, to reach the quantum critical point, both the particle-hole symmetry and the ratio of Kondo to RKKY coupling need to be varied.

Transition into the superconducting state. The degeneracy responsible for the strongly incoherent metal with large scattering rate at the Fermi level is lifted by the superconductivity, avoiding the critical point. This dramatic reduction of scattering rate in going from the normal to the superconducting phase, depicted in Figs. 17 and 18, highlights how anomalously incoherent the normal state at optimal doping is and how those anomalies are removed by superconductivity.

This fact also has a natural interpretation in terms of pseudoparticles. Figure 41 (left) shows that both important singlet pseudoparticles (for Γ_4 and Γ_2) develop a very sharp peak at the same threshold frequency and, at the same time, their occupancy increases (see Fig. 41, bottom) upon condensation, indicating that electrons are locked into singlets with zero momentum. A gap opens between the singlets and doublets, which gives the gap in the one-particle density of states. Because of this gap in the pseudoparticle thresholds, the large imaginary part of the electron self-energy does not persist in the superconducting state (see also Fig. 17). Notice, however, that in the superconducting state the pseudoparticles are strongly mixed and the off-diagonal spectral function $A_{\Gamma_4\Gamma_2}$ also develops a pole at the same threshold as A_{Γ_4} and A_{Γ_2}. The off-diagonal spectral function $A_{\Gamma_4\Gamma_2}$ describes the creation of a Cooper pair on the cluster $G_{\Gamma_4\Gamma_2} = \langle 0|a_{\Gamma_4}^\dagger(\tau)a_{\Gamma_2}|0\rangle$ and, therefore, diverges at low temperature at the same threshold frequency.

Since the density of states is composed of two almost equally important contributions, i.e., the convolution of the doublet with both singlets (Γ_4 and Γ_2), the superconducting gap is almost particle-hole symmetric in the optimally doped regime with half-width of the order of $0.1t$. When the doping value is changed from its critical value, the asymmetry in the superconducting density of states appears. The magnitude of the asymmetry is the same as the asymmetry of the corresponding normal state spectra and comes from the fact that the occupancy and, therefore, the importance of the Γ_4 singlet exceed the importance of the Γ_2 singlet (see Fig. 41, bottom).

Finally, we comment on the role of the triplet pseudoparticle. The spin susceptibility comes almost entirely from the convolution of the half-filled singlet with the half-filled triplet (Γ_4 with $\Gamma_{4'}$). The latter develops a peak at an energy $0.16t$ upon condensation, which results in the resonance in the spin susceptibility shown in Fig. 39.

It is interesting to derive the form of a low energy Hamiltonian involving the pseudoparticles in question. The conser-

vation of charge, spin, and cluster momentum considerably restricts the form of this Hamiltonian. If we assume that it is of the Kondo form, it takes the following form:

$$
\begin{aligned}
H = &\sum_\Gamma \epsilon_\Gamma a_\Gamma^\dagger a_\Gamma + \sum_{k\mathbf{Q}\sigma} \epsilon_{k\mathbf{Q}} c_{k\mathbf{Q}\sigma}^\dagger c_{k\mathbf{Q}\sigma} \\
&+ J_1 a_{\Gamma_4}^\dagger a_{\Gamma_2} \sum_{kk'\mathbf{Q}\sigma'\sigma} \epsilon_{\sigma,\sigma'} c_{k\mathbf{Q}\sigma} c_{k\mathbf{Q}\sigma'} + \text{H.c.} \\
&+ J_2 \sum_{k\sigma k'\sigma',\mathbf{K},\mathbf{K}'\in[(0,\pi),(\pi,0)]} a_{\Gamma_{3\sigma\mathbf{K}}}^\dagger a_{\Gamma_{3\sigma'\mathbf{K}'}} c_{k'\mathbf{K}'\sigma'}^\dagger c_{k\mathbf{K}\sigma} + \text{H.c.} \\
&+ \lambda \sum_\Gamma (a_\Gamma^\dagger a_\Gamma - 1),
\end{aligned}
\tag{61}
$$

where Γ runs over the relevant low energy pseudoparticles. $\epsilon_{\sigma,\sigma'}$ is an antisymmetric tensor and the $\mathbf{Q}$ runs over cluster momenta. Here, $c_{k\mathbf{Q}\sigma}^\dagger$ operators create electrons in the bath with cluster momenta $\mathbf{Q}$ and spin σ. The operators $a_\Gamma^\dagger$ create a pseudoparticle on the cluster [see Eq. (15)].

This Hamiltonian contains the competition of the particle-hole and particle-particle channels for pairing with the baths of conduction electrons, and the approach to criticality is controlled by the variation of the on-site energy ϵ_Γ, which should be identified with the pseudoparticle thresholds. It would be very interesting to investigate this impurity model with the tools and the perspective of Ref. 133. It is clear that superconductivity will add magnetic field like terms proportional to $\langle a_{\Gamma_4}^\dagger a_{\Gamma_2}\rangle \sum_{kk'\mathbf{Q}\sigma'\sigma}\epsilon_{\sigma,\sigma'}c_{k\mathbf{Q}\sigma}c_{k\mathbf{Q}\sigma'}$. These terms should be strongly relevant and move the system away from criticality.

Within CDMFT, the cluster of few sites (2×2 in our case) hybridizes with the Weiss field Δ, defined in Eq. (6). In single site DMFT, this effective medium drives the Mott transition. On the Bethe lattice within single site DMFT, it is proportional to the local Green's function $\Delta = t^2 G$ and, therefore, becomes gapped in the Mott-insulating state, while it remains gapless in the metallic phase. Hence, due to the DMFT self-consistency condition, this quantity shows a very strong doping dependence.

Within cluster DMFT, the effective medium is only weakly doping dependent, and the evolution with doping is smooth (see Fig. 42) in the doping range considered here. Moreover, this quantity shows very mild momentum dependence as opposed to strong momentum dependence of self-energy shown in Fig. 5. For example, the (0,0) and (π,π) Green's functions show almost no spectra at low frequency (are almost gapped), while the hybridization functions of these two orbitals are very similar to $(0,\pi)$ hybridization function, which contains most of the low frequency spectral weight. The mild and smooth doping dependences of hybridization functions lead us to believe that the proximity to quantum cluster criticality, which manifests itself in large scattering rate and vanishing coherence scale, is driven by the impurity model itself rather than the self-consistency condition.

The picture here is based entirely on a finite temperature analysis and is in the spirit of the DMFT approach, where we approach the strong correlation problem starting from high temperatures.
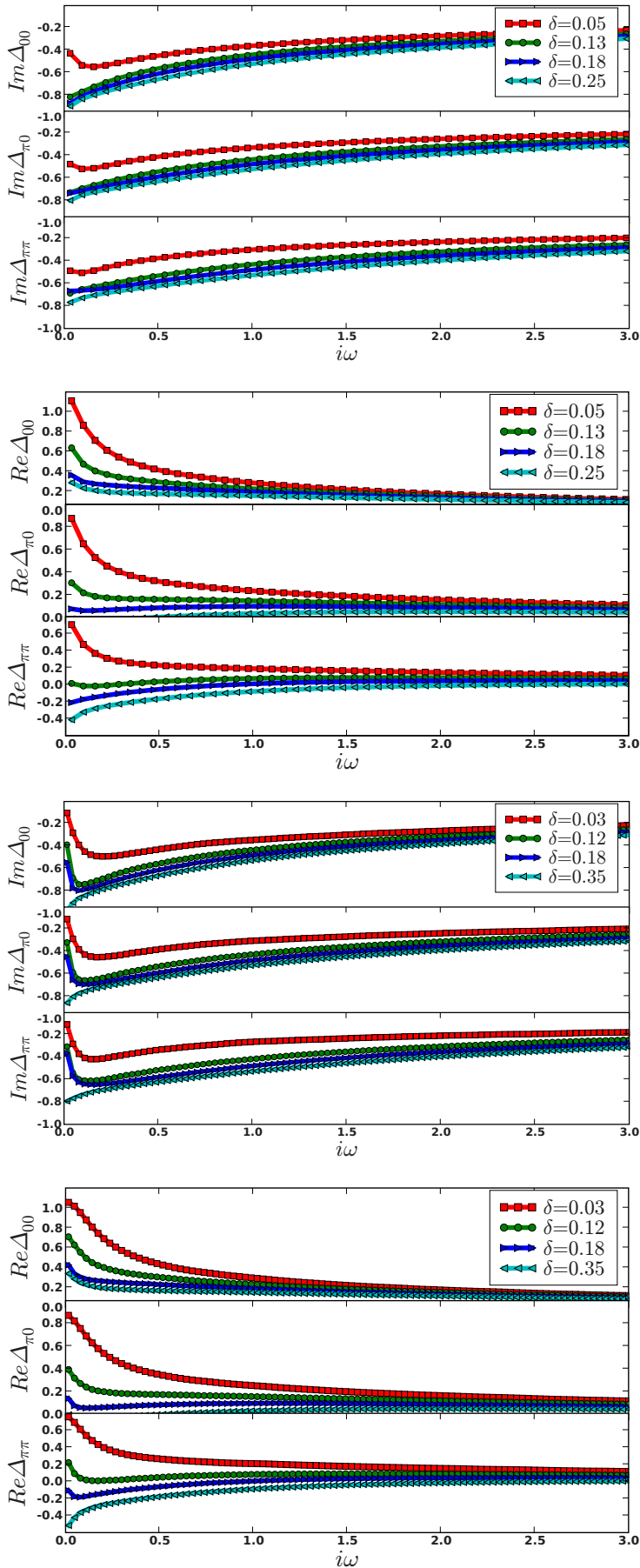
FIG. 42. (Color online) First panel: Imaginary parts of the cluster hybridization functions for various dopings in the normal state at $T=0.01t$ using C-DMFT and CTQMC. Second panel: Real parts of the same hybridization functions in the normal state at $T=0.01t$. Third panel: Imaginary parts of the same hybridization functions in the superconducting state at $T=0.005t$. Fourth panel: Real part of the same hybridization functions in the superconducting state at $T=0.005t$. The self-energies of the cluster show strong momentum dependence, while hybridizations are only weakly momentum dependent. Furthermore, there seems to be no indication of any criticality in the hybridization functions such as the formation of a gap.

It is important to continue the normal solutions of the plaquette DMFT equations to very low temperature to clarify the mathematical source of the criticality that we observe at higher temperatures. The critical point could occur exactly at $T=0$, as proposed by Capone *et al.*[62] in the context of the two band Hubbard model with inverted Hund rule exchange and by us in Ref. [50]. The quantum critical point may exist in an impurity model with a fixed bath or might require the DMFT self-consistency condition. Alternatively, there may be a finite second order endpoint of a first order line, as found in DMFT lattice models related to the two impurity model.[134] Notice also that power laws in an intermediate asymptotic regime, without an obvious underlying quantum critical impurity model, have also been found in an impurity model related to frustrated magnets.[68]

Still, the precise nature of the low temperature normal state phase below T_C is not essential for the validity of the CDMFT description. What matters is that at very high temperature, $T>J$, single site DMFT is a good description of the system, and as we lower the temperature, we find a broad region of temperatures where the plaquette reference frame correctly captures the physics of the problem with its apparent criticality, even though at much lower temperatures a more nonlocal description will be needed. It is even possible that the zero temperature solution of the DMFT equations does not exist, in which case, unlike the standard BCS theory where the superconductivity is viewed as an instability of a normal phase, we would have a superconducting state that exists without an underlying normal state.

There is an important distinction between our views and those of local quantum critical scenario based on single site EDMFT scenario.[135] In the latter case, the locality of the quantum critical theory of the lattice is asserted to be reliable at $T=0$, while the results of the EDMFT equations in two dimensions are known to be less reliable as temperature is raised.[136] On the other hand, the results of plaquette DMFT are expected to become more accurate as the temperature is raised.

VIII. CONCLUSION AND DISCUSSION

In this paper, we developed and applied a plaquette dynamical mean-field theory to understand the nature of the superconductivity near the Mott transition. In relation to earlier works, we focused on low but finite temperatures to allow a comparison with the underlying normal phase. For this purpose, advanced impurity solvers were brought to bear on the solution of the CDMFT equations.

The idea of using a plaquette in a self-consistent medium as a reference frame to reconstruct physical correlation functions on a lattice, while appealing, has several different implementations through different cluster schemes. Here, we stressed the numerous qualitative features which are common to all methods while pointing out the few significant quantitative discrepancies that we found among the different cluster methods in the course of our investigations.

The low temperature landscape of strongly correlated electron systems can have many competing phases, for example, commensurate and incommensurate condensates of charge spin and current. A first step toward understanding this landscape is to follow the evolution of well defined phases as a function of control parameters. In this paper, we focused on the superconducting and normal phases. Other phases and the competition with superconductivity can be studied with CDMFT techniques, as was done, for example, in Ref. [37] for the commensurate antiferromagnetism.

We find that the normal state in the mean-field theory has two distinct regimes, which are naturally characterized in terms of the regimes of the impurity model. At low doping, in the immediate proximity of the Mott-insulating state, we have a realization of the RVB picture of holes propagating in a sea of spins with strong singlet correlations. In the impurity model language, that corresponds to the RKKY phase of the two impurity model and its generalization to a plaquette. At high doping, we have a regime with well formed quasiparticles, with a Fermi surface containing $1-\delta$ electrons. In the impurity model language, this corresponds to the Kondo regime of the one impurity model, and single site DMFT provides an adequate description of its properties.

Plaquette CDMFT has three independent cluster self-energies. For very large doping, only the local cluster self-energy is nonzero, indicating the validity of single site DMFT. As doping is reduced, $\Sigma_{\pi\pi}(i\omega)$ acquires large real and imaginary parts. This is controlled by the existence of a pole which approaches zero frequency at certain doping δ_1^c ($\delta_1^c \sim 0.1$ in the *t-J* model and $\delta_1^c=0$ in the Hubbard model). When combined with the cumulant periodization, this anomalous growth gives rise to a topological transition associated with the formation of line of zeros in the Green's function (line of poles in the self-energy) at zero temperature discussed in Ref. [43]. We call the doping at which the topological transition of the Fermi surface happens as δ_3^c. Notice, however, that from a CDMFT perspective which focuses on the finite temperature description, an infinite self-energy is not necessary, and all that is required to generate the pseudogap regime with its concomitant formation of Fermi arcs is a self-energy which exceeds the bandwidth.

We identified another critical doping δ_2^c associated with a maximum in the scattering rate of the third cluster degree of freedom $\Sigma_{0\pi}$. This is an example of cluster quantum multicriticality. Namely, a mapping of a lattice model onto a quantum impurity model with a critical point. This critical point satisfies the following conditions: (a) it requires a cluster of impurities for its existence, hence it has no analogy in single site DMFT, and (b) has at least two unstable (relevant) directions (for example, the ratio J_{Kondo}/J_{RKKY} and particle-hole symmetry breaking in the two impurity model Jones-Varma critical point[131]).

At a critical doping δ_2^c, there is an avoided critical point in the normal phase, which is near the doping level with the highest superconducting transition temperature. Since $\delta_2^c > \delta_1^c$, δ_2^c may lie very close to δ_3^c if one adopts a periodization scheme along the lines of the cumulant periodization, but this issue is left for future studies since it strongly depends on the periodization scheme. Looking at the scattering rate and coherence temperature in the normal state solution of CDMFT equations, we thus identified a critical doping δ_2^c which could be related to the hidden quantum critical point, which has been hypothesized by many authors based on a large body of experimental data.[131,137]

We have not analyzed the properties of the CDMFT quantum impurity model describing the normal state at zero temperature. It is even possible that the normal state solution simply does not exist at $T=0$. These points are largely academic from the point of view of the finite temperature physics which we want to describe with CDMFT. The manifestations of the possible quantum criticality are rapidly removed by the onset of superconductivity. The electronic lifetime on the Fermi surface controlled by Im $\Sigma(0,\pi)$ is dramatically reduced as the system becomes superconducting.

One then arrives at a superconducting state, which inherits the normal state gap, largely caused by $\Sigma_{\pi\pi}$, but with coherent nodal quasiparticles characterized by a weakly doping dependent velocity perpendicular to the Fermi surface. The velocity along the Fermi surface v_Δ has a domelike shape and decreases in the underdoped regime, providing further support to the two gap picture of the superconducting state of the underdoped cuprates.[51,52,99–101]

The superconducting phase is stabilized by the gain of superexchange energy, namely, improved spin-spin singlet correlations. We resolved the frequency dependence of the anomalous Green's function and the anomalous self-energy, and found them to have a structure very different from conventional phonon mediated superconductivity in the Migdal-Eliashberg theory. Since the superconducting state restores coherence, long lived sharp excitations, Bogoliubov quasiparticles, and a sharp spin mode which resembles the neutron "40 meV resonance" emerge below T_C.

We extracted different observables such as tunneling density of states, optical conductivity, optical mass and plasma frequencies, integrated optical spectral weight superfluid stiffness, and spin susceptibility which compare well at a qualitative level with experimental data on copper oxide materials.

We have shown that at δ_2^c (which occurs very near the maximum in T_C), the coherence energy vanishes and the scattering rate is maximal. At this doping, an approximate particle-hole symmetry in the one electron spectra is recovered, and approximate power laws in physical quantities ($\sigma \propto \omega^{-2/3}$) emerge in an intermediate frequency range.

Upon periodization, the large value of the nonlocal self-energies turn Fermi surface into Fermi arcs,[43] and we studied the evolution of the Fermi arcs with temperature. We showed that within C-DMFT, Fermi arcs shrink with decreasing temperature.

Our solution of the CDMFT on a plaquette has many similarities with the earlier studies of Anderson's resonating valence bond theory of high temperature superconductivity in the slave boson mean-field theory formulation. This approach correctly predicted the d-wave symmetry of the superconducting order parameter and the presence of a pseudogap with the same symmetry well above T_C.[18]

The similarity between the results of the CDMFT and slave boson approaches is not accidental. Both methods are mean-field techniques based on order parameters that can be defined within a plaquette, and capture the effects of the proximity to a Mott-insulating state using a small set of short-range degrees of freedom.

Compared with slave boson mean-field theory, CDMFT has additional flexibility both in the frequency of the one electron spectral function as well as in its momentum dependence. One crucial difference is a much more pronounced momentum space differentiation with very different electronic properties at the nodes and at the antinodes. This anisotropy, with the concomitant existence of two energy scales in the superconductor, resolves the earlier problems of the RVB theory related to the doping dependence of the linear term of the penetration depth.[138] The need for the introduction of more anisotropy in the microscopic theory had been anticipated by experiments and by the phenomenological analysis of Ioffe and Millis.[139–141] Recent phenomenological models[83,84] have also generated a more pronounced momentum dependence of the one-particle spectra and incorporated in their approach a v_Δ that decreases with decreasing doping. The main differences between these phenomenological approaches and the more microscopic C-DMFT reside in the location of the lines of zeros of the Green function. While in Refs. [83] and [84] the lines of zero lie on the umklapp surface, in C-DMFT the lines of zeros are dynamical entities with a location that evolves with doping.

CDMFT is an extension of single site DMFT, an approach that has been very successful in describing many aspects of the finite temperature Mott transition. By using a single impurity in a medium, this method has been able to describe several regimes near a Mott transition: a Fermi-liquid regime at small U and temperature, a bad metal at temperature larger than a characteristic temperature $T_{coh}(U)$, a Mott insulator at large U and low temperature, and a bad insulator when the temperature is high enough that the Hubbard bands begin to merge.

By construction, single site DMFT assigns the same self-energy to the electronic states on the whole Fermi surface. Hence, at a given energy and temperature, either all the states at all **k** points are coherent or they are all incoherent. This is not a good description of the high temperature superconductors, which therefore cannot be described with single site DMFT.

On the other hand, CDMFT allows the states in the nodal region to be coherent quasiparticles, while, at the same time, the states in the antinodal region are highly incoherent and have a pseudogap, i.e., $T_{coh}(nodal) \ll T_{coh}(antinodal)$. The self-energy in the nodal region could be compared to a single site DMFT in the Fermi-liquid regime with $U < U_{c2}$ and $T_c < T_{coh}(U)$, while the antinodal self-energy is more of a single site DMFT in the bad insulator regime, $U > U_{c2}$ and $T_c > T_{coh}(U)$. Plaquette DMFT offers a mean-field picture of the lattice problem, whereby the different cluster self-energies and cumulants describe different regions of momentum space with distinct physical properties: a nodal region which is closest to a Fermi liquid, an antinodal region which exhibits a pseudogap, and an intermediate region between the two, described by the $(0,\pi)$ self-energy, which exhibits the maximum scattering rate at criticality.

This qualitative picture is only a crude caricature of the full CDMFT solution, but it is a useful qualitative guide to understand how the Fermi arcs originate from the proximity to the Mott insulator, and above all, highlights why single site DMFT is inadequate in this situation.

The objective of this work was to advance our understanding of the t-J and Hubbard models as a "bare bones"

model of the density driven Mott transition. An important open problem is to incorporate and understand how other effects, such as the effects of more realistic band structure in the multiband model, the disorder, and the electron-phonon interaction, which play an important role in cuprates, can affect the solution of the model,

We presented a qualitative comparison with several experiments in the copper oxide based materials and gave the limitations of the model and of the methodology used; this comparison is very encouraging and warrants future studies including more accurate modeling and further methodological improvements.

Future studies should include a realistic band structure of the copper-oxygen planes and additional Coulomb terms beyond the local Hubbard U that can be accommodated on the plaquette. In addition to $d_{x^2-y^2}$ copper band, it would be desirable to include another copper band, namely, d_{z^2} band which is coupled to apical oxygen. Although the latter band is filled in the band structure calculation, it comes close to the Fermi level.

Another important direction is to better momentum resolve one particle and two particle quantities. The latter will require advances in the analytic continuation techniques of QMC data as well as a better understanding of how to convert cluster quantities into lattice observables in C-DMFT. Furthermore, within a cluster size, it is important to implement an optimal choice of orbitals in CDMFT, describing different momentum patches in the Brillouin zone. Functional approaches[23,142] as well as CDMFT inspired modeling

of experimental data along the lines of Ref. 143 can provide useful guidance in this direction.

Mean-field approaches clearly separates the short distance effects contained in the theory from long distance effects, which will require the introduction of fluctuations due to vortices and pair fluctuations. The T_C vs δ line in CDMFT should be interpreted as being close to the Nerst line in the cuprate phase diagram.[144] On the other hand, the true superconducting critical temperature line is strongly reduced relative to the CDMFT on the underdoped side of the phase diagram to the effects of long wavelength fluctuations of the order parameter, which require long wavelength field theoretical techniques along the lines of Ref. 145

Finally, other inhomogeneous phases, such as stripes, charge, bond, pair density waves, and other broken symmetries, can appear as secondary instabilities and can be studied with our methods by inserting relatively local (restricted to a plaquette) but site dependent self-energies into the CDMFT functional.

[1] See the articles in Nat. Phys. **2**, 138 (2006).

[2] P. A. Lee, N. Nagaosa, and X. G. Wen, Rev. Mod. Phys. **78**, 17 (2006).

[3] M. R. Norman and C. Pepin, Rep. Prog. Phys. **66**, 1547 (2003).

[4] E. Fischer, M. Kugler, I. Maggio-Aprile, C. Berthod, and C. Renner, Rev. Mod. Phys. **79**, 353 (2007).

[5] T. P. Devereaux and R. Hackl, Rev. Mod. Phys. **79**, 175 (2007).

[6] T. Timusk and B. Statt, Rep. Prog. Phys. **62**, 61 (1999).

[7] S. Sachdev, Rev. Mod. Phys. **75**, 913 (2003).

[8] M. A. Kastner, R. J. Birgeneau, G. Shirane, and Y. Endoh, Rev. Mod. Phys. **70**, 897 (1998).

[9] A. Damascelli, Z. Hussain, and Z. X. Shen, Rev. Mod. Phys. **75**, 473 (2003).

[10] D. N. Basov and T. Timusk, Rev. Mod. Phys. **77**, 721 (2005).

[11] E. Dagotto, Rev. Mod. Phys. **66**, 763 (1994).

[12] D. J. Van Harlingen, Rev. Mod. Phys. **67**, 515 (1995).

[13] W. E. Pickett, Rev. Mod. Phys. **61**, 433 (1989).

[14] J. P. Carbotte, Rev. Mod. Phys. **62**, 1027 (1990).

[15] P. W. Anderson, Science **235**, 1196 (1987).

[16] P. W. Anderson, *The Theory of Superconductivity in the High T_C Cuprates* (Princeton University Press, Princeton, NJ, 1997).

[17] G. Baskaran, Z. Zou, and P. W. Anderson, Solid State Commun. **63**, 973 (1987).

[18] G. Kotliar and J. Liu, Phys. Rev. B **38**, 5142 (1988).

[19] C. Gros, Phys. Rev. B **38**, 931 (1988).

[20] A. Paramekanti, M. Randeria, and N. Trivedi, Phys. Rev. Lett. **87**, 217002 (2001).

[21] A. Georges, G. Kotliar, W. Krauth, and M. J. Rozenberg, Rev. Mod. Phys. **68**, 13 (1996).

[22] G. Kotliar and D. Vollhardt, Phys. Today **57**, 53 (2004).

[23] G. Kotliar, S. Y. Savrasov, K. Haule, V. S. Oudovenko, O. Parcollet, and C. A. Marianetti, Rev. Mod. Phys. **78**, 865 (2006).

[24] K. Held, I. A. Nekrasov, G. Keller, V. Eyert, N. Blümer, A. K. McMahan, R. T. Scalettar, T. Pruschke, V. I. Anisimov, and D. Vollhardt, 2003, Psi-k Newsletter **56**, 65 (http://psik.dl.ac.u.k).

[25] K. Held, I. A. Nekrasov, N. Blumer, V. I. Anisimov, and D. Vollhardt, Int. J. Mod. Phys. B **15**, 2611 (2001).

[26] K. Held, A. K. McMahan, and R. T. Scalettar, Phys. Rev. Lett. **87**, 276404 (2001).

[27] S. Y. Savrasov, G. Kotliar, and E. Abrahams, Nature (London) **410**, 793 (2001).

[28] X. Dai, S. Y. Savrasov, G. Kotliar, A. Migliori, H. Ledbetter, and E. Abrahams, Science **300**, 953 (2003).

[29] S. Y. Savrasov, K. Haule, and G. Kotliar, Phys. Rev. Lett. **96**, 036404 (2006).

[30] K. Haule, V. Oudovenko, S. Y. Savrasov, and G. Kotliar, Phys. Rev. Lett. **94**, 036401 (2005).

[31] J. H. Shim, K. Haule, and G. Kotliar, Nature (London) **446**, 513 (2007).

[32] T. Maier, M. Jarrell, T. Pruschke, and M. H. Hettler, Rev. Mod. Phys. **77**, 1027 (2005).

[33] T. D. Stanescu and G. Kotliar, Phys. Rev. B **70**, 205112 (2004).

[34] T. A. Maier, M. Jarrell, T. C. Schulthess, P. R. C. Kent, and J. B. White, Phys. Rev. Lett. **95**, 237001 (2005).

[35] A. I. Lichtenstein and M. I. Katsnelson, Phys. Rev. B **62**, R9283 (2000).

[36] Th. Maier, M. Jarrell, Th. Pruschke, and J. Keller, Phys. Rev. Lett. **85**, 1524 (2000).

[37] M. Capone and G. Kotliar, Phys. Rev. B **74**, 054513 (2006).

[38] D. Sénéchal, P. L. Lavertu, M. A. Marois, and A. M. S. Tremblay, Phys. Rev. Lett. **94**, 156404 (2005).

[39] A. M. S. Tremblay, B. Kyung, and D. Sénéchal, Low Temp. Phys. **32**, 424 (2006).

[40] M. Jarrell, Th. Maier, M. H. Hettler, and A. N. Tahvildarzadeh, Europhys. Lett. **56**, 563 (2001).

[41] A. Macridin, M. Jarrell, T. Maier, P. R. C. Kent, and E. D'Azevedo, Phys. Rev. Lett. **97**, 036401 (2006).

[42] T. D. Stanescu and P. Phillips, Phys. Rev. Lett. **91**, 017002 (2003).

[43] T. D. Stanescu and G. Kotliar, Phys. Rev. B **74**, 125110 (2006).

[44] T. D. Stanescu, M. Civelli, K. Haule, and Gabriel Kotliar, Ann. Phys. (N.Y.) **321**, 1682 (2006).

[45] B. Kyung, S. S. Kancharla, D. Sénéchal, A.-M. S. Tremblay, M. Civelli, and G. Kotliar, Phys. Rev. B **73**, 165114 (2006).

[46] D. Sénéchal and A. M. S. Tremblay, Phys. Rev. Lett. **92**, 126401 (2004).

[47] O. Parcollet, G. Biroli, and G. Kotliar, Phys. Rev. Lett. **92**, 226402 (2004).

[48] M. Civelli, M. Capone, S. S. Kancharla, O. Parcollet, and G. Kotliar, Phys. Rev. Lett. **95**, 106402 (2005).

[49] K. Haule and G. Kotliar, Europhys. Lett. **77**, 27007 (2007).

[50] K. Haule and G. Kotliar, arXiv:cond-mat/0605149 (unpublished).

[51] M. Civelli, M. Capone, A. Georges, K. Haule, O. Parcollet, T. D. Stanescu, and G. Kotliar, arXiv:0704.1486 (unpublished).

[52] M. Aichhorn, E. Arrigoni, Z. B. Huang, and W. Hanke, arXiv:cond-mat/0702391 (unpublished).

[53] S. S. Kancharla, M. Civelli, M. Capone, B. Kyung, D. Senechal, G. Kotliar, and A.-M. S. Tremblay, arXiv:cond-mat/0508205 (unpublished).

[54] Bumsoo Kyung, Jean-Sebastien Landry, and A.-M. S. Tremblay, Phys. Rev. B **68**, 174502 (2003).

[55] T. A. Maier, A. Macridin, M. Jarrell, and D. J. Scalapino, arXiv:0706.0241 (unpublished).

[56] P. Werner, A. Comanac, L. de Medici, M. Troyer, and A. J. Millis, Phys. Rev. Lett. **97**, 076405 (2006).

[57] K. Haule, Phys. Rev. B **75**, 155113 (2007).

[58] N. E. Bickers, Rev. Mod. Phys. **59**, 845 (1987).

[59] K. Haule, A. Rosch, J. Kroha, and P. Wölfle, Phys. Rev. Lett. **89**, 236402 (2002).

[60] K. Haule, A. Rosch, J. Kroha, and P. Wölfle, Phys. Rev. B **68**, 155119 (2003).

[61] K. Haule, S. Kirchner, J. Kroha, and P. Wölfle, Phys. Rev. B **64**, 155111 (2001).

[62] M. Capone, M. Fabrizio, C. Castellani, and E. Tosatti, Phys. Rev. Lett. **93**, 047001 (2004).

[63] M. Capone, M. Fabrizio, C. Castellani, and E. Tosatti, Science **296**, 2364 (2002).

[64] Q. Si and J. L. Smith, Phys. Rev. Lett. **77**, 3391 (1996); J. L. Smith and Q. Si, Phys. Rev. B **61**, 5184 (2000).

[65] R. Chitra and G. Kotliar, Phys. Rev. Lett. **84**, 3678 (2000).

[66] A. M. Sengupta and A. Georges, Phys. Rev. B **52**, 10295 (1995).

[67] O. Parcollet and A. Georges, Phys. Rev. B **59**, 5341 (1999).

[68] A. Georges, R. Siddharthan, and S. Florens, Phys. Rev. Lett. **87**, 277203 (2001).

[69] G. Kotliar, S. Y. Savrasov, G. Palsson, and G. Biroli, Phys. Rev. Lett. **87**, 186401 (2001).

[70] M. H. Hettler, A. N. Tahvildar-Zadeh, M. Jarrell, T. Pruschke, and H. R. Krishnamurthy, Phys. Rev. B **58**, R7475 (1998).

[71] Th. A. Maier, Physica B **359–361**, 512 (2005); arXiv:cond-mat/0312447 (unpublished).

[72] A. Koga, N. Kawakami, T. M. Rice, and M. Sigrist, Phys. Rev. Lett. **92**, 216402 (2004).

[73] L. de' Medici, A. Georges, and S. Biermann, Phys. Rev. B **72**, 205124 (2005).

[74] S. Biermann, L. de' Medici, and A. Georges, Phys. Rev. Lett. **95**, 206401 (2005).

[75] R. Ofer, G. Bazalitsky, A. Kanigel, A. Keren, A. Auerbach, J. S. Lord, and A. Amato, Phys. Rev. B **74**, 220508(R) (2006).

[76] G. Biroli and G. Kotliar, Phys. Rev. B **71**, 037102 (2005).

[77] A. A. Abrikosov, Physics (Long Island City, N.Y.) **2**, 21 (1965).

[78] J. Kroha and P. Wölfle, Acta Phys. Pol. B **29**, 3781 (1998).

[79] I. Dzyaloshinskii, Phys. Rev. B **68**, 085113 (2003).

[80] C. Berthod, T. Giamarchi, S. Biermann, and A. Georges, Phys. Rev. Lett. **97**, 136401 (2006).

[81] R. M. Konik, T. M. Rice, and A. M. Tsvelik, Phys. Rev. Lett. **96**, 086407 (2006).

[82] F. H. L. Essler and A. M. Tsvelik, Phys. Rev. B **71**, 195116 (2005).

[83] B. Valenzuela and E. Bascones, arXiv:cond-mat/0611154 [Phys. Rev. Lett. (to be published)].

[84] K.-Y. Yang, T. M. Rice, and F.-C. Zhang, Phys. Rev. B **73**, 174501 (2006).

[85] T. D. Stanescu, P. Phillips, and Ting-Pong Choy, Phys. Rev. B **75**, 104503 (2007).

[86] M. Grilli and G. Kotliar, Phys. Rev. Lett. **64**, 1170 (1990).

[87] G. Kotliar, *Strongly Interacting Fermions and High Tc Superconductivity*, edited by B. Doucot and J Sinn-Justin, Proceedings of the Les Houches Summer School of Theoretical Physics, Session LVI, 1991 (Elsevier Sience, New York, 1995), pp. 201–247.

[88] G. Kotliar and J. Liu, Phys. Rev. B **38**, 5142 (1988).

[89] N. M. Plakida and V. S. Oudovenko, Phys. Rev. B **59**, 11949 (1999).

[90] D. Poilblanc, D. J. Scalapino, and S. Capponi, Phys. Rev. Lett. **91**, 137203 (2003).

[91] M. Civelli and G. Kotliar (unpublished).

[92] A. Kanigel, M. R. Norman, M. Randeria, U. Chatterjee, S. Souma, A. Kaminski, H. M. Fretwell, S. Rosenkranz, M. Shi, T. Sato, T. Takahashi, Z. Z. Li, H. Raffy, K. Kadowaki, D. Hinks, L. Ozyuzer, and J. C. Campuzano, Nat. Phys. **2**, 447 (2006).

[93] N. Doiron-Leyraud, C. Proust, D. LeBoeuf, J. Levallois, J. B. Bonnemaison, R. Liang, D. A. Bonn, W. N. Hardy, and L. Taillefer, Nature (London) **447**, 565 (2007).

[94] Z. Wang, Y. Bang, and G. Kotliar, Phys. Rev. Lett. **67**, 2733 (1991).

[95] N. Nagaosa and P. A. Lee, Phys. Rev. Lett. **64**, 2450 (1990).

[96] M. Randeria, R. Sensarma, N. Trivedi, and F. C. Zhang, Phys. Rev. Lett. **95**, 137001 (2005).

[97] H. Eskes, M. B. J. Meinders, and G. A. Sawatzky, Phys. Rev. Lett. **67**, 1035 (1991).

[98] M. B. J. Meinders, H. Eskes, and G. A. Sawatzky, Phys. Rev. B **48**, 3916 (1993).

[99] G. Deutscher, Nature (London) **397**, 410 (1999).

[100] M. Le Tacon, A. Sacuto, A. Georges, G. Kotliar, Y. Gallais, D. Colson, and A. Forget, Nat. Phys. **2**, 537 (2006).

[101] K. Tanaka, W. S. Lee, D. H. Lu, A. Fujimori, T. Fujii, Risdiana, I. Terasaki, D. J. Scalapino, T. P. Devereaux, Z. Hussain, and Z.-X. Shen, Science **314**, 1910 (2006).

[102] B. Kyung and A. M.-S. Tremblay, arXiv:cond-mat/0204500 (unpublished).

[103] K. K. Gomes, A. N. Pasupathy, A. Pushp, S. Ohno, Y. Ando, and A. Yazdani (private communication).

[104] X. J. Zhou, T. Yoshida, A. Lanzara, P. V. Bogdanov, S. A. Kellar, K. M. Shen, W. L. Yang, F. Ronning, T. Sasagawa, T. Kakeshita, T. Noda, H. Eisaki, S. Uchida, C. T. Lin, F. Zhou, J. W. Xiong, W. X. Ti, Z. X. Zhao, A. Fujimori, Z. Hussain, and Z.-X. Shen, Nature (London) **423**, 398 (2003).

[105] A. F. Santander-Syro, R. P. S. M. Lobo, N. Bontemps, W. Lopera, D. Girata, Z. Konstantinovic, Z. Z. Li, and H. Raffy, Phys. Rev. B **70**, 134504 (2004); A. F. Santander-Syro, R. P. S. M. Lobo, and N. Bontemps, arXiv:cond-mat/0404290 (unpublished).

[106] R. A. Ferrell and R. E. Glover, Phys. Rev. **109**, 1398 (1958); M. Tinkham and R. A. Ferrell, Phys. Rev. Lett. **2**, 331 (1959).

[107] G. Deutscher, A. F. Santander-Syro, and N. Bontemps, Phys. Rev. B **72**, 092504 (2005).

[108] H. J. A. Molegraaf, C. Presura, D. van der Marel, P. H. Kes, and M. Li, Science **295**, 2239 (2002).

[109] J. Hwang, T. Timusk, and G. D. Gu, arXiv:cond-mat/0607653 (unpublished).

[110] A. V. Boris, N. N. Kovaleva, O. V. Dolgov, T. Holden, C. T. Lin, B. Keimer, and C. Bernhard, Science **304**, 708 (2004); A. F. Santander-Syro and N. Bontemps, arXiv:cond-mat/0503767 (unpublished).

[111] A. B. Kuzmenko, H. J. A. Molegraaf, F. Carbone, and D. van der Marel, Phys. Rev. B **72**, 144503 (2005).

[112] F. Carbone, A. B. Kuzmenko, H. J. A. Molegraaf, E. van Heumen, V. Lukovac, F. Marsiglio, D. van der Marel, K. Haule, G. Kotliar, H. Berger, S. Courjault, P. H. Kes, and M. Li, Phys. Rev. B **74**, 064510 (2006).

[113] Y. S. Lee, K. Segawa, Z. Q. Li, W. J. Padilla, M. Dumm, S. V. Dordevic, C. C. Homes, Y. Ando, and D. N. Basov, Phys. Rev. B **72**, 054529 (2005).

[114] W. J. Padilla, Y. S. Lee, M. Dumm, G. Blumberg, S. Ono, K. Segawa, S. Komiya, Y. Ando, and D. N. Basov, Phys. Rev. B **72**, 060511(R) (2005).

[115] A. El Azrak, R. Nahoum, N. Bontemps, M. Guilloux-Viry, C. Thivet, A. Perrin, S. Labdi, Z. Z. Li, and H. Raffy, Phys. Rev. B **49**, 9846 (1994).

[116] D. van der Marel, H. J. A. Molegraaf, J. Zaanen, Z. Nussinov, F. Carbone, A. Damascelli, H. Eisaki, M. Greven, P. H. Kes, and M. Li, Nature (London) **425**, 271 (2003).

[117] M. M. Zemljic and P. Prelovsek, Phys. Rev. B **72**, 075108 (2005).

[118] A. Toschi, M. Capone, M. Ortolani, P. Calvani, S. Lupi, and C. Castellani, Phys. Rev. Lett. **95**, 097002 (2005).

[119] H. J. A. Molegraaf, C. Presura, D. van der Marel, P. H. Kes, and M. Li, Science **295**, 2239 (2002).

[120] M. Ortolani, P. Calvani, and S. Lupi, Phys. Rev. Lett. **94**, 067002 (2005).

[121] A. F. Santander-Syro, R. P. S. M. Lobo, N. Bontemps, W. Lopera, D. Girata, Z. Konstantinovic, Z. Z. Li, and H. Raffy, Phys. Rev. B **70**, 134504 (2004).

[122] C. Panagopoulos, B. D. Rainford, J. R. Cooper, W. Lo, J. L. Tallon, J. W. Loram, J. Betouras, Y. S. Wang, and C. W. Chu, Phys. Rev. B **60**, 14617 (1999).

[123] D. M. Broun, P. J. Turner, W. A. Huttema, S. Ozcan, B. Morgan, Ruixing Liang, W. N. Hardy, and D. A. Bonn, arXiv:cond-mat/0509223 (unpublished).

[124] B. R. Boyce, J. A. Skinta, and T. R. Lemberger, Physica C **341-348**, 561 (2000).

[125] Y. Sidis, S. Pailhes, B. Keimer, P. Bourges, C. Ulrich, and L. P. Regnault, Phys. Status Solidi B **241**, 1204 (2004).

[126] S. A. Kivelson, I. P. Bindloss, E. Fradkin, V. Oganesyan, J. M. Tranquada, A. Kapitulnik, and C. Howald, Rev. Mod. Phys. **75**, 1201 (2003).

[127] T. Nakano, M. Oda, C. Manabe, N. Momono, Y. Miura, and M. Ido, Phys. Rev. B **49**, 16000 (1994).

[128] Y. Kubo, Y. Shimakawa, T. Manako, and H. Igarashi, Phys. Rev. B **43**, 7875 (1991).

[129] P. Dai, H. A. Mook, S. M. Hayden, G. Aeppli, T. G. Perring, R. D. Hunt, and F. Doan, Science **284**, 1344 (1999).

[130] D. J. Scalapino and S. R. White, Phys. Rev. B **58**, 8222 (1998).

[131] B. A. Jones and C. M. Varma, Phys. Rev. Lett. **58**, 843 (1987).

[132] B. A. Jones, B. G. Kotliar, and A. J. Millis, Phys. Rev. B **39**, 3415 (1989).

[133] M. Ferrero, L. De Leo, P. Lecheminant, and M. Fabrizio, arXiv:cond-mat/0702629 (unpublished).

[134] G. Moeller, V. Dobrosavljevic, and A. E. Ruckenstein, Phys. Rev. B **59**, 6846 (1999).

[135] Q. Si et al., Nature (London) **413**, 804 (2001).

[136] S. Pankov, G. Kotliar, and Y. Motome, Phys. Rev. B **66**, 045117 (2002).

[137] J. L. Tallon et al., Phys. Status Solidi B **215**, 531 (1999).

[138] X. G. Wen and P. A. Lee, Phys. Rev. Lett. **80**, 2193 (1998).

[139] L. B. Ioffe and A. J. Millis, Phys. Rev. B **58**, 11631 (1998).

[140] L. B. Ioffe and A. J. Millis, Science **285**, 1241 (1999).

[141] L. B. Ioffe and A. J. Millis, Phys. Rev. B **61**, 9077 (2000).

[142] G. Biroli, O. Parcollet, and G. Kotliar, Phys. Rev. B **69**, 205108 (2004).

[143] A. Perali, M. Sindel, and G. Kotliar, Eur. Phys. J. B **24**, 487 (2001).

[144] Z. Xu, N. P. Ong, Y. Wang, T. Kakeshita, and S. Uchida, Nature (London) **406**, 486 (2000).

[145] Zlatko Tesanovic, arXiv:0705.3836 (unpublished).